TUNABLE FERROELECTRIC THIN FILM DEVICES FOR MICROWAVE APPLICATIONS

SHENG SU

NATIONAL UNIVERSITY OF SINGAPORE

2011

TUNABLE FERROELECTRIC THIN FILM DEVICES FOR MICROWAVE APPLICATIONS

SHENG SU
(M. Sc., Wuhan University)

A THESIS SUBMITTED
FOR THE DEGREE OF DOCTOR OF PHILOSOPHY
DEPARTMENT OF PHYSICS
NATIONAL UNIVERSITY OF SINGAPORE

2011

Acknowledgments

Many people have been helping and supporting me in different ways throughout this work. I would like to express my deepest gratitude to my supervisor, Professor Ong Chong Kim. Working with you has made my Ph.D. study a memorable experience. In addition to the knowledge and skills you taught me, your serious attitude for scientific research and work ethic has given me a great example of how to work as a scientist. I am grateful that you gave me a lot of freedom to pursue what I was interested in. Also, I would like to thank Professor Sow Chorng Haur and Professor Ariando for serving on my thesis committee.

Special thanks must be given to Mr. Cheng Wei Ning and Dr. Wang Peng for their initial introduction in the field of microwave measurement, Mr. Chen Xin and Dr. Zhang Xiao Yu for their assistance and contribution in this project.

Many thanks go to my past and present colleagues of the Center of Superconducting and Magnetic Materials (CSMM), Dr. Ma Yun Gui, Dr. Xu Feng, Dr. Zhao Li, Ms. Phua Li Xian, Dr. Nguyen Nguyen Phuoc, Mr. Le Thanh Hung, Ms. Song Qing, Ms. Lim Siew Leng. Their friendship made my graduate study in Singapore more meaningful and enjoyable.

Thanks go to all the other people not mentioned here, but to whom I am grateful for their kind assistance in one way or another.

Last but not least, I want to express my gratitude and love to my parents, my wife Wang Fen and my lovely son Sheng Hao Yu, for their encouragement and patience with me and their unending support and love. To them this thesis is dedicated.

Table of Contents

Page

Acknowledgments ..... **i**

Table of Contents ..... **ii**

Summary ..... **v**

List of Publications ..... **vii**

List of Tables ..... **viii**

List of Figures ..... **ix**

Chapter

1. Introduction **1**

1.1 Motivations for ferroelectric tunable microwave devices 1

1.2 An overview of tunable microwave devices 3

1.2.1 Brief review of non-ferroelectric technologies 4

1.2.2 Ferroelectric technology 6

1.3 Ferroelectric materials and their microwave applications 7

1.3.1 Theory of dielectric response of ferroelectric materials 9

1.3.2 Tunable ferroelectric thin film microwave devices 13

1.4 Objectives of this study 15

References 17

2. Fabrication and Microwave Characterization of Ferroelectric Thin Films **21**

2.1 Fabrication of ferroelectric thin films 21

2.1.1 Pulsed laser deposition process 23

2.1.2 Target preparation and thin film deposition parameter optimization 25

2.2 Microwave measurement techniques for ferroelectric thin films 26

2.2.1 Lumped capacitance measurement method 27

2.2.2 Coplanar waveguide transmission line method 31

2.2.3 Coplanar resonator method 34

2.3 Experimental measurement 36

2.3.1 Preparation of top electrode layer 36

2.3.2 Measurement setup 39

References 39

3. Ferroelectric Thin Film Varactors 42
3.1 Introduction 42
3.2 Parallel plate varactors 44
3.2.1 Characterization of microwave dielectric properties of BST parallel plate varactors 44
3.2.2 Effects of bottom electrodes on microwave dielectric properties of BST parallel plate varactors 54
3.3 Comparison of microwave properties of BST varactors with parallel plate and interdigital electrodes 59
3.4 Hybrid varactors 67
3.4.1 Design with coplanar and parallel plate structures 67
3.4.2 Experiments and results 69
3.4.3 Conclusion 72
References 72

4. Coplanar Waveguide Ferroelectric Thin Film Microwave Phase Shifters 76
4.1 Introduction 76
4.1.1 Microwave phase shifters 76
4.1.2 Coplanar waveguide transmission lines 78
4.2 Theory of distributed transmission line phase shifters 80
4.3 Design and implementation of coplanar waveguide ferroelectric microwave phase shifters 82
4.4 Experimental results and discussion 87
4.5 Conclusion 88
References 89

5. Coupled Microstrip Line Ferroelectric Thin Film Microwave Phase Shifters 92
5.1 Properties of coupled microstrip line 92
5.2 Design and simulation of coupled microstrip line phase shifter circuit 94
5.3 Fabrication process and measurement results 100
5.4 Conclusion 103
References 104

6. Composite Right/Left-Handed Transmission Line Microwave Phase Shifter Using Ferroelectric Varactors 105
6.1 Introduction 105

6.2 Model of composite right/left-handed transmission line phase shifters 107
6.2.1 Left-handed transmission lines 107
6.2.2 Composite right/left-handed transmission lines 108
6.2.3 Phase shift of varactor-tuned CRLH TLs 109
6.3 Realization of CRLH TL line phase shifter using ferroelectric varactors 111
6.3.1 Design and fabrication 111
6.3.2 Measurement results and discussion 113
6.4 Conclusions 117
References 118

7. Dual-Tunable Trilayered Structure of Ferroelectrics and Multiferroics for Microwave Device Applications 120
7.1 Introduction 120
7.2 Experimental procedure and samples 122
7.3 Results and discussion 123
7.4 Conclusion 128
References 129

8. Conclusions and Future Work 131
8.1 Conclusions 131
8.2 Future work 134

Summary

Recent researches have been focused on the development of microwave tunable devices based on ferroelectric thin films. Barium strontium titanate ($Ba_xSr_{1-x}TiO_3$ or BST) thin films are currently considered to be the most suitable candidate for tunable microwave applications. In this thesis, the main work includes improvement of dielectric properties of BST thin films, microwave characterization of ferroelectric thin films, design and fabrication of tunable microwave devices based on BST thin films.

There are little reliable data on the microwave dielectric properties of parallel plate ferroelectric varactors, due to the difficulty of completely removing the parasitic inductance and resistance generated by the electrodes. By the consistency of the electromagnetic simulation results and measured results with simple analytical model, we developed an accurate evaluation technique for microwave dielectric properties which is indispensable for optimizing ferroelectric materials. The parasitic effects can be effectively corrected by introducing correction resistances and equivalent circuits.

We have studied the microwave dielectric properties of BST thin films deposited by pulsed laser deposition (PLD). Firstly, effects of bottom electrodes including $La_{0.7}Sr_{0.3}MnO_3$ (LSMO), Pt and Au, on microwave dielectric properties of BST parallel plate varactors were investigated. Secondly, a systematic comparison of the microwave properties of BST thin film varactors with parallel plate and interdigital electrodes was carried out. Finally, a multiferroic trilayered structure composed of a $BiFeO_3$ (BFO) layer and two $Ba_{0.25}Sr_{0.75}TiO_3$ (BST) layers grown on platinized silicon substrate

was studied. The significant tuning response for the dielectric constant with the electric field and the magnetic field respectively was obtained for the trilayered structure.

In our study on ferroelectric varactors, a new hybrid varactor structure proposed by our group was modified and fabricated. In this structure, an ultra-thin film with low conductivity is used as dc bias electrode and at the same time the electrode does not contribute in the electric field distribution of microwave signal. The fabricated BST hybrid varactor with a modified structure showed a low capacitance and improved tunability compared with the conventional coplanar varactor.

In the development of phase shifter device, we proposed three kinds of phase shifters integrated on high resistance Si-substrates using ferroelectric thin film varactors. Firstly, a distributed coplanar waveguide (CPW) transmission line phase shifter using parallel-plate BST thin film varactors was presented. This phase shifter structure provided a simple method and high microwave phase shift properties. Then, an analog microwave phase shifter, which consists of coupled microstrip line loaded with parallel plate BST varactors and two planar Marchand baluns, was demonstrated. The phase shifter devices based on coupled microstrip line structure are less sensitive to interfacial effects and require simple processing. Lastly, a composite right/left-handed transmission line (CRLH TL) phase shifter with parallel plate BST thin film varactors was presented. The CRLH TL phase shifter using BST varactors provided a differential phase shift with flat frequency dependence characteristic in the operating frequency range.

List of Publications

1. S. Sheng, and C. K. Ong, Multifunctional dual-tunable multiferroic $Ba_{0.25}Sr_{0.75}TiO_3$-$BiFeO_3$-$Ba_{0.25}Sr_{0.75}TiO_3$ trilayered structure for tunable microwave applications, *J. Phys. D: Appl. Phys.* **44**, 165406 (2011).

2. S. Sheng, and C. K. Ong, Distributed transmission line phase shifter using parallel-plate ferroelectric thin film varactors, *Microelectronic Engineering*, **87**, 1932 (2010).

3. S. Sheng, X. Y. Zhang, P. Wang, and C. K. Ong, Effect of bottom electrodes on dielectric properties of high frequency $Ba_{0.5}Sr_{0.5}TiO_3$ parallel plate varactor, *Thin Solid Films*, **518**, 2864 (2010).

4. S. Sheng, P. Wang, X. Chen, X. Y. Zhang, and C. K. Ong, Two paralleled $Ba_{0.25}Sr_{0.75}TiO_3$ ferroelectric varactors series connected coplanar waveguide microwave phase shifter, *J. Appl. Phys.* **105**, 114509 (2009).

5. X. Y. Zhang, Q. Song, F. Xu, S. Sheng, P. Wang and C. K. Ong, Dielectric dispersion of $Ba_xSr_{1-x}TiO_3$ thin film with parallel-plate and coplanar interdigital electrodes, *J. Phys. D: Appl. Phys.* **42**, 065411 (2009).

6. S. Sheng, P. Wang, and C. K. Ong, Compact Tunable periodically LC Loaded phase shifter using left-handed transmission line, *Microwave and Optical Technology Letters.* **51**(9), 2127 (2009).

7. X. Y. Zhang, P. Wang, S. Sheng, Y. G. Ma, F. Xu and C. K. Ong, A novel structure for dc bias on varactors in composite right/left-handed transmission lines phase shifter using $Ba_{0.25}Sr_{0.75}TiO_3$ thin film, *J. Phys. D: Appl. Phys*. **42**, 175103 (2009).

8. S. Sheng, P. Wang, X. Y. Zhang, and C K Ong, Characterization of microwave dielectric properties of ferroelectric parallel plate varactor, *J. Phys. D: Appl. Phys.* **42**, 015501 (2009).

9. X. Y. Zhang, P. Wang, S. Sheng, F. Xu, and C. K. Ong, Ferroelectric $Ba_xSr_{1-x}TiO_3$ thin-film varactors with parallel plate and interdigital electrodes for microwave applications, *J. Appl. Phys.* **104**, 124110 (2008).

10. S. Sheng, P. Wang, and C. K. Ong, A new hybrid ferroelectric varactor with promising microwave properties for tunable microwave applications, *IEEE Electron Device Letters*, Submitted.

11. S. Sheng, and C. K. Ong, Coupled microstrip line microwave phase shifter using ferroelectric thin film varactors, *Progress In Electromagnetics Research-PIER*, Submitted.

List of Tables

		Page
Table 3.1	The parameters and dielectric properties of the parallel plate and interdigital varactors.	60
Table 4.1	The primary parameters used to simulate phase shifter.	83

List of Figures

		Page
Figure 1.1	ABO_3 perovskite lattice structures in paraelectric (a) and ferroelectric states (b). Above T_c, their crystal lattice has a cubic structure in (a) and is paraelectric. Below T_c, the centers of the positive and negative charges shift and the crystal is characterized by spontaneous polarization.	9
Figure 1.2	Polarization dependences on the applied electric field for (a) a ferroelectric state and (b) a paraelectric state. In (a), P_s is the saturation polarization, P_r is the remnant polarization, E_c is the coercive field.	12
Figure 2.1	The schematic basic setup for PLD system for thin film fabrication.	22
Figure 2.2	The shape of the plasma plume in PLD process.	24
Figure 2.3	The plane-view and cross sections of ferroelectric thin films capacitors. (a) Parallel plate capacitor; (b) interdigital capacitor.	28
Figure 2.4	Schematic of a coplanar waveguide (CPW) on ferroelectric thin film.	31
Figure 2.5	A ferroelectric thin film coplanar resonator.	34
Figure 2.6	The photograph of one-port measurement setup (a) and a magnified image of GSG microprobe (b).	38
Figure 3.1	The cross section of the varactor (a) and the photograph of the measurement setup using a GSG coplanar waveguide probe (b).	45
Figure 3.2	X-ray diffraction pattern (a) and cross sectional SEM image (b) of the BST film on Pt/Si substrate.	46
Figure 3.3	Measured S_{11} reflection data curve of varactor, plotted in polar representation (a) and phase of the S_{11} as a function of frequency for measured data and HFSS simulation results, inset shows the distribution of electric field in varactor using HFSS (b).	48

Figure 3.4	A simplified equivalent circuit of the parallel plate varactor.	49
Figure 3.5	The simulated and measured real and imaginary parts of the S_{11} parameters of the varactor.	50
Figure 3.6	Frequency dependencies of capacitance (a) and loss tangents (b) of varactor before and after correction. The two test structures: a_1=20 μm, a_2=30 μm, b=60 μm.	51
Figure 3.7	Frequency dependences of capacitance of varactor at V=0 and 12V. Inset shows the voltage dependence of capacitance of varactor at 1GHz.	52
Figure 3.8	X-ray diffraction patterns of the BST films on different bottom electrode.	55
Figure 3.9	Cross section SEM images of BST/LSMO (a) BST/Pt (b) BST/Au (c) varactors.	56
Figure 3.10	Dielectric constant and loss tangent of the BST thin films grown on LSMO, Au, and Pt bottom electrodes as a function of the measured frequency.	57
Figure 3.11	Permittivity of BST film as a function of temperature at f=10 kHz. The inset shows the inverse of permittivity with the temperature.	60
Figure 3.12	Capacitance as a function of frequency for BST film under 0-60 V dc bias. The inset in (a) displays the schematic of interdigital capacitance and the inset in (b) shows the loss tangent with a variation in frequency at different dc voltage.	61
Figure 3.13	S_{11} and phase shift as a function of frequency for HFSS simulation results and sample BST-0.25. The inset shows the distribution of electric field in interdigital varactor using HFSS.	63
Figure 3.14	dc bias field dependent capacitance of BST film in the interdigital structure at the frequency of 1 GHz.	64

Figure 3.15	(a) Capacitance with a variation of frequency in parallel plate structure measurement under 0 and 12 V. (b) Loss tangent as a function of frequency at different dc voltage.	65
Figure 3.16	The conceptual diagram of columnar BST grain, grain boundary and electric field lines in coplanar and parallel-plate varactors.	66
Figure 3.17	Layer structure of the hybrid varactor and orientation of electrical field lines in the varactor.	68
Figure 3.18	XRD patterns of the thin films (a) ZnO, (b) BST/ZnO on (001) LAO substrates.	69
Figure 3.19	Photograph of the hybrid varactor. The marked interdigital electrode was used for one-port measurement and the outer electrode was designed for applying dc bias.	70
Figure 3.20	Tunability of the hybrid varactor at different bias voltages. Inset shows the capacitance and the quality factor of the varactor at zero bias.	71
Figure 4.1	Equivalent circuit of distributed ferroelectric phase shifter.	80
Figure 4.2	(a) Layout of the distributed transmission line phase shifter of coplanar waveguide. (b) The side view of a parallel plate varactor. (c) The photograph of top view of a varactor.	82
Figure 4.3	The matching impedance of phase shifter circuit as a function of capacitance of shunt varactor.	84
Figure 4.4	The simulation results of the phase shifter under different full port impedance.	84
Figure 4.5	Frequency dependent insertion loss and return loss of the distributed ferroelectric phase shifter based on 6 unit cells at different bias voltages.	86
Figure 4.6	Differential phase shift of the phase shifter as a function of frequency at different bias voltages.	86

Figure 5.1	A configuration of conventional coupled microstrip lines.	92
Figure 5.2	Field distributions resulting from (a) even-mode and (b) odd-mode excitation of the coupled microstrip lines.	93
Figure 5.3	A schematic structure of a segment of the coupled microstrip line loaded with three varactors.	96
Figure 5.4	The simulated response of the coupled microstrip line loaded with eight capacitors of capacitance of 0.12 pF.	96
Figure 5.5	The topology of the planar balun using microstrip line to coupled microstrip lines.	97
Figure 5.6	Layout of top conductor layer of the planar Marchand balun.	98
Figure 5.7	Simulated S-parameters for the planar Marchand balun. Inset shows magnitude of the electric field in the balun.	99
Figure 5.8	Layout of the coupled microstrip line phase shifter, with all dimensions in millimeters.	100
Figure 5.9	Measured frequency dependent insertion loss and return loss of the phase shifter based on 8 unit cells at zero bias voltages.	101
Figure 5.10	Measured differential phase shift of the phase shifter as a function of frequency at different bias voltages.	101
Figure 6.1	Equivalent circuit model for an infinitesimal short LH TL.	107
Figure 6.2	Equivalent circuit model of the CRLH unit cell (a) and Dispersion diagram of a CRLH TL [2].	109
Figure 6.3	(a) Equivalent circuit of the CRLH TL phase shifter. (b) Layout of the phase shifter. (c) and (d) Magnified top-view and cross section of the varactors C_R and C_L, and RF ground.	112

Figure 6.4	Capacitance and loss tangent of two series connected varactors at f=1 GHz as a function of dc bias up to 10 V.	114
Figure 6.5	Comparison between measured and HFSS simulated forward transmission and reflection magnitude.	114
Figure 6.6	Measured magnitude and phase responses of the phase shifter under different bias voltages.	115
Figure 6.7	Differential phase shift under different dc biases over each varactor.	116
Figure 7.1	XRD patterns of the films (a) BST, (b) BFO/BST, and (c) BST/BFO/BST on (111) Pt/TiO_2 $/SiO_2/Si$ substrates.	123
Figure 7.2	SEM picture of cross-section of the trilayered BST/BFO/BST thin films.	124
Figure 7.3	(a) The relative dielectric constant (ε_r) versus external electric fields for the trilayered BST/BFO/BST structure at 0.1 MHz. (b) The *P-E* hysteresis loops for the trilayered BST/BFO/BST structure at a series of external fields at room temperature and 250 Hz, where the inset for the *P-E* loop of the single layer BFO thin film.	125
Figure 7.4	Microwave frequency dependences of the capacitance and loss tangent for the BST/BFO/BST trilayered structure. The insets show the cross-section of the trilayered structure and the photograph of the measurement setup using a GSG coplanar waveguide probe, respectively.	126
Figure 7.5	The capacitance of the multiferroic BST/BFO/BST trilayered structure versus frequency under different external magnetic field. The inset shows the magnetic field dependences of the capacitance at different frequency and loss tangent at 10 kHz.	128

Chapter 1

INTRODUCTION

1.1 Motivations for Ferroelectric Tunable Microwave Devices

Modern radio frequency (RF) and microwave engineering is an exciting and dynamic field, due in large part to the explosive growth of commercial wireless markets and the symbiosis between recent advances in modern electronic device technology. The widespread use of RF and microwave integrated circuit (IC) technology along with device miniaturization trend have led to the development of RF and microwave circuit components whose dimensions are much smaller than their wavelength. The miniaturization, reliability, ease of assembly and compactness of IC fabrication technology are the factors that paved the way for embedding these components directly into the substrates. In recent years, there is a rapidly growing demand for electrically tunable RF and microwave devices in advanced radar and mobile communication systems. The high dielectric nonlinearity (i.e. the strong dependence of dielectric constant on electric field) of ferroelectric materials with perovskite structure has made them promising candidates for these applications.

The application of ferroelectric materials in tunable microwave devices was first introduced in the 1960's [1-4]. However, real applications of ferroelectric materials were limited by device electronics and material technology at that time. Currently there is a huge research interest in utilizing

ferroelectric thin films for tunable microwave devices since they have high tunability, low loss, fast switching speeds and good power handling capability at GHz frequencies. There are several reviews on different aspects of tunable ferroelectric devices, including both material science and device designs [5-11]. Ferroelectric materials are widely used in microwave tunable components such as variable capacitors (i.e. varactors), tunable resonators, frequency-agile filters, phase shifters, variable power dividers and tunable oscillators. There are also ferroelectric devices based nonlinear components such as harmonic generator, parametric amplifier, pulse shaper and mixer. In all the ferroelectric tunable devices, ferroelectric materials always show up in the form of varactors directly or equivalently, so ferroelectric based varactors are crucial components in RF and microwave devices.

The $Ba_xSr_{1-x}TiO_3$ ($0 < x < 1$) (BST) thin films are currently considered to be important materials for tunable microwave devices because BST thin films have high dielectric constants, high tunability, low dielectric loss tangent and low leakage current; most importantly, it can be integrated on a traditional Si substrate to replace the current silicon oxide and nitride dielectrics, which would have considerable commercial impact. Both theoretical and experimental works have shown that the dielectric constant of $Ba_xSr_{1-x}TiO_3$ is highly dependent on the temperature, the Ba/Sr ratio and internal or external stresses. By changing one or more factors, the dielectric properties can be tuned broadly, especially in the layered or graded composites. It is well known that in the vicinity of the paraelectric-to-ferroelectric phase transition temperature, the thermodynamic properties of BST show large anomalies accompanied with large increases in dielectric constant and tunability.

The subsequent sections will provide an overview of tunable microwave devices. Also, the basic theory of dielectric response of ferroelectric materials and tunable ferroelectric thin film microwave device applications will be presented.

1.2 An Overview of Tunable Microwave Devices

The components and circuits in a RF and microwave system can be divided into two groups: passive and active. Microwave tunable passive devices mainly include filters, phase shifters, delay lines and network matching circuits in connection with such applications as antenna arrays, communications and radar transceivers. In the early days of microwaves, tuning was done manually or mechanically. Today, many circuit options are available to realize such tunable devices whose performances are closely related to the choice of a technology. These options essentially include mechanical tuning, semiconductors, RF micro-electro-mechanical systems (MEMS), ferrites and ferroelectric materials. Electric and magnetic fields (voltage, current), optical interactions or mechanical manipulations are used to achieve tunability in components based on them. The ranges and the speed of tunability, control power consumption, losses of microwave signal, power handling capability, potentials of integration, cost, and other parameters of the devices depend on the materials used, the controlling mechanisms (magnetic, optical, electrical, mechanical), and the design. The next two sections will briefly review those technologies and put emphasis on ferroelectric material

technology, which has performances comparable or better than competing commercial technologies.

1.2.1 Brief Review of Non-Ferroelectric Technologies

The earliest forms of tunable circuits were all mechanical, for example, the rotary vane adjustable waveguide phase shifter firstly proposed by Fox in 1947 [12]. Early mechanically tunable devices make use of coaxial lines or hollow metal waveguides and trimming screws/motors/stepper motors. Mechanical circuits are inexpensive, easy to fabricate and have very low loss and possess good power handling capability. However their disadvantages include their large size, low tuning speed, low cost effectiveness, and sensitive to vibrations.

Semiconductor technology is a very popular alternative for making tunable integrated microwave devices. Classically, the tuning can be made with switching or continuous mode using PIN or varactor diodes, respectively [13-14]. The tunable devices based on semiconductor are very small (in μms), very fast (<1 μs for pin diode and <1 ns for field effect transistor (FET)), and have large tunability. In addition, they can be easily integrated with other circuits for example in monolithic microwave integrated circuits (MMICs). However, their linear decrease of quality factor (Q factor) over frequency confines their usability to be only in the lower end of microwave range. Efforts to compensate the high ohmic loss of varactor diodes by using FETs as negative resistors have resulted in almost lossless filters at the expense of higher power consumption and lower bandwidth [15]. Despite these problems,

semiconductors are widely used in tuning applications as they offer low cost and compact advantages and allow faster tuning speeds. However, for large arrays, such as phased arrays with up to 10 000 and more radiating elements, the power consumption and heat sink are the main problems hindering applications of semiconductor devices.

In early 1990s, MEMS were started to use for tunable circuits, where tunability is obtained by the physical movement of a component which changes the capacitance of the device [16]. Excluding MEMS antennas, there are to date two generic types of MEMS circuits: switch and varactor [17]. MEMS varactors are very competitive [18- 19]. They have advantage of very high Q factor, higher self resonance, higher power handling capability, and low control power solutions. Moreover, electro-statically actuated MEMS have a near zero power consumption and a more linear capacitance variation with applied voltage. However, due to the mechanical structures, their response is slower than ferroelectric and GaAs varactors. MEMS also require very high operating voltage by far and they are sensitive to environmental conditions such as moisture, temperature and vibrations.

Ferrite has been used to fabricate microwave tunable devices [20-21], mostly include phase shifters and filters. These devices take advantage of a property of ferromagnetic materials to change its permeability with an applied DC magnetic field therefore allowing control of the phase constant of the waveguiding medium. Similar to MEMS varactors, ferrite devices can be tuned continuously or switched between the two states. The latter technique makes use of the magnetic hysteresis of the ferrite core to store a remanent permeability. The switching speed between the two remanent states is in the

order of few microseconds. Because of the difficulty in magnetic field generation, the ferrite tunable devices are always bulky, slow and power consuming.

1.2.2 Ferroelectric Technology

Ferroelectric based varactors have demonstrated strong potential for commercial applications in the microwave frequency range for its tuning speed, low cost and ease of power handling. In comparison with non-ferroelectric technologies, ferroelectric varactors and tunable devices based on them have potential of easy integration with standard Si and GaAs processes [22-26]. As opposed to ferrite, the permittivity of ferroelectric materials can be changed proportionally to the intensity of an applied DC electric field. Permittivity also varies with temperature so it must be compensated within an acceptable range. An operating temperature slightly above the Curie-point in the paraelectric phase is normally preferred for tunable devices as it is characterized by a less dispersive permittivity at microwave frequencies and low hysteresis effect. Moreover, the permittivity and breakdown voltage of ferroelectric thin films are intrinsically high thus allowing for increased miniaturization and high power handling. Overall, though ferroelectric materials may prevail or yield in different aspects of the contest, they have been proven to be a very competitive candidature for the development of microwave tunable devices.

The main disadvantage in using ferroelectric materials for tunable wireless devices is the relatively high dielectric loss tangent of ferroelectric materials

which leads to microwave dissipation. However recent researches, including work carried out in our lab [27-28], indicated that the loss tangent can be reduced by improved thin film fabrication method and material enhancement such as by doping [29-35] or multilayering the ferroelectric thin film [36-38]. Furthermore with proper device design, it is usually possible to reduce insertion loss through reduction in device tunability such that a compromise can be made for satisfactory performance. Although there are a lot of reports on the integration of ferroelectric materials with tunable microwave devices, further improvement and understanding of ferroelectric materials is required before more competitive devices can be developed. Also, research is required to develop prototypes of ferroelectric based varactors and miniature microwave communication applications such as phase shifters and tunable matching networks, etc.

1.3 Ferroelectric Materials and Their Microwave Applications

A ferroelectric material is normally in single crystalline, thin film or polycrystalline form, and possesses a reversible spontaneous polarization over a certain temperature range. There is a critical temperature (usually referred as the Curie or transition temperature), which marks the transition from an ordered to a disordered state. The phase transition induces a mechanical strain, tending to change not only the volume and the shape of the material body, but also the refractive index of the material. Thus ferroelectric materials exhibit piezoelectric, pyroelectric, and electro-optic properties in addition to the

ferroelectric property, which can be used for many technological applications [39].

In modern physics of dielectrics, we deal with the study of ferroelectric, anti-ferroelectric, piezoelectric and pyroelectric materials. All ferroelectrics are piezoelectric and pyroelectric, but they additionally possess a reversible, non-volatile macroscopic spontaneous electric dipole moment in the absence of an external electric field. In simple words, ferroelectric crystals can be seen as assembly of batteries with a particular orientation, which remains stable unless an external electric field is applied to change its direction. Their polar state is a consequence of the structural transition from a high-temperature (high-symmetry) paraelectric phase to a low-temperature (low-symmetry) ferroelectric phase. For the use in tunable microwave devices, the paraelectric phase is often preferred since it has no hysteresis associated with the domain walls.

Two main types of ferroelectrics are distinguished: order-disorder and displacive. In order-disorder type ferroelectrics, the ferroelectricity, i.e. the spontaneous polarization is associated with the ordering of the ions below phase transition temperature. Crystals with the hydrogen bounding, like KH_2PO_4, belongs to this type of ferroelectrics. In displacive ferroelectrics one sublattice of the crystal is displaced relative to the other resulting in spontaneous polarization below phase transition temperature. Complex metal oxides with perovskite structure belong to this group (i.e. $BaTiO_3$, $KNbO_3$). Most ferroelectric materials have perovskite structure, named after the $CaTiO_3$ perovskite mineral; in fact ferroelectricity itself is closely related to the intrinsic structure frustration associated with perovskite structures. A perfect

perovskite structure has a general formula of ABO_3, where A represents a divalent or a trivalent cation, and B is typically a tetravalent or a trivalent cation. As shown in Figure 1.1, A atoms occupy the corner of the cube, while the B atoms sit in the center inside the octahedral formed be oxygen atoms, which are at the face centers. Above the Curie temperature (T_c), their crystal lattice has a cubic structure (Figure 1.1 (a)). In this phase the crystal has no spontaneous polarization. Its permittivity is rather high, DC field, temperature and strain dependent. Below T_c the centers of the positive and negative charges shift (Figure 1.1 (b)), and the crystal is characterized by spontaneous polarization.

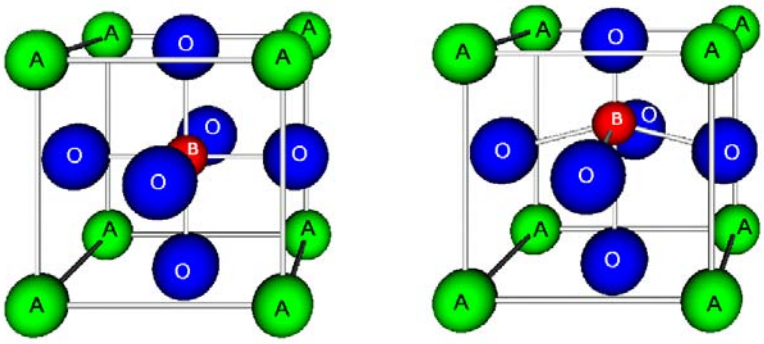

(a) (b)

Figure 1.1 ABO_3 perovskite lattice structures in paraelectric (a) and ferroelectric states (b). Above T_c, their crystal lattice has a cubic structure in (a) and is paraelectric. Below T_c, the centers of the positive and negative charges shift and the crystal is characterized by spontaneous polarization.

1.3.1 Theory of Dielectric Response of Ferroelectric Materials

The most straightforward description of the dielectric response of ferroelectrics is given by thermodynamic theory of Landau [40]. The thermodynamic theory correlates different macroscopic values such as

temperature, polarization and energy. The theory is based on the expansion of the Helmholtz free energy F of a ferroelectric crystal as a function of the vector macroscopic polarization P [41]. We assume that the free energy F in one dimension may be expanded as:

$$F(P,T) = \frac{1}{2}\alpha P^2 + \frac{1}{4}\beta P^4 + \cdots \quad (1.1)$$

where the coefficients α, β depend, in general, on temperature. At this instance the higher order terms in this expansion are ignored. The series does not contain terms in odd powers of P because the free energy of the crystal will not change with polarization reversal. The phenomenological formulation should be applied for the whole temperature range over which the material is in the paraelectric and ferroelectric states.

The equation of state $\partial F/\partial P = E$ then leads to a relation between the polarization and electric field:

$$E = \alpha P + \beta P^3 \quad (1.2)$$

From equation (1.2) it becomes clear that the coefficient α should have a meaning of the inverse permittivity:

$$\alpha = 1/(\varepsilon\varepsilon_0)\,, \quad (1.3)$$

where ε is the relative dielectric permittivity and ε_0 is the dielectric constant of vacuum. According to the Landau theory, the coefficient α is assumed to be linear function of temperature and vanishes at the Curie-Weiss temperature T_0. To obtain the ferroelectric state, the coefficient of P^2 term must be negative for the polarized state to be stable, while in the paraelectric state it must be positive passing through zero at some temperature T_0:

$$\alpha = (T - T_0)/\varepsilon_0 C\,, \quad (1.4)$$

where C is taken as a positive constant called the Curie-Weiss constant and the value of T_0 may be equal to or lower than the actual transition temperature T_c (Curie temperature). The validity of this assumption is experimentally supported by the Curie-Weiss law.

If β is positive, the polarization for zero electric field can be found from eq. (1.2):

$$\alpha P_s + \beta P_s^3 = 0, \tag{1.5}$$

so that either $P_s = 0$ or $P_s^2 = (\varepsilon_0 C/\beta)(T_0 - T)$. For $T \geq T_0$, the only real root of eq. (1.5) is at $P_s = 0$ since C and β are positive. Therefore, T_0 is equal to the Curie temperature T_c. For $T < T_0$, the minimum of the free energy in zero electric field is at

$$P_s = \sqrt{(T_0 - T)/(\beta \varepsilon_0 \varepsilon C)} \tag{1.6}$$

Below the Curie temperature T_0 the ferroelectric is in ferroelectric state with the spontaneous polarization $P_s = \sqrt{(T_0 - T)/(\beta \varepsilon_0 \varepsilon C)}$. Above T_0 the ferroelectric is in paraelectric state with $P_s = 0$. The transition is the first order if β is negative. For the first order phase transition, the Curie-Weiss temperature is a little bit smaller than the Curie temperature, $T_0 < T_c$.

From eq. (1.2) and eq. (1.3), the dielectric permittivity is obtained:

$$\varepsilon = \frac{1}{\varepsilon_0}\frac{\partial E}{\partial P} = \frac{1}{\varepsilon_0(\alpha + 3\beta P^2)} \tag{1.7}$$

In paraelectric state ($T > T_c$) with zero bias electric field ($P = 0$), one can get Curie-Weiss law:

$$\varepsilon = \frac{C}{T - T_c} \tag{1.8}$$

In ferroelectric state ($T < T_c$) with zero bias electric field ($P = P_s$), the dielectric permittivity is written as:

$$\varepsilon = \frac{C}{2(T_C - T)} \tag{1.9}$$

In ferroelectric state, the electric field response of ferroelectric materials shows a typical hysteresis loop as shown in Figure 1.2 (a); similar behavior is also found in ferromagnetic materials under magnetic fields. The remnant polarization P_r, is the polarization value of the material at zero bias, also known as the spontaneous polarization, the saturation polarization P_s, is the maximum polarization, and the coercive field E_c, is the field necessary to reverse the direction of the net polarization of the material. In paraelectric state, the spontaneous polarization is zero and the polarization dependence on the external electric field is again nonlinear but without hysteresis loop, as shown in Figure 1.2 (b).

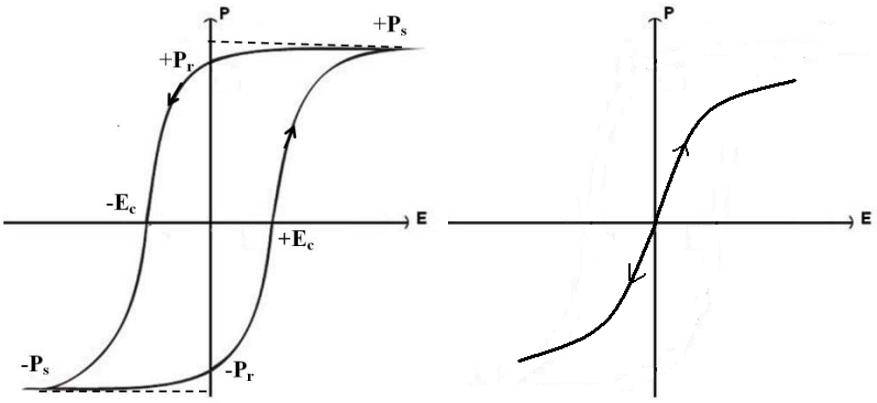

(a) (b)

Figure 1.2 Polarization dependences on the applied electric field for (a) a ferroelectric state and (b) a paraelectric state. In (a), P_s is the saturation polarization, P_r is the remnant polarization, E_c is the coercive field.

The main attraction of ferroelectric materials is the strong nonlinear change of their dielectric permittivity ε on the application of an external electric field. This characteristic is commonly described by the tunability *n*

defined as the ratio of the dielectric permittivity of the material at zero electric field to its permittivity at some non-zero electric field, expressed as:

$$n = \varepsilon(0)/\varepsilon(E) \tag{1.10}$$

Another way of expressing the tunability is the relative tunability:

$$n_r = (\varepsilon(0) - \varepsilon(E))/\varepsilon(0) \tag{1.11}$$

The dielectric loss is a critical parameter to consider when optimizing the properties of the ferroelectric material, which should be taken into account in the device design. Low loss is almost always desired for electronic applications, especially for high frequency devices, where dielectric losses would lead to signal loss, which decreases the signal to noise ratio. Dielectric losses arise in ferroelectric crystals due to three predominant sources: (1) an intrinsic loss attributed to multi-phonon scattering, (2) a loss associated with the conversion of the microwave field into acoustic oscillations by regions with residual ferroelectric polarization, and (3) extrinsic losses due to motion of charged defects such as interstitials and vacancies resulting in acoustic waves at the frequency of the applied field [5]. The trend "the higher the dielectric constant, the higher the tunability, loss, and temperature dependence of the dielectric permittivity" is observed for many dielectrics [42]. The optimal balance of these parameters is one challenging problem for best device performance.

1.3.2 Tunable Ferroelectric Thin Film Microwave Devices

Ferroelectrics, especially complex oxides with perovskite structure, are truly multifunctional materials. The sensitivity of the physical properties

(permittivity, polarization, refractive index, magnetic permeability etc.) of these materials to temperature, external electrical, magnetic, and mechanical fields (stresses), especially near the temperatures of phase transitions, make them attractive for applications in electronic and optical devices [43]. Previous designs for tunable microwave devices in bulk ferroelectric materials have resulted in low capacitances and very high applied voltages. Thin-film ferroelectrics provide an advantage over the bulk materials for practical device applications, such as ferroelectric thin films provide us with possibility of device miniaturization and integration. Additional advantage of thin films for tunable devices is the relative low applied electric field, since the voltage can be applied in thickness direction which is usually not larger than 1 μm and small gap electrodes can be readily fabricated with the modern lithography techniques. As a result, Ferroelectric thin films, such as barium strontium titanate (BST), have been extensively studied for microwave device applications. This study will mainly focus on the applications of BST thin films on tunable microwave devices.

Examples of the applications in the field of microwave engineering include varactors, tunable microwave resonators, phase shifters, tunable filters, voltage controlled oscillators, tunable diplexers, and tunable matching networks etc. Many new communications systems would greatly benefit from these components. For example, microwave phase shifters, one of the first and simplest components to be made with ferroelectrics, are used in antenna arrays in order to produce a beam scanning function. It is possible to integrate ferroelectric materials to produce complex electronically steerable antenna arrays with applications in planned low Earth orbiting satellite networks.

1.4 Objectives of This Study

Ferroelectric thin film varactors have performances comparable or better than competing commercial technologies, such as semiconductor, MEMS. Nowadays, there are an extensive number of reports on the integration of ferroelectric thin films for microwave applications. Also, the new "old" technology, ferroelectric microwave devices, is making its way from-the-labs-to-the-fabs [44-45]. However, there are still many challenges to be solved. For example, the major disadvantage of using ferroelectric thin films for tunable microwave devices is its relatively high dielectric loss tangent which leads to microwave dissipation. The microwave dielectric properties of ferroelectric thin films in the varactor form have not been accurately evaluated at microwave frequencies, and the electrical means of improving the total quality factor (Q factor) have not been implemented. Furthermore, the developments of various microwave systems, such as mobile wireless system and radar, have been the driving force behind substantial research efforts toward the designs of miniature and tunable microwave circuits using ferroelectric thin film.

A high performance ferroelectric varactor would have exploitation potential. Tunable microwave devices (such as phase shifters, filters, matching networks, etc.) based on ferroelectric varactors are the most representative components considered for applications in microwave systems. Miniaturization of these devices is to reduce space and weight requirement and is desirable in applications where portability or high device density is required.

Therefore, the main aim of this research was to develop prototypes of ferroelectric based varactors and miniature microwave communication applications such as phase shifters and tunable matching networks, including those based on the group of newly emerging artificial materials termed as metamaterials. The specific objectives of this work are:

(a) To reduce the relatively high dielectric loss tangent of ferroelectric thin films through materials development; to develop accurate characteristic techniques for microwave properties of ferroelectric thin films.

(b) To overcome the initial technological obstacle of fabricating parallel-plate varactors and its applications in tunable devices; to integrate the parallel-plate varactors into tunable microwave devices such as tunable matching network, tunable filter and phase shifter etc.

(c) To understand and implement a new concept regarding metamaterials used in phase shifters through transmission lines loaded with varactors and inductors; to demonstrate its advantages over the novel phase shifter and explore its potential in possible commercialization.

References:

1. M. Di Domenico, D. A. Johnson, and R. H. Pantell, “Ferroelectric garmonic generator and the large-signal microwave characteristics of ferroelectric ceramic”, *J. Appl. Phys.*, **33**(5), 1697-1706 (1962).

2. K. M. Johnson, “Variation of dielectric constant with voltage in ferro-electric ceramics”, *J. Appl. Phys.*, **33**(9), 2826-2831 (1962).

3. Yu. M. Poplavko, “Ferroelectric with controlled dielectric permittivity in a waveguide”, *Radio Eng. (Moscow, in Russian)*, **18**(10), 22-27 (1963).

4. S. N. Das, “Quality of a ferroelectric material”, *IEEE Trans. MTT*, **12**(7), 440-445 (1964).

5. M. J. Lancaster, J. Powell, and A. Porch, “Thin-film ferroelectric micro-wave devices”, *Supercond. Sci. Technol.*, **11**, 1323-1334 (1998).

6. O. G. Vendik, E. K. Hollmann, A. B. Kozyrev, and A. M. Prudan, “Ferroelectric Tuning of Planar and Bulk Microwave Devices”, *Supercond. Sci. Technol.*, **12**(2), 325-338 (1999).

7. David S. Korn and Huey-Daw Wu, “A comprehensive review of microwave system requirements on thin-film ferroelectrics”, *Integrated Ferroelectrics*, **24**, 215-237 (1999).

8. X. X. Xi, Hong-Cheng Li, Wei dong Si, A. A. Sirenko, I. A. Akimov, J.R. Fox, A.M. Clark and Jianhua Hao, “Oxide Thin Films for Tunable Microwave Devices”, *J. Electroceram.*, **4**(2/3), 393-405 (2000).

9. Felix A. Miranda, Fred W. Van Keuls, Robert R. Romanofsky, Carl H. Mueller, Samuel Alterovitz, and Guru Subramanyam, “Ferroelectric Thin Films-Based Technology for Frequency- and Phase-Agile Microwave Communication Applications”, *Integrated Ferroelectrics*, **42**, 131-149 (2002).

10. A. K. Tagantsev, V. O. Sherman, K. F. Astafiev, J. Venkatesh, and N. Setter, “Ferroelectric Materials for Microwave Tunable Applications”, *J. Electroceram.*, **11**, 5-66 (2003).

11. N. Setter, D. Damjanovic, L. Eng, G. Fox, S. Gevorgian, S. Hong, A. Kingon, H. Kohlstedt, N. Y. Park, G. B. Stephenson, I. Stolitchnov, A. K. Taganstev, D. V. Taylor, T. Yamada, and S. Streiffer, “Ferroelectric thin films: Review of materials, properties, and applications”, *J. Appl. Phys.*, **100**, 051606-051646 (2006).

12. A. G. Fox, “An adjustable waveguide phase changer”, *Proc. IRE*, **35**, 1489-1498 (1947).

13. J. F. White, “High power p-I-n diode controlled, microwave transmission phase shifters”, *IEEE Trans. Microwave Theory Tech.*, **13**, 233-242 (1965).

14. K. M. Johnson, “Microwave varactor tuned transistor oscillator design”, *IEEE Trans. Microwave Theory Tech.*, **14**, 564-572 (1966).

15. S. R. Chandler, I.C. Hunter, and J.G. Gardiner, “Active Varactor Tunable Bandpass Filter”, *IEEE Guided wave letters*, **13**(3), 70-71 (1993).

16. L. Lin, C. Nguyen, R.T. Howe, and A.P. Pisano, “Micro electromechanical filters for signal processing”, *Proceedings of IEEE Micro Electro Mechanical Systems, MEMS '92*, pp. 226-231 (1992).

17. G. Rebeiz, “RF MEMS Theory, Design, and Technology”, Wiley, 2003.

18. Huey D. Wu, Kevin F. Harsh, Ronda S. Irwin, Wenge Zhang, Alan R. Mickelson, and Y. C. Lee, “MEMS Designed for Tunable Capacitors”, *Microwave Symposium Digest, IEEE MTT-S International*, **1**, 127-129 (1998).

19. N. S. Barker and G. M. Rebeiz, “Optimization of distributed MEMS transmission-line phase shifters-U-band and W-band designs”, *IEEE Trans. Microwave Theory Tech.*, **48**, 1957-1966 (2000).

20. F. Reggia and E.G. Spencer, “A new technique in ferrite phase shifting for beam scanning of microwave antennas”, *Proc. IRE*, **45**, 1510-1517 (1957).

21. Gerald F. Dionne and Daniel E. Oates, “Tunability of Microstrip Ferrite Resonator in the Partially Magnetized State”, *IEEE trans. Magn.*, **33**, 3421-3423 (1997).

22. X. H. Zhu, J. M. Zhu, S. H. Zhou, Z. G. Liu, N. B. Ming, S. G. Lu, H. L. W. Chan, and C. L. Choy, “Recent progress of (Ba,Sr)TiO3 thin films for tunable microwave devices”, *Journal of Electronic Materials*, **32**, 1125-1134 (2003).

23. G. Subruamanyam, F. V. Keuls, and F. A. Miranda, “A K-band tunable microstrip bandpass filter using a thin film conductor/ferroelectric /dielectric multilayer configurations”, *IEEE Microw. Guided Wave Lett.*, **8**, 78 (1998).

24. B. Acikel, T. R. Taylor, P. J. Hansen, J. S. Speck, and R. A. York, “A new high performance phase shifter using $BaSrTiO_3$ thin films”, *IEEE Microw. Wireless Compon. Lett.*, **12**, 237 (2002).

25. G. Velu, K. Blary, L. Burgnies, A. Marteau, G. Houzet, D. Lippens, and J. C. Carru, "A 360^{o} BST phase shifter with moderate bias voltage at 30 GHz", *IEEE Trans. Microw. Theory Tech.*, **55**, 438 (2007).

26. Jayesh Nath, Dipankar Ghosh, Wael Fathelbab, Jon-Paul Maria, Angus I. Kingon, Paul D.Franzon, and Michael B. Steer, "An Electronically – Tunable Microstrip Bandpass Filter Using Thin – Film Barium Strontium Titanate Varactors", *IEEE Trans. Microwave Theory Tech.*, **53**, 2707-2712 (2005).

27. K. B. Chong, L. B. Kong, L. F. Chen, L. Yan, C. Y. Tan, T. Yang, C. K. Ong, T. Osipowicz, "Improvement of dielectric loss tangent of Al_2O_3 doped $Ba_{0.5}Sr_{0.5}TiO_3$ thin films for tunable microwave devices", *Journal of Applied Physics*, **95**, 1416-1419 (2004).

28. Yan L, Kong, L B, Chen L F, Chong K B, Tan C Y, and Ong C K, $Ba_{0.5}Sr_{0.5}TiO_3$-$Bi_{1.5}Zn_{1.0}Nb_{1.5}O_7$ composite thin films with promising microwave dielectric properties for microwave device applications. Appl. Phys. Lett. 2004, 85, 3522-3524.

29. M. W. Cole, C. Hubbard, E. Ngo, M. Ervin, M. Wood, R. G. Geyer, "Structure-property relationships in pure and acceptor-doped $Ba_{1-x}Sr_xTiO_3$ thin films for tunable microwave device applications", *J. Appl. Phys.* **92**(1), 475-483 (2002).

30. S. Saha, S. B. Krupanidhi, "Large reduction of leakage current by graded-layer La doping in $(Ba_{0.5}Sr_{0.5})TiO_3$ thin films", *Appl. Phys. Lett.*, **79**(1), 111-113 (2001).

31. T. G. In, S. Baik, S. Kim, "Leakage current of Al- or Nb-doped $Ba_{0.5}Sr_{0.5}TiO_3$ thin films by rf magnetron sputtering", *J. Mater. Res.*, **13**(4), 990-994 (1998).

32. Z. Yuan, Y. Lin, J. Weaver, X. Chen, C. L. Chen, "Subramanyam G, Jiang J C, Meletis E I, Large dielectric tenability and microwave properties of Mn-doped $(Ba,Sr)TiO_3$ thin films", *Appl. Phys. Lett.*, **87**, 152901-1-3 (2005).

33 M. C. Chiu, H. C. Yao, C. J. Huang, F. S. shieu, "Improvement of dielectric properties of $Ba_{0.6}Sr_{0.4}TiO_3$ thin films by MgO doping", *J. Appl. Phys.*, **102**, 014110-1-8 (2007).

34. Q. X. Jia, B. H. Park, B. J. Gibbons, J. Y. Huang, P. Lu, "Dielectric response and structural properties of TiO_2-doped $Ba_{0.6}Sr_{0.4}TiO_3$ films", *Appl. Phys. Lett.*, **81**(1), 114-116 (2002).

35. M. W. Zhang, J. W. Zhai, X. Yao, "Tunable and microwave dielectric properties of $Ba_{0.5}Sr_{0.5}TiO_3$-$BaWO_4$ composite ceramics doped with Co_2O_3", *Materials Research Bulletin*, **45**(12), 1990-1995 (2010).

36. D. W. Peng, J. R. Cheng, Z. Y. Meng, "Low dielectric dissipation and enhanced tunability of $Ba_{0.6}Sr_{0.4}TiO_3$ thin films by the modified composition and multilayer structure", *Journal of Electroceramics*, ***21***, 668-671 (2008).

37. W. F. Qin, J. Xiong, J. Zhu, J. L. Tang, W. J. Jie, Y. Zhang, Y. R. Li, "Enhanced electrical properties of multilayer $Ba(Zr_{0.2}Ti_{0.8})O_3$/ $Ba_{0.6}Sr_{0.4}TiO_3$/$Ba(Zr_{0.2}Ti_{0.8})O_3$ thin films for tunable microwave applications", *Journal of Materials Science*, **43** (1), 409-412 (2008).

38. W. Fu, L. Cao, D. Wang, J. Miao, J. Qi, H. L. W. Chan, C. L. Choy, "Dielectric properties $Ba_{1.5}Zn_{1.0}Nb_{1.5}O_7$/Mn-doped $Ba_{0.6}Sr_{0.4}TiO_3$ hetero-layered films grown by pulsed laser deposition", *Appl. Phys. Lett.*, **89**, 132908-1-3 (2006).

39. Ai Huang, "Recent advances in dielectric materials". *NOVA*, New York, (2009).

40. M. E. Lines and A.M. Glass, "Principles and application of ferroelectrics and related materials", *Clarendon press*, Oxford Eng., (1977).

41. A. K. Tagantsev, "Permittivity, tunability and losses in ferroelectrics for reconfigurable high freauency electronics", In: Setter N (Ed) *Electroceramic Based MEMs*, Springer, (2005).

42. N. M. Alford, S. J. Penn, A. Templeton, X. Wang, J. C. Gallop, N. Klein, C. Zuccaro, and P. Filhol, *IEE Colloquium on Electro-Technical Ceramics—Processing, Properties and Applications*, pp. 9/1-9/5 (1997).

43. S. Gevorgian, "Ferroelectrics in microwave Devices, Circuits and Systems", *Springer*, London, (2009).

44. B. York, "Tunable Dielectrics for RF Circuits. In: M. Steer, and W. D. Palmer, Eds., Multifunctional Adaptive Microwave Circuits and Systems", *Scitech Publishing*, (2009).

45. P. Bao, T. J. Jackson, X. Wang, and M. J. Lancaster, "Barium strontium titanate thin film varactors for room temperature microwave device applications", *J. Phys. D: Appl. Phys.*, **41**, 1 (2008).

Chapter 2

FABRICATION AND MICROWAVE CHARACTERIZATION OF FERROELECTRIC THIN FILMS

2.1 Fabrication of Ferroelectric Thin Films

Most device fabrication requires sophisticated techniques for synthesizing high-quality oxide thin films to understand their unique physical properties and device performance. Current methods of fabricating ferroelectric thin films include: RF sputtering [1-2], Sol-gel method [3-4], molecular beam epitaxy (MBE) [5], metal-organic chemical vapor deposition (MOCVD) [6], and pulsed laser deposition (PLD) [7-9]. The first two provide polycrystalline or amorphous thin films, while the others can provide highly oriented thin films. Compared with other thin film deposition techniques, PLD shows several advantages, such as (1) the ability to reproduce the stoichiometry and crystallographic status of very complex bulk materials; (2) the relatively high growth rate of 1-5 Å/pulse and even higher; (3) an energy source independent of the deposition environment; (4) no ultrahigh vacuum requirements; (5) wide range of ambient reactive gas pressure, typically from 10^{-9} to 1 mbar; (6) relative simplicity of the growth facility offering great experimental versatility, e.g. using multi-targets and multi-component complex materials to produce multilayer or using dual-beam lasers to perform in-situ doping; and (7) reduction of film contamination due to the use of light for promoting ablation.

Today, PLD technique has become one of the most successful vapor deposition techniques in research and device applications. Besides all the advantages, there exist two main disadvantages for PLD technique: (1) splashing effect that causes particulate and droplets on the film surface; (2) narrow angular distribution of the species in the plume, which makes it difficult to fabricate large area film. Despite of the above drawbacks, PLD is an effective research tool because of its versatile deposition capability and ease of stoichiometry control. In this study, PLD is utilized to grow oxide thin films including BST thin films and electrode layer $La_{0.7}Sr_{0.3}MnO_3$ etc. Metal electrodes are deposited by RF magnetron sputtering and electroplated.

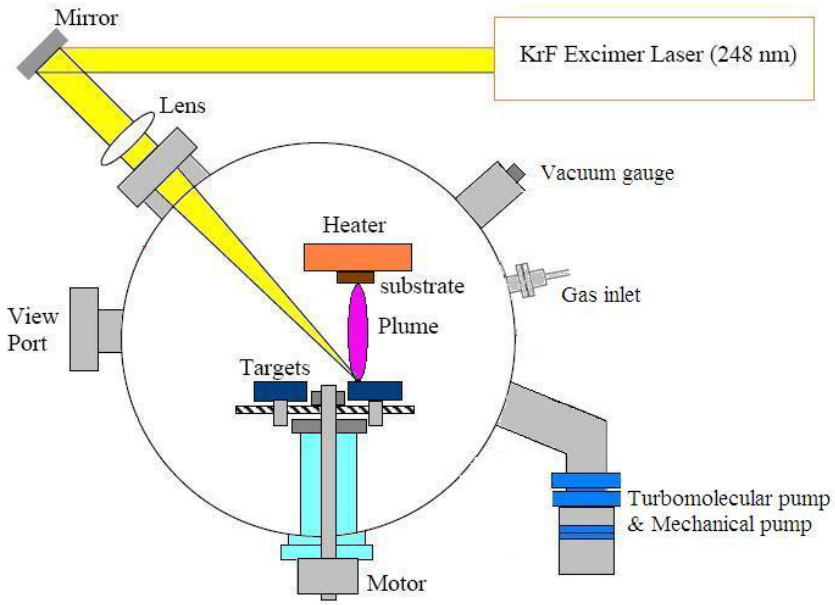

Figure 2.1 The schematic basic setup for PLD system for thin film fabrication.

2.1.1 Pulsed Laser Deposition Process

Pulsed laser deposition (PLD) is a physical vapor deposition technique where a high-power pulsed-laser beam is focused inside a vacuum chamber by a lens to strike a target of the desired composition. Figure 2.1 is a schematic diagram of the PLD system used in this project, where the whole setup includes a laser beam source and a stainless steel vacuum chamber with a rotating target holder and a substrate stage with a programmed-temperature controller. While the basic setup is simple compared to many other deposition techniques, such as vapor chemical deposition, magnetron sputtering, etc, the physical phenomena of laser-target interaction and film growth are quite complex. Details regarding its principles can be found from a number of sources in the literature [10]. For the laser system, the commercial LAMBDA PHYSIK excimer laser system is normally used to produce the KrF excimer high-energy laser. The laser beams are then guided using coated total reflection mirrors. After passing through a UV SiO_2 window on the chamber wall, the beams are finally focused onto the rotating ceramic target inside the high vacuum chamber.

The target holder is customized such that it can hold up to 2 different targets inside the chamber. This would enable us to grow different thin film layers without breaking the vacuum by rotating the holder to the desired target [11]. This would also help to keep the sample clean during the deposition. The rotation of the target during deposition to minimize the large particulate splashing effect and achieve a more uniform ablation of the target is driven using a small DC motor. Opposite the target holder, the substrates can be mounted on a stainless steel substrate heater in which the resistive filaments

are embedded. Silver paste is used to hold the substrates onto the holder and also for the efficient heat transfer between the substrates and the heater. A turbomolecular pump in combination with a mechanical pump is used to pump down the deposition chamber to a background pressure of less than 10^{-6} mbar. The reactive gas, O_2 in the case of fabricating oxide thin film, is injected into the chamber through a nozzle placed close to the target. Prior to the deposition of thin films, the target surface was polished using sand paper and pre-sputtered in PLD chamber. The substrates were first washed in the ultra-sonic bathing in the acetone for 10~15 minutes with the aim to remove oil molecular, fibers, and other contaminants on the surface. In order to have a clear picture of the PLD technique, one can divide the processes of PLD into three main stages: (1) interaction between laser and ceramic target surface, (2) interaction between species in the plasma plume and ambient gas, and (3) film growth on the substrate surface. As the process is repeated with more laser pulses, a thin film forms on the substrate surface, as shown in Figure 2.2.

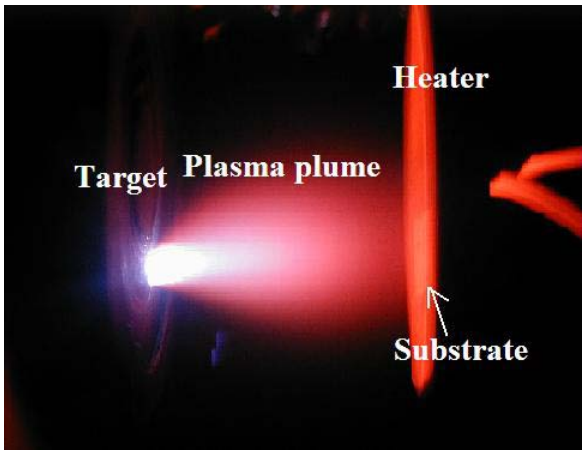

Figure 2.2 The shape of the plasma plume in PLD process.

2.1.2 Target Preparation and Thin Film Deposition Parameter Optimization

Most of the targets used in PLD were prepared using solid-state reaction method. Solid-state reaction is the most conventional synthesis method for preparing the multi-component targets. In this thesis, $Ba_{0.5}Sr_{0.5}TiO_3$ and $Ba_{0.25}Sr_{0.75}TiO_3$ targets with the diameter of about 2.5 cm were prepared using $BaTiO_3$, $SrTiO_3$ powders with ratio 1:1 and 1:3, respectively. The $BaTiO_3$ and $SrTiO_3$ powders were mixed and calcined at 950 °C for 1 h before they were compacted and sintered at 1350 °C for 4 h. As the BST thin films fabricated in this thesis were for the fabrication of microwave devices, the deposition parameters were optimized for the best crystal quality. $Ba_{0.5}Sr_{0.5}TiO_3$ had the maximum tunability, as well as relatively high dielectric loss at room temperature. $Ba_{0.25}Sr_{0.75}TiO_3$ exhibited low dielectric loss and permittivity well suited for the fabrication of low capacitance elements in devices. For comparison, the BST thin films with the different Ba/Sr ratio were grown on platinized silicon ($Pt/TiO_2/SiO_2/Si$) substrates and (100) $LaAlO_3$ (LAO) single crystal substrates using PLD with ceramic targets of $Ba_{0.5}Sr_{0.5}TiO_3$ and $Ba_{0.25}Sr_{0.75}TiO_3$, respectively. The BST thin films were deposited with the following optimized parameters: the distance between target and substrate is about 4.5 cm; a KrF excimer laser (λ=248 nm) of 3 Hz with the energy density of 1.5 Jm^{-2} was used; the temperature of substrate and oxygen pressure during the growth of BST films were kept at 700 °C and 0.2 mbar, respectively; the deposition time is about 30 minutes; after deposition, the samples were annealed for half an hour at about 650 ˚C in 1×10^3 mbar oxygen pressure.

2.2 Microwave Measurement Techniques for Ferroelectric Thin Films

Microwave measurements of the dielectric permittivity and loss tangent of a ferroelectric material is used (1) as initial data for the device design, (2) for the dielectric spectroscopy, e.g. for the analysis of the loss mechanisms, and (3) feedback information for the optimization for the composition and fabrication process. Therefore, it is very important to characterize the high frequency dielectric constant and tunability of ferroelectric materials for microwave applications. As ferroelectric materials may be in composite state, polycrystalline ceramic state, bulk single crystal state, and thin film state, different characterization methods are needed. For low frequencies (below some tens or hundreds of megahertz), the varactor which is made of any form of ferroelectric material is regarded as a lumped element since its dimensions are much less than the wavelength of the electromagnetic signal. The capacitance and loss tangent of the varactor can be measured directly by a standard impedance analyzer. At higher frequencies (RF/microwave), direct measurements of the capacitances are less applicable because, at higher frequencies, the dimensions of the varactors become comparable with the length of the electromagnetic wave and they cannot be considered any more as lumped elements. Generally speaking, the microwave measurement techniques for characterizing dielectric composites, ceramics and bulk ferroelectric crystals include nonresonant methods and resonant methods [12]. Ferroelectric thin films are usually characterized using planar-circuit methods, and almost all the dielectric properties, including the dielectric relaxations and electric tunability, are needed to be studied. In this section, we mainly discuss planar-

circuit measurement methods, including Lumped capacitance measurement method, coplanar waveguide transmission line method, and coplanar resonator method. The choice of which measurement technique to use is dependent on the final device architecture required for microwave application.

2.2.1 Lumped Capacitance Measurement Method

In this method, the ferroelectric thin film under study is fabricated into a capacitor. The dielectric constant of thin film is calculated from the capacitance of the capacitor, and the loss factor of the thin film is estimated from the quality factor of the capacitor. The two important aspects of this method are the capacitor design and the capacitance measurement.

Although ferroelectric thin film capacitors have been created in many different designs, they basically consist of two structural types: the parallel plate type (trilayer capacitor) and the coplanar type (e.g. interdigital capacitor). Figure 2.3 shows the configurations of the two types of ferroelectric thin film capacitor. Characterization of ferroelectric thin film capacitors at microwave frequencies is complicated by several factors. At these frequencies, series inductance associated with the electrode geometry introduces a self-resonant frequency that limits the useful measurement and operating bandwidth. The high capacitance density of the films also means that capacitors intended for use in this frequency range will have rather small electrode areas. Measurement interpretation is also more difficult, as new loss mechanisms become significant in the GHz range that may not be apparent at lower frequencies (dielectric relaxation processes, interfacial losses arising from

electron transfer between the electrodes and surface states, and skin-effect losses in the electrodes) [13]. Here, some reported on-wafer characterization methods will be discussed based on parallel plate capacitor and interdigital capacitor (IDC), respectively.

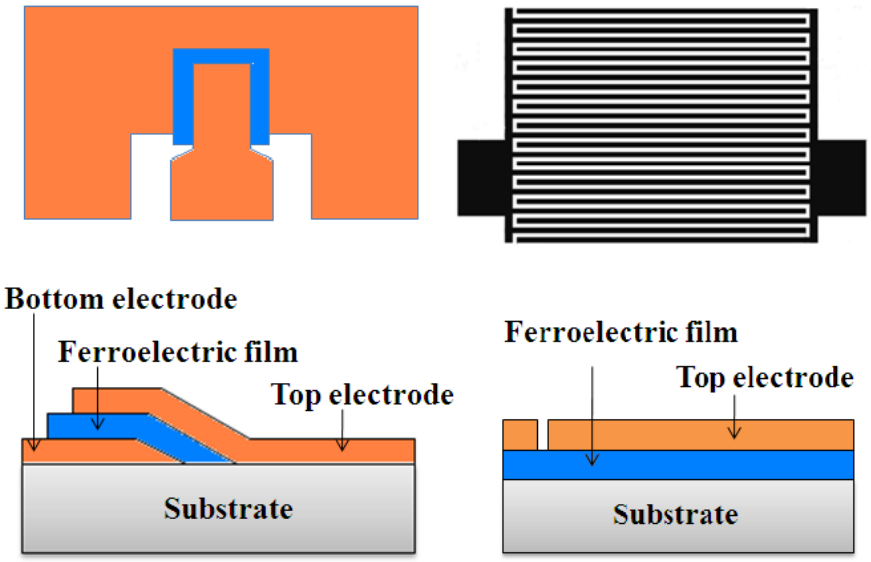

(a) (b)

Figure 2.3 The plane-view and cross sections of ferroelectric thin films capacitors. (a) Parallel plate capacitor; (b) interdigital capacitor.

(a) Parallel plate capacitor

A simple and commonly used test structure for one-port network analyzer measurement using ground-source-ground (GSG) probes has been proposed [14,15]. As shown in Figure 2.3 (a), the equivalent circuit of the capacitor can be expressed by lumped elements of intrinsic capacitor admittance, parallel and series stray admittances. The intrinsic capacitor admittance Y can be expressed in terms of S_{11} as:

$$Y = G + j\omega C = \frac{1}{Z_0}\left(\frac{1-S_{11}}{1+S_{11}}\right), \quad (2.1)$$

where *G* and *C* are the conductance and capacitance of the capacitor, ω is the measured angular frequency, S_{11} is the measured complex reflection coefficient from a vector network analyzer (VNA), and Z_0 is the characteristic impedance (50 Ω) of the transmission cable. The relative dielectric constant (ε_r) and dielectric loss tangent ($tan\ \delta$) of ferroelectric thin film can be derived from equation (2.1):

$$\varepsilon_r = \frac{C \cdot h}{A \cdot \varepsilon_0} \tag{2.2}$$

$$tan\delta = \frac{G}{\omega \cdot C} \tag{2.3}$$

A key issue encountered in evaluating the high-frequency dielectric properties of parallel plate capacitors is the accurate evaluation of parasitic. In particular, the series resistance that dominates high-frequency loss should be completely excluded to accurately estimate the dielectric loss. In the third chapter, a measurement method proposed by our group, to accurate evaluate microwave dielectric properties for parallel plate capacitors fabricated on BST thin film will be presented.

(b) Interdigital capacitor

In the interdigital capacitor (IDC) shown in Figure 2.3 (b), the substrate of the capacitor consists of two layers: ferroelectric thin film with dielectric constant ε_2 and the substrate with dielectric constant ε_1. Conformal-mapping-based models for IDC on layered substrates have been applied to the device data [16]. By definition, these models are only applicable at frequencies which are sufficiently low that the device is electrically small. The relative dielectric constant of the ferroelectric thin film can be calculated given the geometry of the IDC, the thickness of the ferroelectric thin film, the thickness and

dielectric constant of the substrate, and the measured capacitance. The IDC is modeled by a parallel resistor-capacitor model [17] for which the admittance reads

$$Y = Y_0 \frac{1-S_{11}}{1+S_{11}} = j\omega C \tag{2.4}$$

where Y_0 is the reference admittance and S_{11} is the reflection coefficient of the calibrated device. C is defined here as complex capacitance, where $Re[C]$ is the usual capacitance and $Im[C] = -G/\omega$, where G is the conductance.

A multifinger ($n > 3$) capacitor can be taken as a combination of a three-finger capacitor and (n - 3) periodical sections. The total capacitance, as decomposed by applying the partial-capacitance technique (PCT), is

$$C = C_3 + C_n + C_{end} \tag{2.5}$$

where C_3 is the capacitance of the three-finger capacitor, C_n is the capacitance of the (n-3) periodical sections, and C_{end} is the correction term of the finger fields at the ends of the strips. Each partial capacitance is expressed as the product of a known factor, depending only on the IDC geometry, and a partial dielectric constant of the form

$$\varepsilon_{eff,x} = 1 + \frac{1}{2} q_{1,x}(\varepsilon_1 - 1) + \frac{1}{2} q_{2,x}(\varepsilon_2 - \varepsilon_1) \tag{2.6}$$

In this linear expression, the index x stands for 3, n and end. $q_{1,x}$ and $q_{2,x}$ are filling factors depending only on the IDC geometry. For a given capacitor, its capacitance can be calculated according to the equations discussed above. By comparing the measurement results and the calculation results, the dielectric properties of ferroelectric thin film can be obtained.

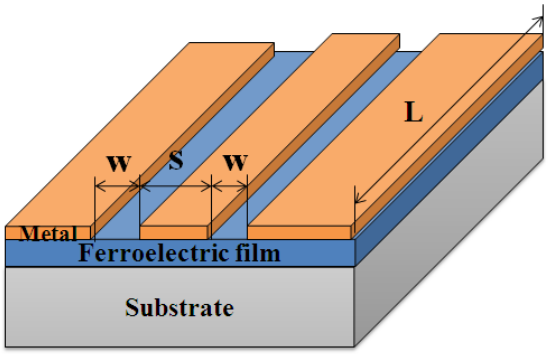

Figure 2.4 Schematic of a coplanar waveguide (CPW) on ferroelectric thin film.

2.2.2 Coplanar Waveguide Transmission Line Method

The coplanar waveguide (CPW) structure here consists of three layers from bottom to top: the substrate, the ferroelectric thin film and the conductors formed a center strip separated by a narrow gap from a pair of ground planes on either side, as shown in Figure 2.4. The dielectric permittivity values of the substrate and the ferroelectric thin film are ε_1 and ε_2 respectively. Conformal mapping is a fast tool for determining the impedance and effective dielectric permittivity in a microstrip circuit. The effective dielectric permittivity (ε_{eff}) of the CPW structure shown in Figure 2.4 may be expressed as follows [18]:

$$\varepsilon_{eff} = 1 + q_1(\varepsilon_1 - 1) + q_2(\varepsilon_2 - \varepsilon_1) \tag{2.7}$$

with the filling factors q_i, involving the transmission-line dimension, thickness of the film, and thickness of the substrate, given by

$$q_i = \frac{1}{2}\frac{K(k_i)}{K'(k_i)}\frac{K'(k_0)}{K(k_0)} \qquad (i = 1,2) \tag{2.8}$$

where

$$k_0 = \frac{s}{s+2w} \tag{2.9}$$

$$k_1 = \frac{\sinh(\pi s/4h_1)}{\sinh(\pi(s+2w)/4h_1)} \tag{2.10}$$

$$k_2 = \frac{\sinh(\pi s/4h_2)}{\sinh(\pi(s+2w)/4h_2)} \tag{2.11}$$

and *w* and *s* are the gap size and center strip width of the CPW transmission line, h_1 is the substrate thickness, h_2 is the thickness of ferroelectric thin film, $K(x)$ is elliptical integral of the first kind, and $K' \equiv K(\sqrt{1-x^2})$.

The characteristic impedance (Z_0) is

$$Z_0 = \frac{30\pi}{\sqrt{\varepsilon_{eff}}} \frac{K'(k_0)}{K(k_0)} \tag{2.12}$$

According to equation (2.7), the contribution of the thin film to the total effective dielectric constant is directly proportional to the q_2. In other words, the q_i factor is a measure of the proportionality of electromagnetic energy inside each dielectric layer.

When the transmission line has good impedance matching with the system characteristic impedance [19], the propagation constant can be directly calculated from the transmission coefficient S_{21} by

$$\alpha = -\frac{S_{21}}{l} \ (dB/cm) \tag{2.13}$$

$$\beta = -\frac{\Delta\emptyset_{S_{21}}}{l} \ (rad/cm) \tag{2.14}$$

$$\Delta\emptyset_{S_{21}} = -\frac{2\pi\sqrt{\varepsilon_{eff}} \cdot f \cdot l}{c} \tag{2.15}$$

where α is the attenuation constant, β is the propagation constant, *f* is the frequency, and *l* is the length of transmission line. The effective dielectric constant ε_{eff} is related to the phase delay of the CPW transmission line $\Delta\emptyset_{S_{21}}$.

With the knowledge of the substrate material, the physical dimensions of the CPW transmission line and the measured phase delay of the CPW line, the

dielectric constant of ferroelectric thin film can be determined using equations given above.

The total loss of the CPW structure includes the conductor loss, the ferroelectric thin film loss, the substrate loss and potentially radiation loss. The loss of substrate (e.g. Al_2O_3, MgO) is very low at the microwave frequencies; therefore the substrate loss is negligible. Also radiation loss is negligible because the CPW line width is much shorter than the operation wavelength. The total CPW loss is mainly due to the conductor loss and the ferroelectric thin film loss, as given by

$$\alpha = \alpha_c + \alpha_{FE} \tag{2.16}$$

The conductor loss can be calculated [20, 21] by

$$\alpha_c = \frac{8.86R_s b^2}{16Z_0K^2(k)(b^2-a^2)}\left(\frac{1}{a}\ln\left(\frac{2a}{\Delta}\frac{b-a}{b+a}\right)+\frac{1}{b}\ln\left(\frac{2b}{\Delta}\frac{b-a}{b+a}\right)\right)\ (dB/m) \tag{2.17}$$

where $a = s/2$, $b = (s + 2w)/2, \Delta = t/4\pi e^{\pi}$, R_s is the surface resistance of the metal, Z_0 is the characteristic impedance, and t is the metal thickness.

The total effective loss tangent is also given by

$$\varepsilon_{eff}tan\delta_{eff} = q_1\varepsilon_1 tan\delta_1 + q_2\varepsilon_2 tan\delta_2 \tag{2.18}$$

If the substrate loss is neglected, the loss tangent of ferroelectric thin film ($tan\delta_2$) is given by

$$tan\delta_2 = (\varepsilon_{eff}tan\delta_{eff})/(q_2\varepsilon_2) \tag{2.19}$$

The ferroelectric loss tangent is related to the dielectric attenuation constant by

$$\alpha_{FE} = 0.91\sqrt{\varepsilon_{eff}}f(GHz)tan\delta_{eff} \quad (dB/cm) \tag{2.20}$$

If the conductor loss of the CPW structure with ferroelectric thin film is assumed to be the same as the CPW structure without ferroelectric thin film, the loss tangent of ferroelectric thin film can be obtained from equations (2.13)-(2.20).

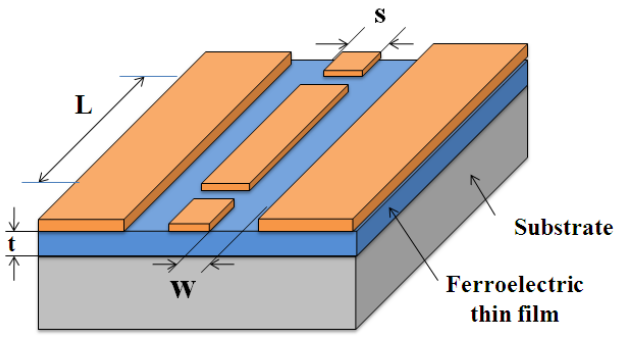

Figure 2.5 A ferroelectric thin film coplanar resonator.

2.2.3 Coplanar Resonator Method

Microwave resonators are often used to facilitate the evaluation of the material properties. Within this category, there are various kinds of resonators for different applications, such as cavity resonators, microstrip ring resonators, CPW half wavelength resonators and capacitively loaded resonators. Among them, planar circuit resonators are more attractive due to their ease of implementation, compact size and versatile design, as compared with the cavity resonators. A simple ferroelectric thin film coplanar resonator [22, 23] is shown in Figure 2.5, which consists of a length of coplanar transmission line open circuit at both ends. There is a ground plane at each side of the central conductor. The ferroelectric thin film is deposited on a substrate, and then the metal trace is deposited on the surface of the ferroelectric thin film. An expression for the total effective dielectric constant for the coplanar resonator is determined by

$$\varepsilon_{eff} = \left(\frac{c}{2f_0 \cdot L}\right)^2 \tag{2.16}$$

where c is the speed of light in vacuum, f_0 is the resonance frequency of the coplanar resonator, L is the length of the coplanar resonator. By applying a

similar analysis using conformal mapping as described in previous section, the dielectric permittivity of the ferroelectric thin film can be calculated by equation (2.7). The effective dielectric loss *tanδ* is determined from the unloaded quality factor of the ferroelectric thin film

$$tan\delta = \frac{2\Delta f}{f_0} \tag{2.17}$$

where *Δf* is the full width at half maximum of the resonance in the 3 dB.

The ways of applying bias voltage and controlling temperature for this method are quite similar to those for CPW transmission line method. However, in applying the bias voltage to the central conductor of the coplanar resonator, because the central conductor is not physically connected to the couplers, the bias voltage is often applied directly to the electric field node of the center conductor of the CPW structure. For a half-wavelength resonator, its electric field node is at the midpoint of the center conductor.

2.3 Experimental Measurement

The coplanar plate configuration is the typical structures used for microwave on-wafer characterization of the ferroelectric thin films. In this thesis, one-port reflection measurements using ferroelectric thin film varactors, including parallel plate varactor (out-of plane) and interdigital vractor (in plane), are used.

2.3.1 Preparation of Top Electrode Layer

Conductor material used in my research is gold (Au) thin film with chromium (Cr) buffer layer as top electrode layer of room temperature devices. Though copper (Cu) has recently been introduced in the semiconductor integrated chip (IC) industry for interconnect lines, limited work has been reported using it as an electrode material for thin film oxide based devices. This is due to its inherently poor adhesion and its tendency to oxidize and react in ambient atmosphere [24]. However, the material Au is suitable for microwave devices because of its high conductivity of 4.7×10^{7} $S\cdot m^{-1}$, as well as its chemical stability against moisture, heat, oxygen, and most corrosive chemicals. A thin Au/Cr seed layer is grown by RF magnetron sputtering deposition in sequence, which is followed by an electroplating process to grow thick Au layer. Then photo lithography and wet chemical etching are employed to pattern the top electrode.

(a) RF Sputtering deposition of Au/Cr seed layer

Sputtering deposition is a widely used processing technique for fabrication of metal and ceramic thin films [25]. Like pulsed laser deposition, sputtering deposition is also a physical vapor deposition process of thin films, in which gaseous ions collide with the target and atoms of target materials are removed and then condensed on the substrate surface. Usually magnetrons are used to confine electrons close to the surface of the target and produce more ionizing collisions with gaseous neutrals resulting in higher deposition rate.

In this study, the Au/Cr seed layers are deposited using the modified metal multilayer film magnetron sputtering system. The commercial target holder system (AJA Company) was used. Three different target holders are inside the chamber. This would enable us to grow different thin film layers without breaking the vacuum by changing the desired target holder and also help to keep the sample clean during the deposition. The distance between the target and the sample is around 25 cm. The chamber can be pumped down to a vacuum of around 3×10^{-7} Torr by two turbo molecular pumps backed by two rotary pumps, respectively. For our study, firstly an about 20 nm Cr thin layer is deposited using the 2″ magnetron sputtering gun at RF energy of 100 W for 2 minutes in an ambient argon pressure at 2×10^{-3} Torr, then an about 30 nm Au thin film is deposited on the surface of it using the 3″ magnetron sputtering gun at RF energy of 80 W for 3 minutes.

(b) Electroplating of Au thick layer

The electroplating processes are carried out in a self-constructed electroplating system. The beaker containing the commercial gold electroplating solution Microfab® AU 100 (Electroplating Engineers of Japan) is put in a water bath at the temperature of 60^{o}C. The solution was continuously stirred to keep uniform concentration. An Au wire is used as the anode, while the sample with seed layer is the cathode. Before electroplating, the sample is immersed in Microfab® bump cleaner (Enthone, Inc., USA) for 1 minutes and then washed using distilled water. The electroplating is carried out in a constant current mode. The magnitude of the current is proportional to the area of the sample exposed to the plating solution by a coefficient of 5 mA·cm^{-2}. At this current density, 8~10 minutes of plating will produce 1.5~2 μm thick Au thin film, which is the commonly used thickness in our room temperature microwave devices.

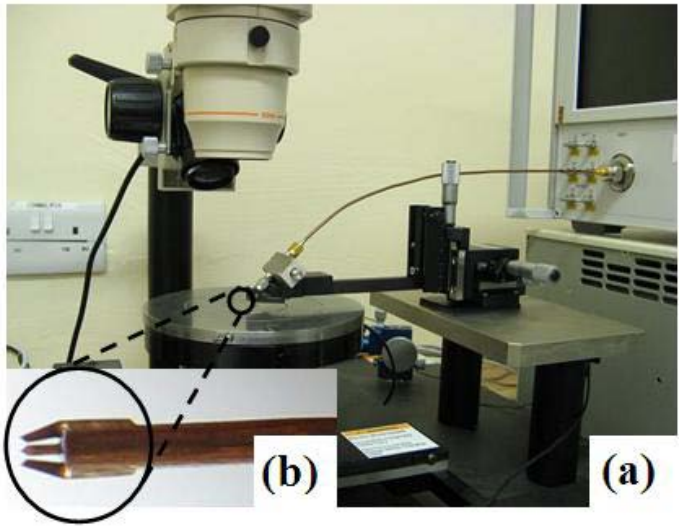

Figure 2.6 The photograph of one-port measurement setup (a) and a magnified image of GSG microprobe (b).

2.3.2 Measurement Setup

The microwave properties are measured in a one-port configuration using a PNA Series Network Analyzer (Agilent N5230A). A ground-signal-ground (GSG) coplanar waveguide microprobe with a pitch of 150 μm (GGB Industries, Model 40A) mounted on XYZ stage is used for this purpose. Pasternack PE1611 bias tee is used to supply dc bias voltage on picoprobe. Figure 2.6 shows the photograph of on-wafer measurement setup. Prior to measuring, one-port OSL (open, short, 50 Ω load) calibration is performed using a commercial standard calibration substrate (CS-5, GGB Industries). The experimental results of microwave measurement will be discussed in the next chapter.

References:

1. P. Padmini, T. R. Taylor, M. J. Lefevre, A. S. Nagra, R. A. York, J. S. Speck, "Realization of high tunability barium strontium titanate thin films by rf magnetron sputtering", *Appl. Phys. Lett.***75**, 3186 (1999).

2. T. Riekkinen T, J. Saijets, P. Kostamo, T. Sajavaara, S. Van Dijken, "Influence of Substrate Bias on the Structural and Dielectric Properties of Magnetron-Sputtered $Ba_xSr_{1-x}TiO_3$ Thin Films", *Ferroelectrics*, 392, 3-12 (2009).

3. V. A. Vasiljev, K. A. Vorotilov, M. I. Yanovskaya, L. I. Solovjeva, and A. S. Sigov, "Sol-gel derived barium-strontium titanate films", *J. Sol-Gel Science Technol.*, **13**, 877-883 (1998).

4. J. Yang, P.Yu, D. Q. Xiao, C. Tang, M. Chen, "The Fabrication of Highly (100)-Oriented $Ba_{0.8}Sr_{0.2}TiO_3/LaNiO_3$ Multilayers via Sol-Gel Method", *Ferroelectrics*, **406**, 90-96 (2010).

5. P. S. Anderson, S. Guerin S, B. E. Hayden, M. A. Khan, A. J. Bell, Y. Han, M. Pasha, K. R. Whittle, I. M. Reaney, "Synthesis of the ferroelectric solid solution, $Pb(Zr_{1-x}Ti_x)O_3$ on a single substrate using a modified molecular beam epitaxy technique", *Appl. Phys. Lett.*, **90** (20), 202907 (2007).

6. K. Takahashi, M. Suzuki, T. Oikawa, T. Kojima, T. Watanabe, H. Funakubo, "MOCVD of single-axis c-oriented strontium bismuth titanate thin films and their electrical properties", *Chemical Vapor Deposition*, **12**(2-3), 136-142 (2006).

7. L. Yan, L. B. Kong, C. K. Ong, "Pulsed laser deposition and characterization of $Bi_{3.25}Nd_{0.75}Ti_3O_{12}$ thin films buffered with $La_{0.7}Sr_{0.3}MnO_3$ electrode", *Materials Letters*, **58**, 2953-2957 (2004).

8. S. G. Lu, X. H. Zhu, C. L. Mak, K. H. Wong, H. L. W. Chan, C. L. Choy, "High tunability in compositionally graded epitaxial barium strontium titanate thin films by pulsed-laser deposition", *Appl. Phys. Lett.*, 82, 2877 (2003).

9. C. V. Varanasi, K. D. Leedy, D. H. Tomich, G. Subramanyam, "Large area $Ba_{1-x}Sr_xTiO_3$ thin films for microwave applications deposited by pulsed laser ablation", *Thin Solid Films*, **517**, 2878 (2009).

10. D. B. Chrisey and G. K. Hubler, "Pulsed Laser Deposition of Thin Films", *John Wiley & Sons*, (1994).

11. S. Y. Xu, C. W. Tan and C. K. Ong, "Designs of multi-target carousels for pulsed-laser deposition systems", *Meas. Sci. & Tech.* **9**, 1912 (1998).

12. L. F. Chen, C. K. Ong, C. P. Neo, V. V. Varadan, and V. K. Varadan, "Microwave electronics: measurement and materials characterization", *John Wiley & Sons, Ltd*, (2004).

13. R. A. York, "Tunable Dielectrics for RF Circuits", In: M. Steer, W. D. Plamer, eds., Multifunctional Adaptive Microwave Circuits and Systems. *Scitech Publishing*, (2009).

14. K. Ikuta, Y. Umeda, and Y. Ishii, "Upper-bound frequency for measuring mm-wave-band dielectric characteristics of thin films on semiconductor substrates", *Jpn. J. Appl. Phys.*, **37**, 210 (1998).

15. Y. Iwazaki, K. Ohta, T. Suzuki, "Elimination of parasitic effects due to measurement conditions of SrTiO3 thin films up to 40 GHz", *J. European Ceramic Society*, **26**, 1841 (2006).

16. S. S. Gevorgian, T. Martinsson, P. L. J. linner, and E. L. Kollberg, "CAD Models for Multilayered Substrate Interdigital Capacitors", *IEEE Transactions on Microwave Theory and Techniques*, **44**(6), 896 (1996).

17. S. W. Kirchoefer, J. M. Pond, A. C. Carter, W. Chang, K. K. Agarwal, J. S. Horwitz, and D. B. Chrisey, "Microwave properties of $Sr_{0.5}Ba_{0.5}TiO_3$ thin-film interdigitated capacitors", *Microwave Opt. Technol. Lett.*, **18**(3), 168–171 (1998).

18. S. S. Gevorgian, "Basic Characteristics of Two Layered Substrate Coplanar Waveguides", *Electron. Lett.*, **30**(5), 1236 (1994).

19. H. T. Lue, T.Y. Tseng, "Application of on-wafer TRL calibration on the measurement of microwave properties of $Ba_{0.5}Sr_{0.5}TiO_3$ thin films", *IEEE Trans. Ultrason., Ferroelectr., & Freq. Control*, **48**(6), 1640 (2001).

20. K. C. Gupta, "Microstrip Lines and Slotlines (2nd ed.)", Boston, MA: *Artech House*, (1998).

21. C. L. Holloway and E. F. Kuester, "A quasi-closed form expression for the conductor loss of CPW lines, with an investigation of edge shape effects", *IEEE Trans. Microwave Theory Tech.*, **43**(12), 2695 (1995).

22. P. M. Suherman, T. J. Jackson, and M. J. Lancaster, "Comparison of techniques for microwave characterization of bst thin films", *IEEE Trans. Microw. Theory Tech.*, **55**(2), 397 (2007).

23. M. J. Lancaster, J. Powell, and A. Porch, "Thin-film ferroelectric microwave devices", *Superconductor Science & Technology*, **11**(11), 1323 (1998).

24. W. Fan, B. Kabius, J. M. Hiller, S. Saha, J. A. Carlisle, O. Aucielle, R. P. H. Chang, R. Ramesh, "Materials science and integration bases for fabrication of (Ba_xSr_{1-x}) TiO_3 thin film capacitors with layered Cu-based electrodes", *J. Appl. Phys.*, **94**, 6192 (2003).

25. J. E. Mahan, "Physical Vapor Deposition of Thin Films", *Wiley*, New York, USA, (2000)

Chapter 3

FERROELECTRIC THIN FILM VARACTORS

3.1 Introduction

Varactors are voltage tunable capacitors in which the capacitance is dependent on a voltage applied thereto. This property can find applications in electrically tuning RF circuits, such as filters, phase shifters, and so on. The most commonly used varactor is semiconductor diode varactor, which has the advantages of high tunability and low tuning voltage, but suffers low quality factor Q, low power handling capability, and limited capacitance range at high frequencies [1]. A new type of varactor is a ferroelectric varactor, whose capacitance is tuned by varying the dielectric constant of a ferroelectric material by changing the bias voltage. Ferroelectric thin film varactors (especially BST) have high Q factor, high power handling capacity, and high capacitance range [2]. Also, ferroelectrics do not produce junction noise in comparison with the reverse biased junction in semiconductor varactor diodes.

Two different types of varactors, parallel plate (vertical) or interdigital (coplanar), are possible using ferroelectric thin films. The devices schematics for both configurations of devices are shown in Figure 2.3 (a) and (b). For the interdigital varactors, BST films are directly deposited on the appropriate substrate followed by top interdigital electrode metallization. In general, interdigital devices are simple to fabricate and integrate into microwave circuits since it requires only single step metallization compared to the parallel plate configuration. But interdigital varactors suffer from reduced tunability

(due to large fringing electric field in the air) and higher control voltages. Having smaller spacing between the fingers can further increase available tunability at lower voltages. However the ability to fabricate small finger spacing depends on the type of substrate and the photolithographic resources available. Typical operating voltages for interdigital varactors are in the range of 100 V with a typical tunability of 2:1.

In comparison with the coplanar configuration reported by Kim et al [3], parallel plate varactors reported by Stauf's group and York's group offer lower control voltage and higher tunability [4-6]. For parallel plate varactors, BST thin films are deposited on the bottom electrode on the substrate. The distance between the electrodes is basically the BST thin film thickness and therefore much shorter than the finger spacing in the interdigital configuration. Since the electric fields in parallel plate varactor are well confined within the ferroelectric film, as compared to the interdigital varactor where only a portion of the electric field is confined within the film, the control voltages in the case of parallel plate varactors are much less than that of interdigital varactors [7]. Moreover, the integration of tunable components on industrially important Si substrates can be easily achieved with parallel plate varactors [8-10]. These properties make the parallel plate varactors attractive for applications in consumer products. That's why our research interests have mainly focused on the development of parallel plate varactor and based microwave tunable devices.

3.2 Parallel Plate Varactors

In this section, a procedure to accurate evaluate microwave dielectric properties for parallel plate varactors fabricated on BST thin film deposited by PLD on Platinized silicon substrate is represented; and effect of bottom electrodes on dielectric properties of high frequency $Ba_{0.5}Sr_{0.5}TiO_3$ parallel-plate varactor is investigated.

3.2.1 Characterization of Microwave Dielectric Properties of BST Parallel Plate Varactors

The measurement of dielectric properties at microwave frequency in the parallel plate structure is complicated because the loss from the metal electrodes and the lead strips connecting to the electrodes will be significant and the parasitic inductance L in the device under test (DUT) will affect the apparent capacitance. Several high-frequency characterization techniques of thin-film dielectrics in the parallel plate structure have been proposed [11-14]. The main purpose of these measurement techniques is the removal of parasitics, such as parasitic inductance and resistance generated by the electrodes. The simplest test structure, as shown in Figure 3.1, was found to be the best for the characterization of the dielectric properties of BST thin films used in parallel plate type varactors. This method was first proposed by Ma et al [12] and modified by Gevorgian's group [13]. One of the advantages of this test structure is the minimized parasitic R and L. It is also the easiest for fabrication. The parallel plate varactors, which are the simplest test structure,

were prepared by one-step lithography process to study the dielectric properties of BST thin films.

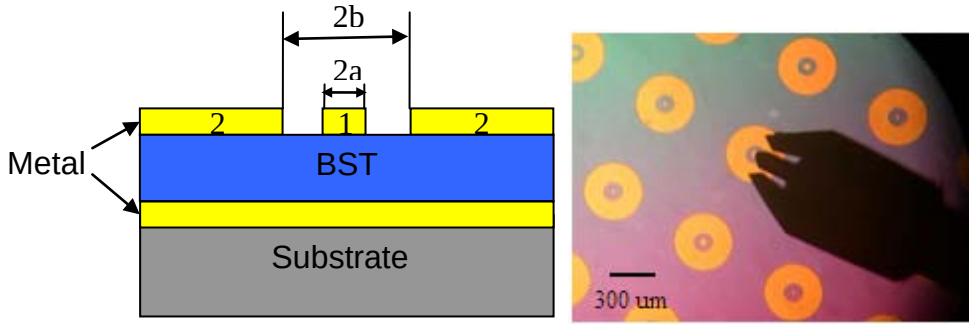

(a) (b)

Figure 3.1 The cross section of the varactor (a) and the photograph of the measurement setup using a GSG coplanar waveguide probe (b).

However, there are little reliable data on the high-frequency dielectric properties of these tunable dielectric thin films, due to the difficulty of completely removing the parasitics. Therefore, the purpose of this work is to seeking computer experiments based on Maxwells equations to examine the unknown equivalent parasite impedance used in evaluating permittivity from experimental measurements based on a vector network analyzer (VNA). By the consistency of the computer experimental results and VNA experimental results with simple analytical model, we develop an accurate evaluation technique for microwave dielectric properties which is indispensable for optimizing tunable thin film materials. Next, the procedure to characterize the microwave dielectric properties for parallel plate varactors is discussed in detail.

The deposition of $Ba_{0.25}Sr_{0.75}TiO_3$ thin films on the Platinized silicon (Pt /TiO_2 /SiO_2/Si) substrates and preparation of top electrode Au/Cr layer were

described in the chapter 2 in detail. Pt bottom electrode is selected due to a relatively high conductivity in combination with chemical and thermal stability, which is necessary in view of the subsequent high-temperature BST growth on the metal surface. The top electrodes were patterned as central circular patches surrounded by cocentric electrodes. Test structures with radii of the center patch a_1=20 μm and a_2=30 μm and the same outer radius b=60 μm were used in the experiments. The cross section of the varactor and the photograph of the measurement setup are shown in Figure 3.1.

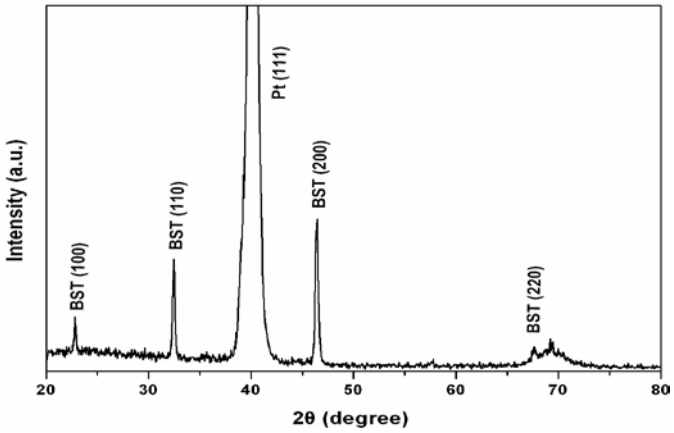

(a)

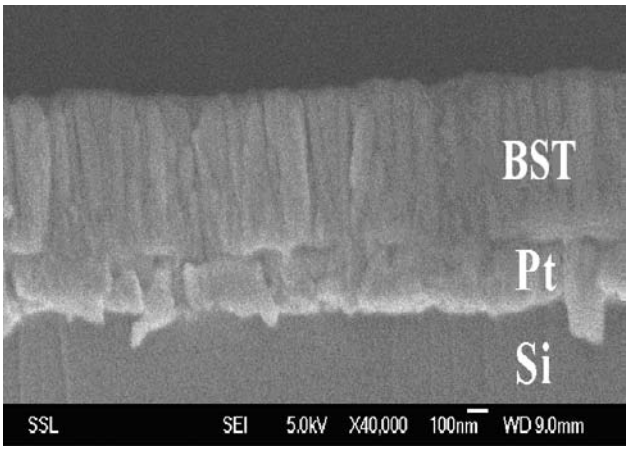

(b)

Figure 3.2 X-ray diffraction pattern (a) and cross sectional SEM image (b) of the BST film on Pt/Si substrate.

The formation of perovskite phase was confirmed by X-ray diffraction (XRD) using Philip automated powder diffractometer 1710 in θ-2θ configuration with a Cu Kα (λ=1.54060 Å) radiation operated at the following generator settings: 40 kV and 30 mA, as shown in Figure 3.2 (a). The microstructure was observed by scanning electron microscopy (SEM, JSM-6700F field emission SEM, Operating voltage of 5 kV). Figure 3.2 (b) shows the cross sectional SEM image of the BST film on Pt/Si substrate, by which the thickness of the BST film (~300 nm) was obtained. One-port reflection measurements of the parallel plate varactors at frequencies 10 MHz – 15 GHz were carried out, as described in the chapter 2. The high-performance full-wave electromagnetic field simulator, HFSS [15], which solves Maxwell's equations by a numeric simulation based on a finite element method, was used for simulating phase and the magnitudes of the S_{11} parameters.

A representative measured S_{11} reflection data curve is plotted in polar format in Figure 3.3 (a). These data were taken over the frequency range from 10MHz to 15GHz. In this polar format, the radius from the origin and the angle from $a+x$ axis represent the magnitude and phase of the S_{11} reflection data, respectively. The data span from the open-circuit point (1.0, 0.0) at low frequencies to near the short-circuit point (-1.0, 0.0) at high frequencies. The simulated S_{11} parameters were compared to the measured data to check the accuracy of the BST varactor parameters. Phase of the S_{11} as a function of frequency for measured data and HFSS simulation results are shown in Figure 3.3 (b). It is clearly seen that the simulation results exhibit good agreement with the experimental measurement. However, the discrepancy at high frequency is likely to stem from the parasitical effect of varactor, because

electric field is also distributed between the circular patch and the external electrode, shown in the inset of the Figure 3.3 (b) simulated by HFSS.

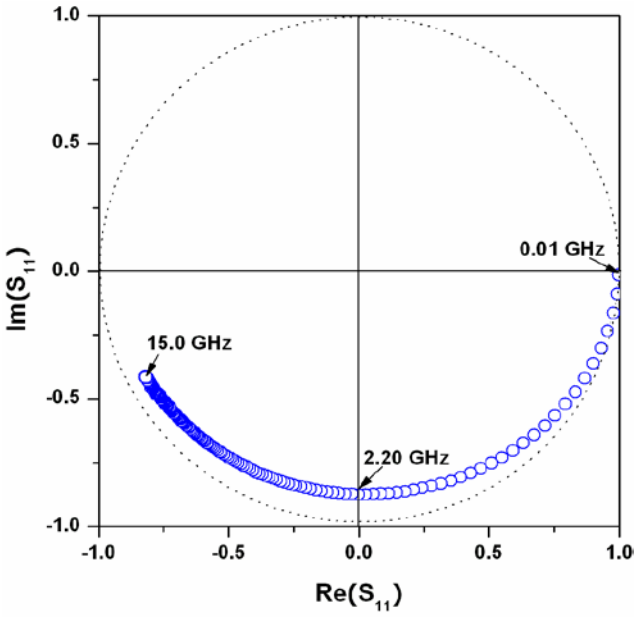

(a)

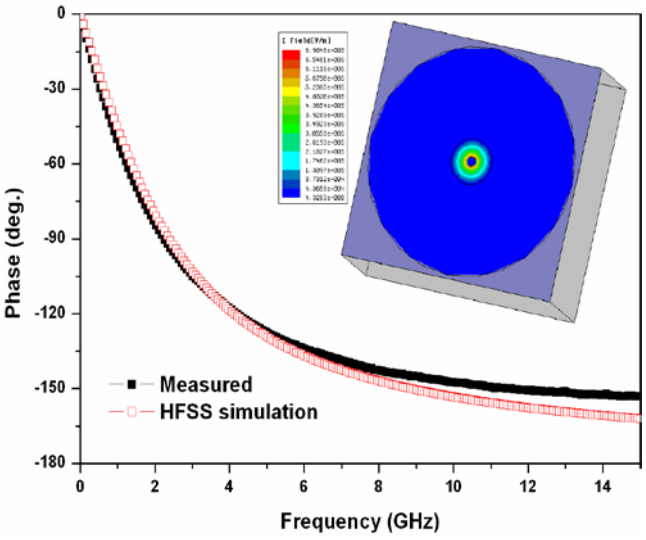

(b)

Figure 3.3 Measured S_{11} reflection data curve of varactor, plotted in polar representation (a) and phase of the S_{11} as a function of frequency for measured data and HFSS simulation results, inset shows the distribution of electric field in varactor using HFSS (b).

The measured reflection coefficients, S_{11}, are converted to impedance for test structure Z_{DUT} using a simple relationship:

$$Z_{DUT} = Z_0 \frac{1+S_{11}}{1-S_{11}} = R + jX \,, \tag{3.1}$$

where Z_0 is the characteristic impedance (50 Ω) of the transmission cable. In general, the capacitance C and the loss tangent tanδ are computed from the complex impedance $Z_{DUT} = R + 1/j\omega C$, $C = -1/\omega X$, $\tan\delta = -R/X$. However, the test structure is not a simple ideal parallel plate capacitor. The dielectric constant and loss tangent of the dielectric material can not be simply calculated from the measured capacitance value and loss of the test structure by using the area of the center patch and the thickness of the dielectric material. A simplified procedure of this type is used below to eliminate parasitic effects from the measured data [12].

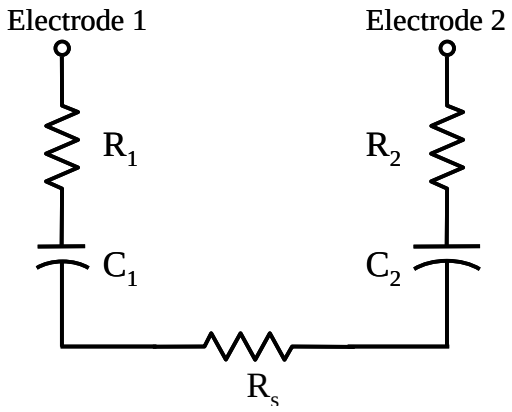

Figure 3.4 A simplified equivalent circuit of the parallel plate varactor.

The equivalent circuit of the test structure, assuming that the feature sizes of the test structures are much smaller than the wavelength of the microwave signal, is shown in Figure 3.4. C_1, C_2, R_1, R_2 represent capacitance and shunt resistance of the dielectric layer between the bottom electrode and top

electrodes corresponding to the circular patch and external electrode. R_S represents resistance in the bottom electrode between the circular patch and external electrode, which takes into account the parasitic resistances due to the outer ground. For the circuit of the Figure 3.4, it can be shown that:

$$Z_{DUT} = R_1 + R_2 + R_S + \frac{1}{j\omega}\left(\frac{1}{C_1} + \frac{1}{C_2}\right). \tag{3.2}$$

Equation (3.2) enables us to obtain the complex dielectric constant ($\varepsilon_r = \varepsilon_1 + j\varepsilon_2$) of the BST film experimentally by measuring two test structures with the same outer radius (b) but different inner radius (a_1, a_2) and assuming that R_S is the same in both cases.

$$\mathrm{Im}(Z^1_{DUT} - Z^2_{DUT}) = -\frac{1}{\pi\omega}\frac{d}{\varepsilon_0\varepsilon_r}\left(\frac{1}{a_1^2} - \frac{1}{a_2^2}\right), \tag{3.3}$$

where Z^1_{DUT} and Z^2_{DUT} are the measured impedances of the two test structures. The capacitance C_1 associated with the circular patch can be extracted from the impedance through the following the equation:

$$C_1 = \frac{\pi a_1^2 \varepsilon_r \varepsilon_0}{d} \tag{3.4}$$

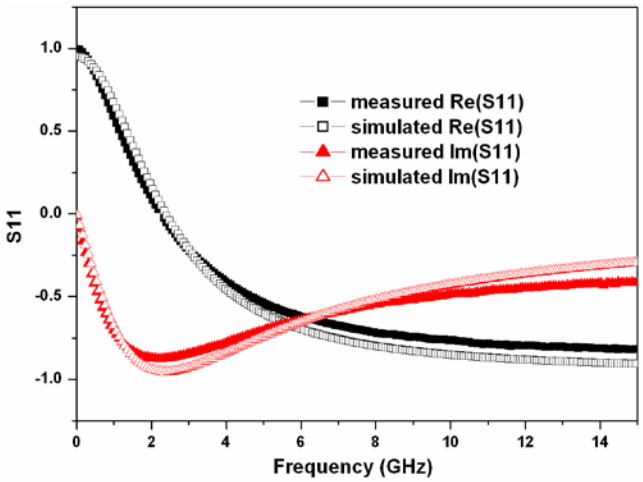

Figure 3.5 The simulated and measured real and imaginary parts of the S_{11} parameters of the varactor.

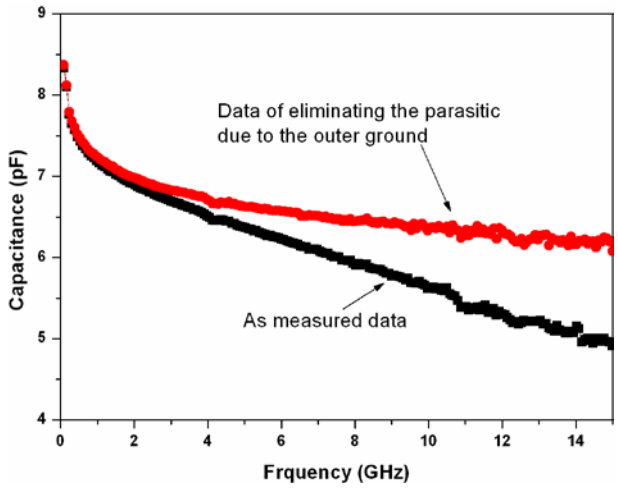

(a)

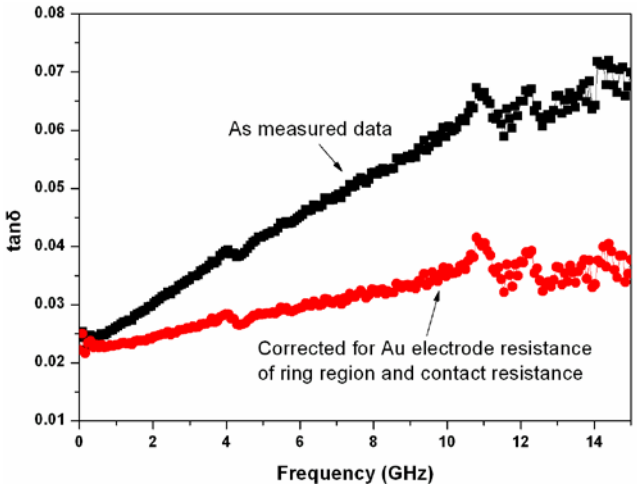

(b)

Figure 3.6 Frequency dependencies of capacitance (a) and loss tangents (b) of varactor before and after correction. The two test structures: a_1=20 μm, a_2=30 μm, b=60 μm.

In order to obtain the dielectric properties of the ferroelectric films at higher frequencies, the losses due to the finite sheet resistance of the bottom electrode and the parasitic resistances due to the outer ground need to be removed. The varactor was simulated with being matched to the circuit model, like the one in Figure 3.4. According to the equivalent circuit, a model, in which the resistances and capacitances were assigned lumped RLC boundaries on the wafer, was drawn in the HFSS. When a modest value of 0.6 Ω was

assumed for the R_S correction, a good agreement between measured and simulated data is observed, as shown in Figure 3.5. After subtracting the impedance of the two testing structures, by which the effect of the outer ground was eliminated, the R_S correction was given as the simulated value of 0.6 Ω. Figure 3.6 shows the capacitance and loss tangents versus frequencies for the varactor before and after correction. In Figure 3.6 (a), the capacitance C_1 calculated from the measured data rapidly decreases with increasing frequency, but the result from the two test structures shows the less frequency dependence, which seems to be explained by dielectric relaxation [16, 17].

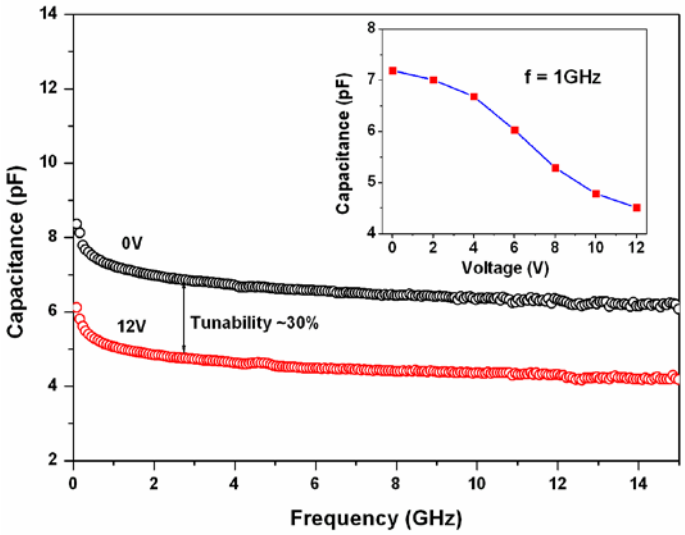

Figure 3.7 Frequency dependences of capacitance of varactor at *V*=0 and 12V. Inset shows the voltage dependence of capacitance of varactor at 1GHz.

Figure 3.7 shows the frequency dependence of the capacitance of the varactor at 0 and 12V dc bias. The permittivity of the BST film can be calculated from the equation (3.4) and it is fairly frequency independent in the range of 1 GHz - 15 GHz. One can define the tunability as following:

$$\text{Tunability} = \frac{C_0 - C_V}{C_0} \tag{3.5}$$

where C_0 is the capacitance at 0V and C_V is the capacitance at the bias of interest (12V here), the tunability of the capacitance at 12V bias is about 30% over the whole frequency range. The typical dependency of the capacitance of varactor on dc bias at 1GHz was shown in the inset of Figure 3.7. The varactor exhibits a characteristic of negative tunability of the capacitance, i.e., the capacitance decreases with increasing bias voltage.

The uncertainties of the measurements are now considered. Measurement uncertainty analysis requires taking into account contributions of both random and systematic errors [18]. The main contribution to the measurement error is from the uncertainty in measurement of the varactor structure dimensions, namely electrode radii and BST layer thickness. The main accuracy problems occur due to differential procedure of data processing using (3.3) and (3.4), where the results of two independent measurements are subtracted to get the permittivity of the film. In ref [19] uncertainty and electrode size related limitations associated with the evaluation of dielectric constant and loss tangent of ferroelectric thin films at microwave frequencies are discussed in detail.

3.2.2 Effects of Bottom Electrodes on Microwave Dielectric Properties of BST Parallel Plate Varactors

The bottom electrode materials greatly affect the electrical characteristic of the BST varactor [20]. Ferroelectric thin films grown on different substrates are subjected to in-plane deformation, usually called misfit strain. The misfit strain is mainly controlled by two contributions: the thermal strain due to the difference between thermal coefficients of the substrate and the strain due to mismatch of lattice parameters of ferroelectric film and substrate [21]. In this section, the effects of bottom electrodes to the dielectric properties in high frequency range from 10 MHz to 15 GHz were investigated. Three electrode structures have been developed to measure the dielectric properties of BST thin films in microwave range.

Three BST parallel plate varactors used $La_{0.7}Sr_{0.3}MnO_3$ (LSMO), Pt and Au as electrodes were fabricated on single crystal (001) $LaAlO_3$ (LAO) or (001) Si substrates. The resistance values of bottom electrode were varied while the thickness of BST thin film remained. For LSMO electrode varactor, the detailed structure is 400 nm BST on LSMO (800 nm)/LAO (001) substrate. For Pt electrode varactor, 400 nm BST thin film was grown in situ on Pt (200 nm)/Si commercial substrate. For Au electrode varactor, 400 nm BST thin film was grown on Au (2.5 μm)/Cr/Si substrate. $Ba_{0.5}Sr_{0.5}TiO_3$ thin films were grown using PLD as described in chapter 2. Au (with Cr buffer layer) was used as top electrode for all the three parallel plate varactors. Lithography and wet etching was employed to pattern the top electrode, as shown in Figure 3.1. The pattern has a circle (marked as number 1) and a ring (marked as number 2)

around the circle. The radius of the circle is 20 μm and the internal radius of the ring is 60 μm while external radius of the ring is 300 μm.

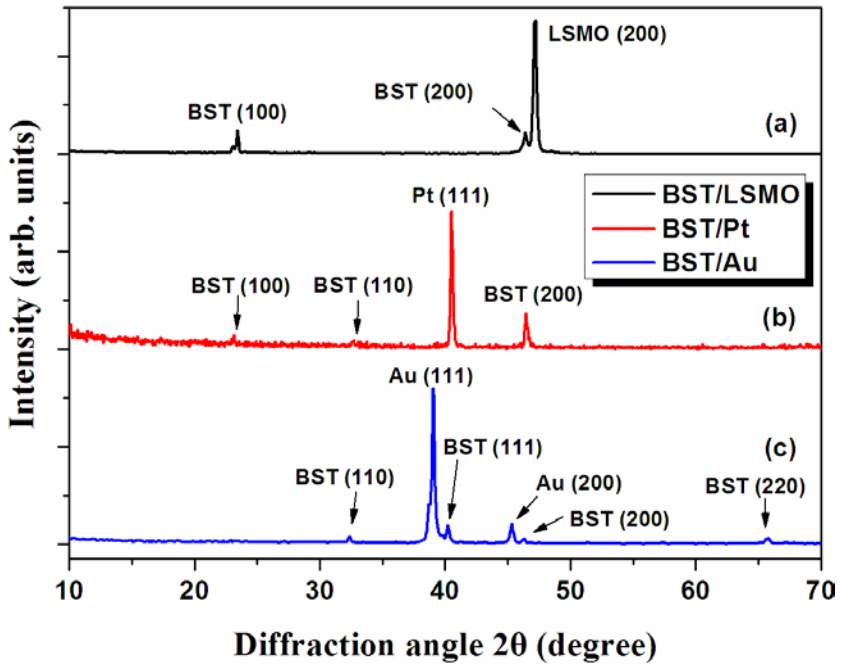

Figure 3.8 X-ray diffraction patterns of the BST films on different bottom electrode.

(a) Varactors Structure

The XRD patterns of the BST films on different bottom electrodes are shown in Figure 3.8. The cross section SEM images of the interface of the multi-layer thin film of the three varactors are shown in Figure 3.9, by which the thicknesses of the BST films were obtained. The Au bottom layer in BST/Au varactor is about 2.5 μm, approaching the gold skin depth at 10 GHz. Thus the effect of skin depth to the resistance is reduced significantly. The crystal orientation of the BST thin films is dependent on the bottom electrodes. Due to the very close lattice parameters of $Ba_{0.5}Sr_{0.5}TiO_3$ (a_{bulk} = 0.394 nm for bulk crystals) and Pt (0.392 nm), their (111) peaks are merged in Figure 3.8(b).

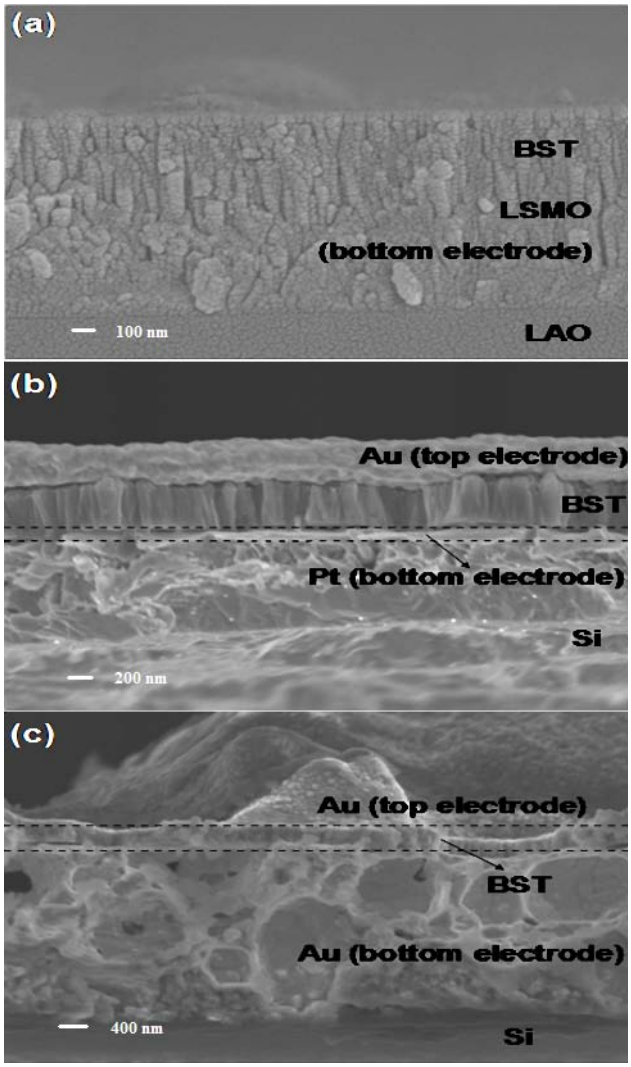

Figure 3.9 Cross section SEM images of BST/LSMO (a) BST/Pt (b) BST/Au (c) varactors.

The (00*l*) BST thin film was grown epitaxially on LSMO bottom electrode. The structures of BST thin films grown on LSMO and Pt bottom electrodes show columnar grains respectively, so the mismatch is very small. However, the BST thin film on Au has many X-ray peaks and the electrode-dielectric interface of the BST film grown on Au electrode is rougher than that deposited on Pt and LSMO electrodes. Many ferroelectric thin film properties are dependent on the quality of the grown film [22-23]. So, the bottom electrode has a pronounced effect on the dielectric properties of the BST films. The

identification of the BST peaks and the texture analysis are based on the comparison with Joint Committee on Powder Diffraction Standards (JCPDS) data [24].

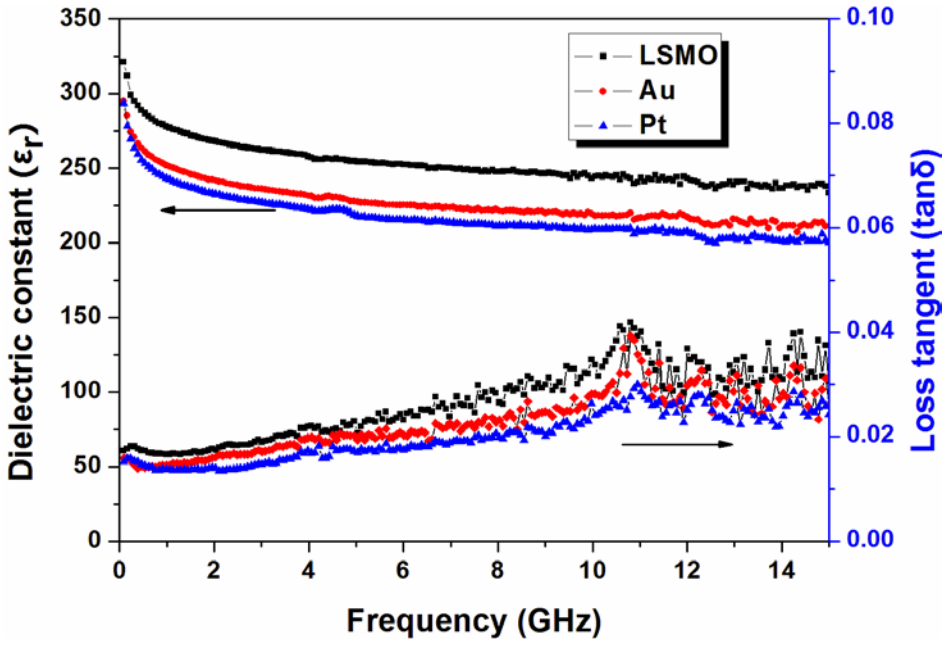

Figure 3.10 Dielectric constant and loss tangent of the BST thin films grown on LSMO, Au, and Pt bottom electrodes as a function of the measured frequency.

(b) The dielectric properties of BST thin films

The dielectric properties of the BST thin films grown on different bottom electrodes were measured using a parallel plate varactor configuration shown in Figure 3.1. The variations in the dielectric constant (ε_r) and loss tangent ($tan\delta$) of the BST thin films grown on three types of bottom electrodes as a function of frequency from 10 MHz to 15 GHz are shown in Figure 3.10. It is observed from three samples that the dielectric constant decreases slightly with increasing frequency, which is mainly associated with the negative calibration inductance. In addition, the defects in the BST films often lead to a

dielectric relaxation as a function of frequency, in which the dielectric constant decreases and loss tangent increases with increasing frequency [19]. The dielectric dispersions of BST thin films grown on LSMO, Au, and Pt bottom electrodes are low and these varactors are expected to have a high charge storage density even at high frequencies. It indicates that the BST thin film grown on LSMO bottom electrode has a maximum dielectric constant and a little higher loss tangent. One possible reason is that the dielectric properties are not only strongly related to the metal or oxide substrate but also the columnar or stacking grain texture in BST films. Another possible explanation is that a Schottky barrier exists at the ferroelectric/metal interface, which results in band-bending and a depletion layer depressing permittivity. The BST films can exhibit large dielectric constants due to polarization of electric dipoles. In general, large grain size, good crystallinity, and small space charge capacitance width can enhance the dielectric constant of the BST films [25, 26]. The BST thin film grown on LSMO electrode has large grain size that has been characterized by SEM observation. Besides, the BST thin film grown on LSMO electrode has smaller space charge width than that of Pt and Au because LSMO (work function 4.96 eV) has lower work function than Pt (5.6 eV) and Au (5.1 eV). Furthermore, rough surface of the bottom electrodes also enlarges the effective electrode area and shortens the effective thickness of the film capacitor, which could be one of the factors affecting the properties of the BST thin films. The higher dissipation factor of the BST thin film grown on LSMO electrode is mainly attributed to the higher resistive loss.

3.3 Comparison of Microwave Properties of BST Varactors with Parallel Plate and Interdigital Electrodes

At present, few studies have focused on the influence of the electrode form on the dielectric properties of columnar BST films both at low frequency and high frequency. In this section, we present a systematic investigation and comparison of the dielectric properties of columnar grown BST thin films based on the interdigital and parallel plate structures in the frequency range of 1 kHz to 10 GHz.

The $Ba_{0.5}Sr_{0.5}TiO_3$ (BST-0.5) and $Ba_{0.25}Sr_{0.75}TiO_3$ (BST-0.25) thin films were grown on the Pt (200 nm)/Ti/SiO_2/Si substrate and (001) $LaAlO_3$ (LAO) single crystal substrate, as described in chapter 2. The thickness of BST thin film were about 520 nm and 460 nm depositing on Pt and LAO substrates respectively, which were determined by cross sectional SEM images. The detailed parameters and dielectric properties of the parallel plate and interdigital varactors are presented in Table 3.1. The XRD measured results indicate that the BST-0.25 and BST-0.5 thin films grown respectively on the LAO and platinized Si substrates have a pure perovskite phase and exhibit good orientation [27].

Figure 3.11 displays the temperature dependence of permittivity for BST-0.5 and BST-0.25 thin film at the frequency of 10 kHz. The permittivity is calculated according to measured capacitance C with the equation $\varepsilon = Cd/\varepsilon_0 A$, where d is the thickness of the BST film and A is the area of electrode. With the increase of temperature, the permittivity reaches the maximum and drops quickly with the transition from the ferroelectric to paraelectric phase.

Table 3.1 The parameters and dielectric properties of the parallel plate and interdigital varactors

	Parallel plate varactor		Interdigital varactor	
	BST-0.5	BST-0.25	BST-0.5	BST-0.25
Measured frequency	1 GHz		1 GHz	
Top-Bottom electrodes	Au-Pt	Au-Pt	Au-	Au-
Area of Capacitance (mm^2)	0.04π	0.04π	-	-
Number of gaps	-	-	8	8
Width and gap of fingers (μm)	-	-	~10.5/9.5	~10/10
Length of fingers (μm)	-	-	180	180
Thickness of film (nm)	~400	~400	~460	~460
Applied dc voltage (V)	12	12	15	15
Capacitance (pF)	10.23	5.77	1.05	0.63
Dielectric constant	368	208	1428.6	714.7
Tunability	30.1%	21.4%	11.3%	8.2%
Loss tangent tanδ	0.016	0.012	0.0098	0.0047

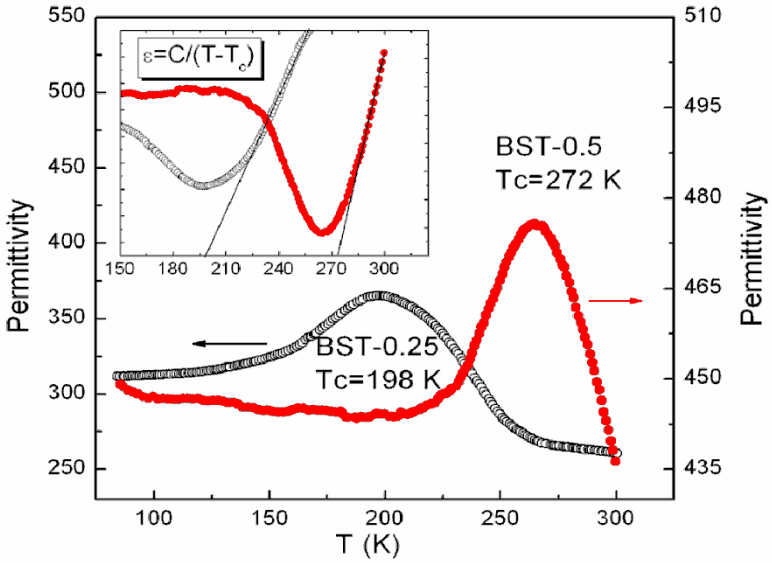

Figure 3.11 Permittivity of BST film as a function of temperature at *f*=10 kHz. The inset shows the inverse of permittivity with the temperature.

In order to determine Curie temperature T_c, the inverse of permittivity is plotted against temperature in the inset of Figure 3.11. Typically, the T_c will increase with the increase of Ba content in $Ba_xSr_{1-x}TiO_3$ material, and will be

changed with the variation of the film thickness [28]. In our experiments, T_c is found to be of 198 K and 272K for BST-0.25 and BST-0.5 from the temperature intercept of the straight line fitted to data above T_c. For the BST-0.25 sample, the permittivity decreases slowly with temperature in paraelectric phase, while the permittivity of the BST-0.5 drops sharply just above the T_c temperature. These indicate that the sample BST-0.5 will exhibit large tunability at room temperature.

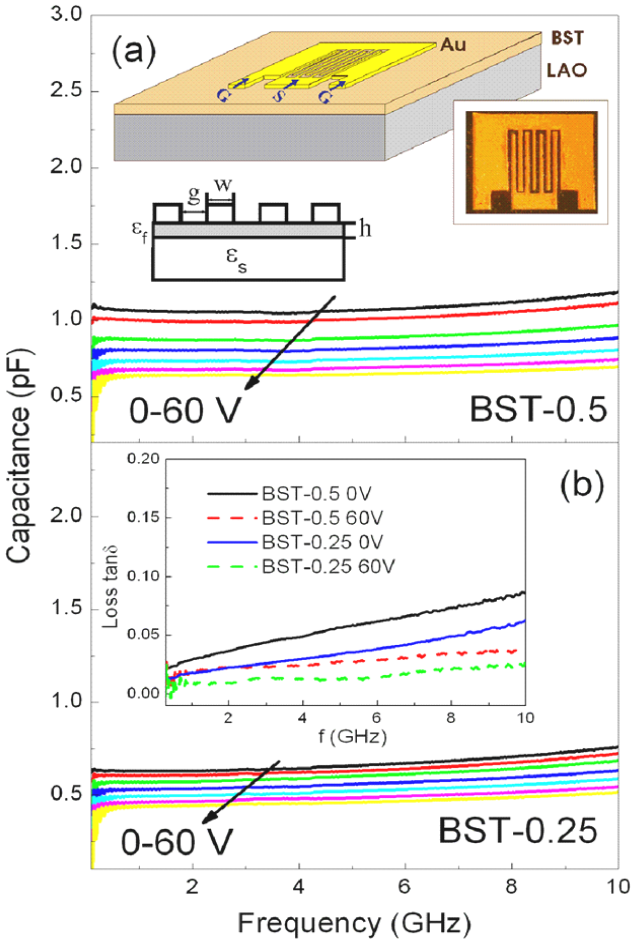

Figure 3.12 Capacitance as a function of frequency for BST film under 0-60 V dc bias. The inset in (a) displays the schematic of interdigital capacitance and the inset in (b) shows the loss tangent with a variation in frequency at different dc voltage.

Figure 3.12 (a) displays the capacitance of the BST film with interdigital structure as a function of frequency up to 10 GHz and dc bias from 0 to 60 V. The microwave dielectric properties can be calculated according to the measurement method of interdigital capacitor presented in chapter 2. The obtained capacitance of BST-0.5 and BST-0.25 are about 1.05 Pf and 0.63 Pf at zero dc bias, respectively. The dielectric losses with the variation of frequency and at the different dc voltages are shown in the inset of Figure 3.12 (b). The tanδ of BST-0.5 increases from 0.022 to 0.086 between 0.1-10 GHz, and the tanδ of BST-0.25 changes from 0.014 to 0.061. The capacitance and the dielectric loss tangent decrease with the increase of the applied voltages. Based on the Tagantsev et al. model [29], this behavior of dielectric loss can be explained by mechanism of energy scattering on the ferroelectric model that is related to the relaxation of phonon distribution function. At the same time, one can observe that the capacitance of BST interdigital varactor exhibit good frequency independent characteristics below 8 GHz, and increases slowly with the frequency further increasing. It is believed that the increased capacitance with frequency results from the resonant of LCR circuit due to a small amount of inductance existing in the interdigital capacitor and test circuit. The resonant frequency in C-*f* curve is found near at 19 GHz (not shown in Fig. 3.12). Thus, the inductance of system can be roughly estimated at 0.067 nH from $f = 1/\sqrt{2\pi(LC)}$.

We used the HFSS software to simulate the S-parameter and phase shift for interdigital varactor, as shown the lines in the Figure 3.13. Inset shows the distribution of the electric field in the interdigital capacitor when the dc voltage is applied. The high electric field was observed to be concentrated on

the edges of the conducting fingers and the vectors of the electric field between fingers mainly exists in the in-plane of the BST film. It is clearly seen that the simulation results exhibit good agreement with the experimental results. However, the discrepancy at high frequency is likely to have stemmed from the parasitical effect of varactor and a small amount of inductance in the actual interdigital varactor. Furthermore, the actual dimension of interdigital fingers and gaps are difficult to determine accurately after electroplating, which may also result in the discrepancy between simulation and experiments.

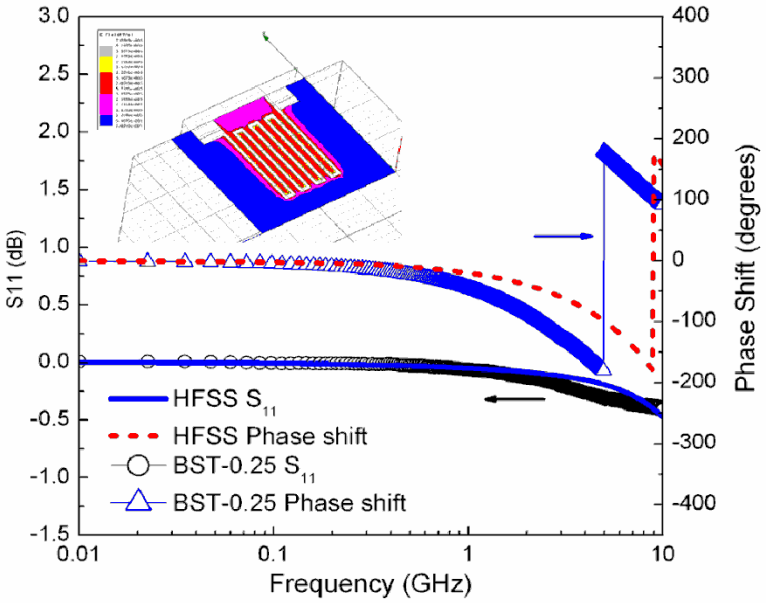

Figure 3.13 S_{11} and phase shift as a function of frequency for HFSS simulation results and sample BST-0.25. The inset shows the distribution of electric field in interdigital varactor using HFSS.

When the dc bias was applied, the capacitance of interdigital varactor decreased with the applied voltage leading to the desired tunability. Figure 3.14 shows the dc bias dependences of capacitance at the frequency of f=1 GHz. The tunability τ reached 42.4% and 29.7% for BST-0.5 and BST-0.25 at 60 V dc bias, respectively. Since the in-plane tunability of BST film is

sensitive to the width of gap in interdigital structure and the type of substrate, therefore, it is difficult to compare our present results with other studies [30]. However, the present tunability remains comparable with that of $\tau = 60\%$ at 40 V and $\tau = 48\%$ at 200 V in BST-0.5 thin film deposited on LAO substrate [31].

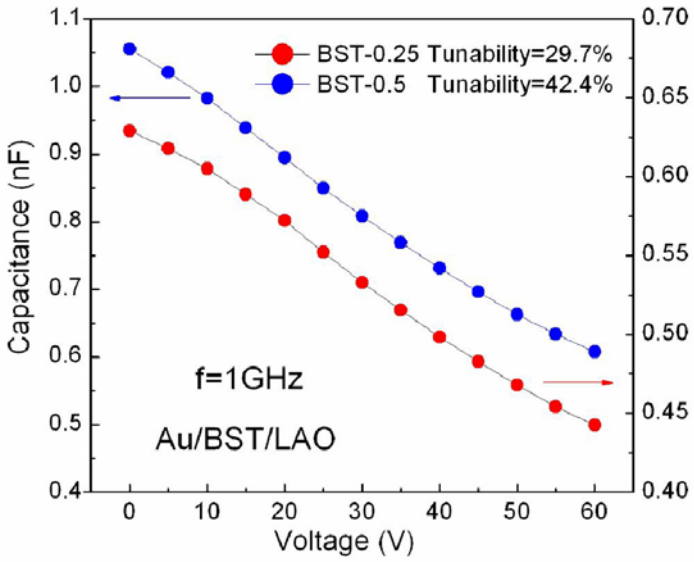

Figure 3.14 dc bias field dependent capacitance of BST film in the interdigital structure at the frequency of 1 GHz.

Figure 3.15 (a) shows the capacitance of BST film with parallel plate structure as a function of frequency up to 10 GHz with and without DC bias. The method of microwave characterization has been presented in previous section (3.2.1). The results show good frequency independent characteristics in the wide frequency range. The permittivity of BST-0.5 and BST-0.25 in parallel structure was about 368 and 208 respectively at *f*=1 GHz. Remarkably, the tunability for samples of BST-0.5 and BST-0.25 reach 30.1% and 21.4% respectively under 12 V DC-bias. Such tunability is also remarkable and can be compared to $\tau = 40\%$ at 20 V for BST-0.25 and $\tau = 29\%$ at 12V for BST-0.5 film using Pt electrodes [32, 33]. However, the tunability in parallel plate

structure was much lower than 40% at 10 V as BST-0.25 depositing on $SrRuO_3$ bottom electrode [34]. Besides the high permittivity and tunability, the sample of BST-0.5 exhibited a large dielectric loss when compared to the sample of BST-0.25 in parallel plate structure. Moreover, the loss tangent showed a rapid increase in high frequency range, as shown in Figure 3.15 (b). The large loss tan δ at high frequency was considered a result of the microwave loss in the thin Pt bottom electrode with lower conductivity [8].

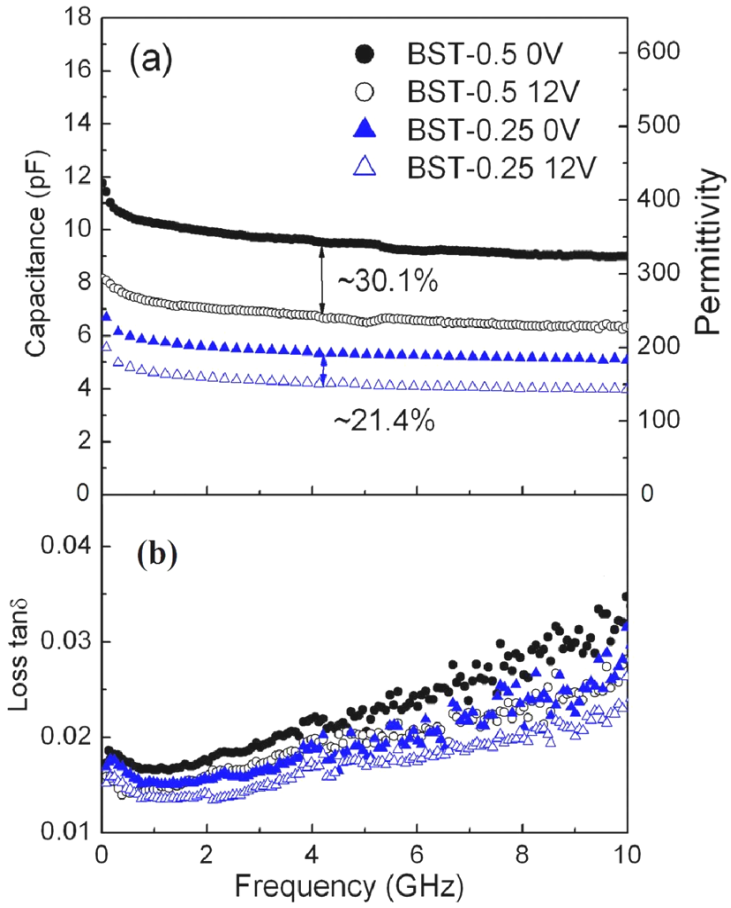

Figure 3.15 (a) Capacitance with a variation of frequency in parallel plate structure measurement under 0 and 12V. (b) Loss tangent as a function of frequency at different dc voltage.

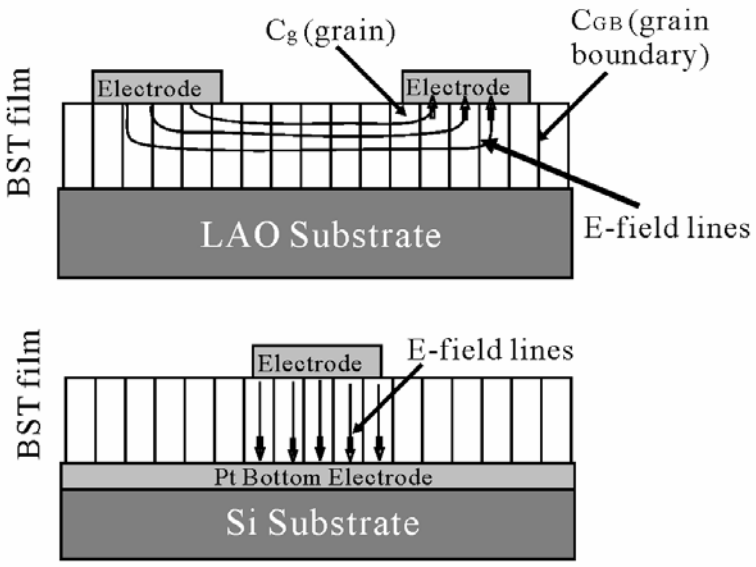

Figure 3.16 The conceptual diagram of columnar BST grain, grain boundary and electric field lines in coplanar and parallel-plate varactors.

The important findings are that significant dielectric dispersion and lower permittivity are observed in the parallel plate configuration in comparison with that in the interdigital configuration. It is generally accepted that the dielectric dispersion results from the interfacial polarization, namely the Maxwell–Wanger relaxation caused by space charge polarization in the film/electrodes interfaces. The grain boundaries had a lower permittivity compared with that of grains. As shown in Figure 3.16, the capacitance of grain C_g was in series with the grain boundary capacitance C_{gb} within the coplanar varactor, while C_g and C_{gb} was in parallel within the parallel-plate varactor. Hence the apparent permittivity of coplanar structures was strongly influenced by the grain boundaries and could be decreased by a traversing electric field.

3.4 Hybrid Varactors

3.4.1 Design with Coplanar and Parallel Plate Structures

As discussed in previous sections, coplanar varactors have relatively simple design and fabrication process, but suffer from reduced tunability; parallel plate varactors have higher capacitance and tunability compared with the coplanar type, however, the high capacitance hinders impedance matching, which is one of the most important issues in microwave device design. Recently, a possible solution has been proposed in our group by developing a hybrid varactor which integrates the features of both basic structures of coplanar and parallel plate varactors and hopefully maintains the merit of its component structures [35]. In this design, an ultra-thin film with low conductivity is used as dc bias bottom electrode and at the same time the electrode does not contribute in the electric field distribution of microwave signal. At microwave frequencies, the charge flow in high resistance films is slow against the fast oscillating electrical field, which makes low conductivity film electrode nearly “transparent” to microwave signal. A closed form analysis of the behavior of low conductivity thin film in microwave field was presented in ref [36], which demonstrates that the low conductivity ultra-thin film in this structure can be considered “transparent” at microwave frequencies. As a result, the dc parallel plate varactor circuit and the microwave coplanar varactor circuit could be non-interactive with each other, which lead to the hybrid varactor’s low bias voltage with relatively high tunability and low capacitance. Because of small separation between top and bottom of parallel plate electrode compared with separation between coplanar

electrodes (i.e. the gap of fingers of interdigital), when a dc bias is applied, the direction of the static electrical field is perpendicular to the low conductivity electrode. In ref [35], although the hybrid varctor with the LSMO dc bias electrode exhibited monotonically increasing frequency dependences as predicted, a low value of the quality factor of the varactor was shown. In our experiments, a BST thin film hybrid varactor with modified configuration and ZnO dc bias bottom electrode was fabricated and measured. The fabricated BST hybrid varactor showed a low capacitance and improved the tunability compared with the conventional coplanar varactor.

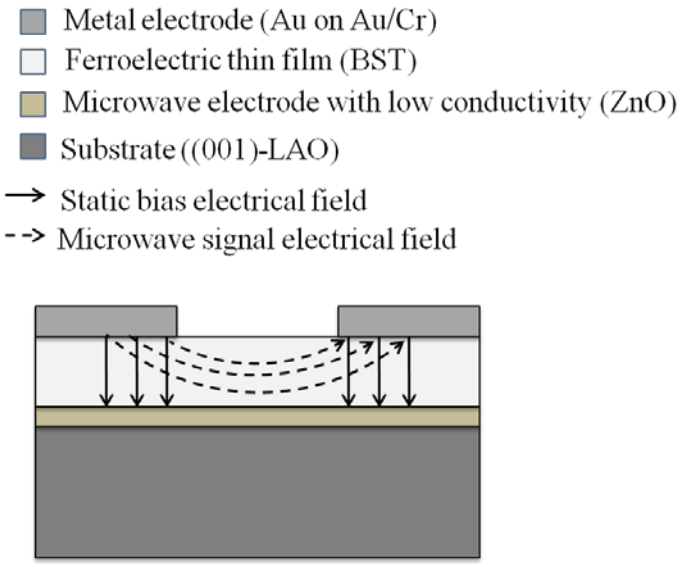

Figure 3.17 Layer structure of the hybrid varactor and orientation of electrical field lines in the varactor.

A modified hybrid varactor structure with coplanar and parallel plate electrodes and orientation of electrical field in the hybrid varactor are shown in Figure 3.17. In this new structure, the top low conductivity electrode layer was discarded and the interdigital metal electrode was used for the top

electrode of dc bias. At microwave frequencies, the microwave current established at low conductivity film electrode is small and orientation of microwave signal electrical field in the hybrid varactor is the same as that in the conventional coplanar varactor (as shown in Figure 3.16).

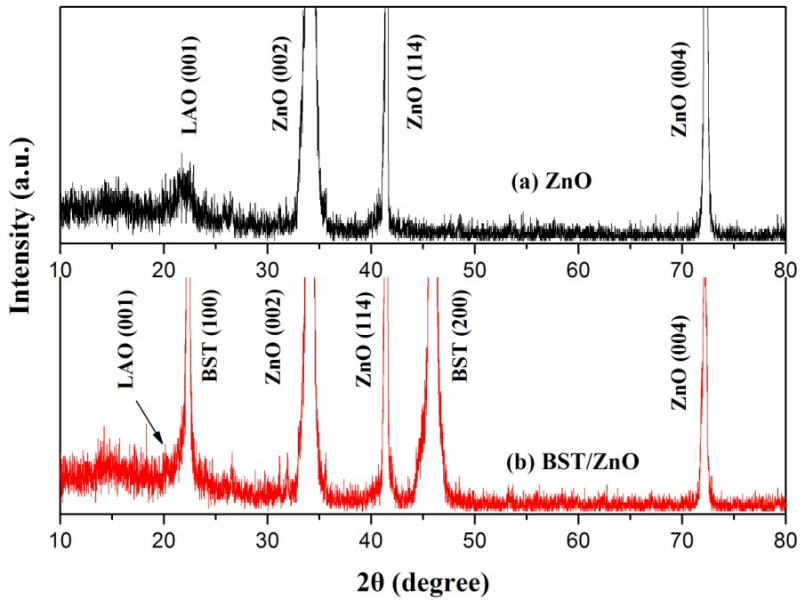

Figure 3.18 XRD patterns of the thin films (a) ZnO, (b) BST/ZnO on (001) LAO substrates.

3.4.2 Experiments and Results

For the fabrication of hybrid varactor, $Ba_{0.25}Sr_{0.75}TiO_3$ (BST) is used for the ferroelectric film layer. A low conductivity ZnO ultra-thin film is chosen as the bottom electrode for applying dc bias because of its preferential (001) orientation on a wide variety of plates [37]. The BST/ZnO thin films were grown in sequence on (001) $LaAlO_3$ (LAO) single crystal substrate of 5 mm × 10 mm × 0.5 mm using PLD with ceramic targets of ZnO and $Ba_{0.25}Sr_{0.75}TiO_3$.

The ZnO thin film was deposited using a KrF excimer laser of 5 Hz and 250 mJ for 15 minutes. The temperature of substrate and the oxygen pressure were kept at 510 °C and 1.2×10^{-3} mbar, respectively. The measured resistivity of these films by the conventional four-terminal method is about 0.01 Ω·cm. The parameters of BST deposition are the same as described in chapter 2. Figure 3.18 shows the XRD patterns of the ZnO and BST/ZnO thin films on (001) LAO substrates. Whereas the ZnO thin film showed preferential (001) orientation, there appeared one (114) reflection. The BST thin film showed (100)-oriented growth on the ZnO film layer. The top Au electrode (1.5 μm) was deposited and patterned as presented in chapter 2. The photograph of the hybrid varactor is shown in Figure 3.19. The two inner electrodes form an interdigital capacitor. The dimensions of this interdigital capacitor are: finger length = 90 μm, finger width = 28 μm, and gap = 20 μm. The outer electrode was designed for applying dc bias voltage.

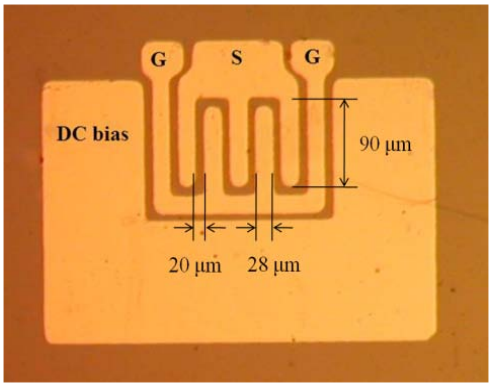

Figure 3.19 Photograph of the hybrid varactor. The marked interdigital electrode was used for one-port measurement and the outer electrode was designed for applying dc bias.

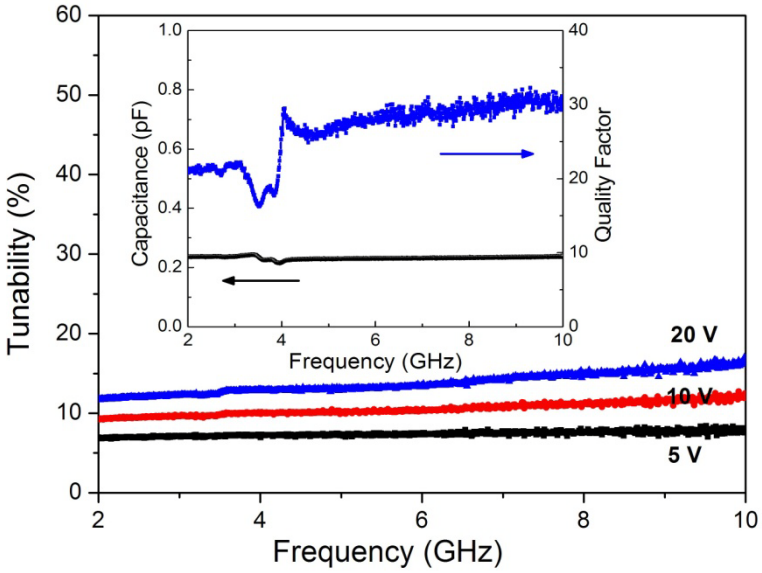

Figure 3.20 Tunability of the hybrid varactor at different bias voltages. Inset shows the capacitance and the quality factor of the varactor at zero bias.

The hybrid varactor was measured by VNA and dc bias voltage was applied between the outer electrode and interdigital electrode, while GSG port was shorted through a bias tee. Figure 3.20 shows the tunability of the hybrid varactor at different bias voltages in the frequency range from 2 GHz to 10 GHz. The inset shows the capacitance and the quality factor of the varactor without bias voltage. The fluctuation around 3 GHz should be caused by PNA Series Network Analyzer (Agilent N5230A). The tunability is larger than 12% at 20 V bias and the quality factor is about 30 at 10 GHz, which were improved significantly compared with the performances reported in ref [35]. The quality factor exhibits the abnormal increase with the increase of frequency as predicted ($Q = \omega CR$). However, the tunability is not high compared with conventional parallel plate varactor. The study on improving the tunability of the hybrid varactor structure is in progress.

3.4.3 Conclusion

The proposed hybrid varactor has improved the tunability of the conventional coplanar varactor by integrating a vertical dc bias electrode with low conductivity, which takes advantage of parallel plate varactor. This makes them good candidates for phase shifters and other microwave transmission devices. The hybrid varactor requires no bottom electrode patterning and low resolution for patterning of the microwave coplanar electrodes. This will significantly reduce the fabrication requirement and thus reduce the cost. The tunability of the hybrid varactor is relatively low for now, but it is expected to be improved by design optimization of hybrid varactor structure or alternative materials for low conductive bottom electrode. The low capacitance and the simplicity of fabrication of the hybrid varactor are suitable for microwave device integration applications.

References:

1. J. S. Horwitz, W. Chang, A. C. Carter, J. M. Pond, S. W. Kirchoeffer, D. B. Chrisey, J. Levy and C. Hubert, "Structure/property relationships in ferroelectric thin films for frequency agile microwave electronics", *Integr. Ferroelect*. **22**, 279 (1998).

2. S. Sheng, P. Wang, X. Y. Zhang and C. K. Ong, "Characterization of microwave dielectric properties of ferroelectric parallel plate varactor", *J. Phys. D: Appl. Phys.*, **42**, 015501 (2009).

3. W. J. Kim, W. Chang, S. B. Qadri, J. M. Pond, S. W. Kirchoefer, D. B. Chrisey and J. S. Orwitz, "Microwave properties of tetragonally distorted $(Ba_{0.5}Sr_{0.5})TiO_3$ thin films", *Appl. Phys. Lett.,* **76**, 1185 (2000).

4. A. Tombak, J. P. Maria, F. Ayguavives, Z. Jin, G. T. Stauf, A. I. Kingon and A. Mortazawi, "Tunable barium strontium titanate thin film capacitors

for RF and microwave applications", *IEEE Microw. Wirel. Compon. Lett*., **12**, 3 (2002).

5. R. A. York, A. S. Nagra, P. Periaswamy, O. Auciello, S. K. Streiffer and J. Im, "Synthesis and characterization of $(Ba_xSr_{1-x})Ti_{1y}O_{3z}$ thin films and integration into microwave varactors and phase shifters", *Integr. Ferroelectr.*, **34**, 177 (2001).

6. F. W. Van Keuls, R. R. Romanofsky, C. H. Mueller, J. D. Warner, C. L. Candy, R. Ramesh and F. A. Miranda, "Current status of thin film $(Ba,Sr)TiO_3$ tunable microwave components for RF communications", *Integr. Ferroelectr.*, **34**, 165 (2001).

7. M. W. Cole, C. V. Weiss, E. Ngo, S. Hirsch, L. A. Coryell, and S. P. Alpay, "Microwave dielectric properties of graded barium strontium titanate films", *Appl. Phys. Lett.*, **92**, 182906 (2008).

8. A. Vorobiev, P. Rundqvist, K. Khamchane and S. Gevorgian, "Silicon substrate integrated high Q-factor parallel-plate ferroelectric varactors for microwave /millimeterwave applications", *Appl. Phys. Lett.*, **83**, 3144 (2003).

9. F. Ahamed and G. Subramanyam, "Design of a Si MMIC Compatible Ferroelectric Varactor Shunt Switch for Microwave Applications", *14th IEEE International Symposium on Applications of Ferroelectrics*, p285 (2004).

10. T. G. Kim, J. Oh, Y. Kim, T. Moon, K. S. Hong and B. W. Park, "Crystallinity dependence of microwave dielectric properties in (Ba,Sr)-TiO_3 thin films", *Jpn. J. Appl. Phys.*, **42**, 1315 (2003).

11. K. Ikuta, Y. Umeda and Y. Ishii, "Measurement of high-frequency dielectric characteristics in the mm-wave band for dielectric thin films on semiconductor substrates", *Jpn. J. Appl. Phys.* **34**, L1211 (1995).

12. Z. X. Ma, A. J. Becker, P. Polakos, H. Huggins, J. Pastalan, H. Wu, K. Watts, Y. H. Wong and P. Mankiewich, "RF measurement technique for characterizing thin dielectric films", *IEEE Trans. Electr. Dev.* **45**, 1811 (1998).

13. A. Vorobiev, D. Kuylenstierna, P. Rundqvist and S. Gevorgian, *Proc. 36th European Microw. Conf. (Manchester,UK)*, p843 (2006).

14. T. Hamano, D. J. Towner and B. W. Wessels, "Relative dielectric constant of epitaxial BaTiO3 thin films in the GHz frequency range", *Appl. Phys. Lett.* **83**, 5274 (2003).

15. Ansoft HFSS 11, User Documentation, *Ansoft Corporation*, (2007).

16. S. Y. Hou, J. Kwo, R. K. Watts, J. Y. Cheng and D. K. Fork, "Structure and properties of epitaxial $Ba_{0.5}Sr_{0.5}TiO_3/SrRuO_3/ZrO_2$ heterostructure on Si grown by off-axis sputtering", *Appl. Phys. Lett.* **67**, 1387 (1995).

17. T. Moon, B. Lee, T. G. Kim, J. Oh, Y. W. Noh, S. Nam and B. Park, "Microwave dielectric relaxation of the polycrystalline (Ba, Sr)TiO_3 thin films", *Appl. Phys. Lett.* **86**, 182904 (2005).

18. P. K. Petrov, Y. Y. Pan, B. Zou and N. M. Alford, "Dielectric constant and loss tangent of thin ferroelectric films at microwave frequencies - How accurately can we evaluate them", *Integr. Ferroelectr.* **97**, 27 (2008).

19. P. Rundqvist, A. Vorobiev, S. Gevorgian and K. Khamchane, "Nondestructive microwave characterization of ferroelectric films on conductive substrates", *Integr. Ferroelectr.* **60**, 1 (2004).

20. M. S. Tsai, T. Y. Tseng, "Effect of bottom electrodes on dielectric relaxation and defect analysis of (Ba0.47Sr0.53)TiO3 thin film capacitors", *Mater. Chem. Phys.*, **57**, 47 (1998).

21. L. J. Sinnamon, M. M. Saad, R. M. Bowman, and J. M. Gregg, "Exploring grain size as a cause for "dead-layer" effects in thin film capacitors", *Appl. Phys. Lett.*, **81**, 703 (2002).

22. S. Razumov, A. Tumarkin, O. Buslov, M. Gaidukov, A. Gagarin, A. Ivanov, A. Kozyrev, Y.W. Song, and C.S. Park, "Electrical properties of magnetron sputtered thin BaSrTiO3 films depending on deposition conditions", *Integr. Ferroelect.*, **39**, 1317 (2001).

23. A. B. Kozyrev, V. N. Keis, G. Koepf, R. Yandrofski, O. I. Soldatenkov, K. A. Dudin, and D. P. Dovgan, "Procedure of microwave investigations of ferroelectric films and tunable microwave devices based on ferroelectric films", *Microelectron. Eng.*, **29**, 257 (1995).

24. JCPDS-Powder Diffraction File International Center for Diffraction Data, Card No. 39-1395, (1999).

25. M. M. Saad, P. Baxter, R. M. Bowman, J. M. Gregg, F. D. Morrison and J. F. Scott, "Intrinsic dielectric response in ferroelectric nano-capacitors", *J. Phys.: Condens. Matter*, **16**, L451 (2004).

26. L. W. Chang, M. McMillen, F. D. Morrison, J. F. Scott, J. M. Gregg, "Size effects on thin film ferroelectrics: Experiments on isolated single crystal sheets", *Appl. Phys. Lett.*, **93**, 132904 (2008).

27. X. Y. Zhang, P. Wang, S. Sheng, F. Xu, and C. K. Ong, "Ferroelectric $Ba_xSr_{1-x}TiO_3$ thin-film Varactors with Parallel-plate and Interdigital Electrodes for Microwave applications", *J. Appl. Phys.*, **104**, 124110 (2008).

28. M. Dawber, K. M. Rabe, J. F. Scott, "Physics of thin-film ferroelectric oxides", *Rev. Mod. Phys.*, **77**, 1083 (2005).

29. N. A. Pertsev, A. G. Zembilgotov, A. K. Tagantsev, "Effect of Mechanical Boundary Conditions on Phase Diagrams of Epitaxial Ferroelectric Thin Films", *Phys. Rev. Lett.*, **80**, 1988 (1998).

30. L. M. B. Alldredge, W. Chang, S. B. Qadri, S. W. Kirchoefer, and J. M. Pond, "Ferroelectric and paraelectric $Ba_{0.5}Sr_{0.5}TiO_3$ film structure distortions at room temperature and their effects on tunable microwave properties", *Appl. Phys. Letts.*, **90**, 212901 (2007)

31. X. H. Zhu, L. P. Yong, H. F. Tian, W. Peng, J. Q. Li and D. N. Zheng, "The origin of the weak ferroelectric-like hysteresis effect in paraelectric $Ba_{0.5}Sr_{0.5}TiO_3$ thin films grown epitaxially on $LaAlO_3$", *J. Phys.: Condens. Matter*, **18**, 4709 (2006).

32. A. Vorobiev, P. Rundqvist, K. Khamchane, and S. Gevorgian, "Microwave loss mechanisms in $Ba_{0.25}Sr_{0.75}TiO_3$ thin film varactors", *J. Appl. Phys.*, **96**, 4642 (2004).

33. A. Mahmud, T. S. Kalkur, A. Jamil, and N. Cramer, "A 1-GHz active phase shifter with a ferroelectric varactor", *IEEE Microwave and Wireless Components Letters*, **16**, 261 (2006).

34. K. Khamchane, A. Vorobiev, T. Claeson, S. Gevorgian, "$Ba_{0.25}Sr_{0.75}TiO_3$ thin-film varactors on $SrRuO_3$ bottom electrode", *J. Appl. Phys.*, **99**, 034103 (2006).

35. P. Wang, and C. K. Ong, "A novel microwave ferroelectric varactor with hybrid coplanar and parallel plate structure", *J. Phys. D: Appl. Phys.*, **42**, 195107 (2009).

36. P. Wang, "Microwave Miniature Ferroelectric Tunable Devices", Ph. D. thesis, National University of Singapore, (2009).

37. J. M. Liu, C. K. Ong, "Pulsed laser deposition of ZnO as conductive buffer layer of (001)-$LiNbO_3$ thin films", *Appl. Phys. A*, **67**,493 (1998).

Chapter 4

COPLANAR WAVEGUIDE FERROELECTRIC THIN FILM MICROWAVE PHASE SHIFTERS

4.1 Introduction

4.1.1 Microwave Phase Shifters

A microwave phase shifter is a two-port device capable of producing a true delay of a microwave signal flowing through it. The produced time delay can be a constant or a variable for a device. And the phase shifter is accordingly called fixed phase shifter or tunable phase shifter. Electronically tunable phase shifters are key elements in phased array antennas and microwave communication systems for improving wireless communications, surveillance, sensing and tracking. Current wireless and information technology require continual upgrade on the phase shifters which have compact size, low fabrication cost, as well as large phase shifts, low insertion loss with broadband operating frequencies, and the ability to handle wide ranges of power levels depending on their applications. Especially, demand of phase shifters which operate above 2 GHz up to 12 GHz is high for wireless communication systems.

Phase shifters can be analog or digital. Analog phase shifters provide a continuously variable phase, perhaps controlled by a voltage. Electronic phase shifters have been fabricated using various materials of ferrite [1-3],

semiconductor [4, 5], and ferroelectric [6-11]. Phase shifters using ferrite materials have demonstrated large phase shifts, low insertion loss, and high power. However, ferrite phase shifters are slow to respond to control signals and cannot be used in applications where rapid beam scanning is required. Also, ferrite devices are difficult to integrate into current semiconductor circuits. The semiconductor devices and their circuitry are generally faster switching and inherently reciprocal, a useful antenna property. Semiconductor phase shifters are smaller than ferrites but their application is limited because of the high insertion loss at high frequencies and poor power-handling capability.

Compared with semiconductor and ferrite phase shifters, the ferroelectric phase shifters are characterized by high speed, high reliability, high radiation resistance, completely integrated technology, and a high level of permissible microwave power. The high tunability of BST, desirable to achieve a large phase shift with a physically relatively small device coupled with relatively low loss at microwave frequencies, fuels the further development of this promising ferroelectric material. Phase shifters using BST thin films have been developed by several groups. Some groups have investigated a transmission-type phase shifter making use of ferroelectric material, which forms either an entire or a fraction of a substrate so that the phase velocity can be controlled by changing capacitance [8, 12-15]. Also, a reflection-type phase shifter, which is composed of a Lange coupler and BST varactors, has been reported [16, 17]. Among them, a coplanar waveguide (CPW) transmission line phase shifter based on ferroelectric varactors has advantages over other type phase shifters because of both simple structure and low production cost

due to its simple device fabrication process. In recent years, a lot of interests were focused on distributed analog phase shifter circuits [18-20], where the wave propagates through periodic structures comprising of lumped capacitive elements. And this structure was first demonstrated using BST thin film varactors by York's group [14]. Although these capacitances can in fact be with either parallel-plate or planar-type capacitors, in comparison with the coplanar design [21-23], the devices with parallel-plate electrodes [7, 24] offer lower control voltage and higher tunability.

However, because of the high dielectric permittivity and the small thickness, the parallel-plate varactors have large capacitance which limits their high frequency applications; also in some ferroelectric CPW phase shifters, parallel plate varactors involved an elaborate process and required bottom electrode patterning. Patterning bottom electrode typically limits the minimum bottom electrode dimension and requires stringent lithography facility. Moreover, most of the distributed circuit designs need very small capacitance in order to attempt an impedance match. In the next sections, a distributed phase shifter circuit with two series connection parallel plate varactors, which can increase the dimension of varactor and simultaneously maintain the small capacitance, will be presented.

4.1.2 Coplanar Waveguide Transmission Lines

A coplanar waveguide (CPW) fabricated on a dielectric substrate was first demonstrated by C. P. Wen in 1969 [25]. A configuration of CPW transmission line on multilayer substrates (ferroelectric film layer and the

wafer) is shown in Figure 2.4. As the strip conductor is deposited on the same surface as the two ground planes in close proximity, the CPW transmission line has demonstrated several advantageous features over the conventional microstrip line, for instance, easy surface mounting of external devices, easy fabrication of both shunt and series passive elements, low-frequency dispersion, and easy adjustment of desirable characteristic impedance. Since its proposal, the CPW technology has been progressively gaining a tremendous application in exploration of advanced RF and microwave integrated circuits, modules, and subsystems. The dimensions of the center strip, the gap, the thickness and permittivity of the dielectric substrate determined the effective dielectric constant (ε_{eff}), characteristic impedance (Z_0), and the attenuation (α) of the transmission line. So far, extensive work in theory has been done to characterize a variety of CPW transmission lines in terms of per unit length characteristic impedance and propagation constants by developing the quasi-static and full-wave analysis approaches [26, 27].

The CPW transmission line has basically two dominant modes of propagation: quasi-TEM (called the even mode or coplanar waveguide mode) and non-TEM mode (called the odd mode or slotline mode). In CPW microwave circuits, the quasi-TEM mode is the most desired due to its low radiation properties. In this way, the excitation of the unwanted slotline mode can be avoided by either maintaining the symmetry of the structure or using air-bridges as bond wires to connect the ground planes of the CPW. Also, the cross-sectional dimensions, such as slot and strip widths, are readily selected electrically short in the frequency region of operation, so as to minimize the longitudinal magnetic field component.

4.2 Theory of Distributed Transmission Line Phase Shifters

The equivalent circuit of distributed ferroelectric phase shifter is shown in Figure 4.1. The phase can be controlled by tuning of the transmission line. According to ref. 18, one can define a unit cell for this periodic structure, which consists of a section of transmission line of length (L_{sect}) and a shunt varactor (C_{var}) to ground. The transmission line section can be approximated as a lumped inductance (L_t) and capacitance (C_t). The shunt varactor is added periodically as discrete elements to the transmission line. This varactor loading makes the distributed phase shifter a periodic structure. A result of creating a periodic structure is the existence of a cutoff frequency or Bragg frequency near the point where the guided wavelength approaches the periodic spacing of the discrete components. The Bragg frequency is given by [28]:

$$f_{Bragg} = \frac{1}{\pi\sqrt{L_t(C_t+C_{var})}} \tag{4.1}$$

$$L_t = \frac{L_{sect}}{v_i} Z_i \,, \quad C_t = \frac{L_{sect}}{Z_i v_i} \tag{4.2}$$

where L_t and C_t are the inductance and capacitance per unit cell and Z_i and v_i are the impedance and velocity on the high impedance line, respectively.

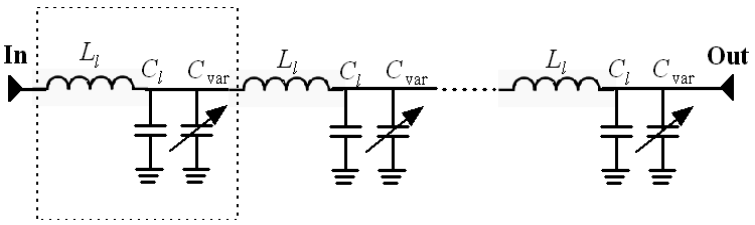

Figure 4.1 Equivalent circuit of distributed ferroelectric phase shifter.

When frequencies are well below the Bragg frequency, the distributed transmission line phase shifter may be treated as a synthetic transmission line. The capacitance per unit length for the synthetic transmission line has been increased due to the periodic loading. The inductance per unit length of the synthetic transmission line is unchanged from that of the original unloaded line. Since the loading varactors are voltage dependent, the properties of this synthetic transmission line, such as its characteristic impedance and phase velocity, are voltage dependent. Therefore, it is possible to control the phase shift for a given length of transmission line by changing the bias voltage. The phase velocity, the characteristic impedance (Z_l), and the insertion phase (φ) of this transmission line are given by

$$v_{phase} = 1/\sqrt{L_l(C_l + C_{var}/L_{sect})} \tag{4.3}$$

$$Z_L = \sqrt{L_l/(C_l + C_{var}/L_{sect})} \tag{4.4}$$

$$\varphi = 2n\pi f L_{sect}\sqrt{L_l(C_l + C_{var}/L_{sect})} \tag{4.5}$$

where $L_l = Z_i/v_i$ and $C_l = 1/(Z_i v_i)$ are the inductance and capacitance per unit length of the CPW transmission line, C_{var} is the capacitance of the loaded varactor, L_{sect} is length of a periodical cell, and n is number of sections. The phase shift of each section of the distributed phase shifter varies as capacitance of varactor is tuned by dc bias. At any given frequency *f*, the maximum differential phase shift of each section is given by

$$\Delta\varphi = 2n\pi f L_{sect}\sqrt{L_l}\left(\sqrt{C_l + C_{var}^{max}/L_{sect}} - \sqrt{C_l + C_{var}^{min}/L_{sect}}\right) \tag{4.6}$$

The terms $C_{\text{var}}^{\max}$ and $C_{\text{var}}^{\min}$ denote the extremes of the values C_{var} can assume with tuning. The equation (4.6) indicates that changing the capacitance ratio ($C_{\text{var}}^{\max}/C_{\text{var}}^{\min}$) results in more differential phase shift.

4.3 Design and Implementation of Coplanar Waveguide Ferroelectric Microwave Phase Shifters

The layout of distributed transmission line phase shifter of coplanar waveguide using ferroelectric thin film varactors with parallel plate electrodes based on 6 unit cells is shown in Figure 4.2 (a). Coplanar line is deposited on top of ferroelectric film. The shunt varactors are added periodically as discrete elements to the transmission line. Tuning the periodic loading reactance alters the phase velocity of the transmission line, resulting in a phase shift.

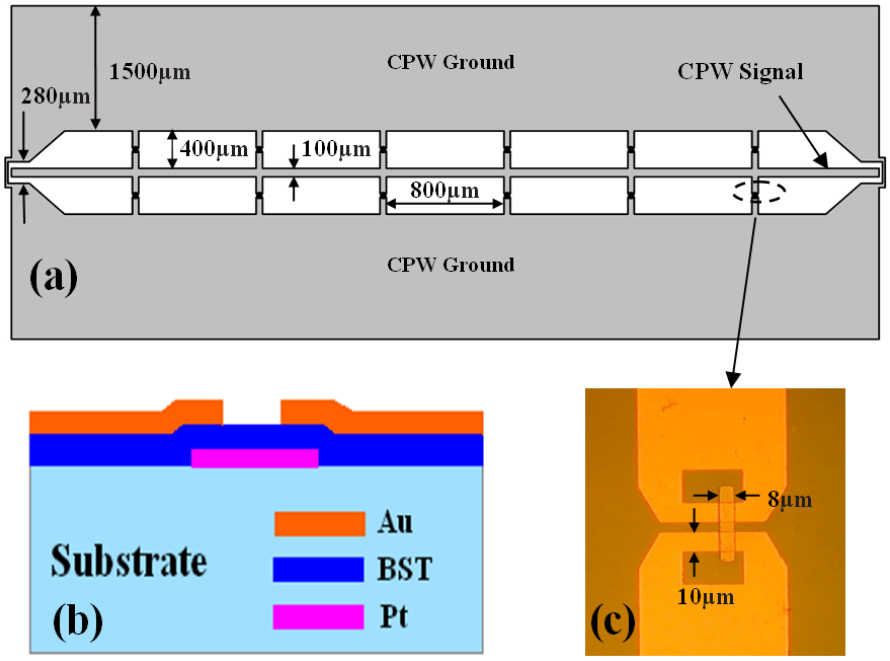

Figure 4.2 (a) Layout of the distributed transmission line phase shifter of coplanar waveguide. (b) The side view of a parallel plate varactor. (c) The photograph of top view of one varactor.

Table 4.1 The primary parameters used to simulate phase shifter.

Parameter	Value
The dimension of Si substrate	$5 \times 10 \times 0.5$ mm^3
The number of unit cells	6
The dielectric constant of substrate	12
The width of center conductor	100 μm
The spacing between two varactors	800 μm
The gap dimension of transmission line	400 μm

For the optimization of the distributed transmission line, such as for better impedance match, the structure of phase shifter was designed by a high-performance full-wave electromagnetic field simulator (HFSS). The primary parameters used to simulate phase shifter were adopted shown in Table 4.1. The capacitance of shunt varactor used in simulation was varied from 0.07 pF to 0.4 pF. For different capacitance of shunt varactor used in simulation, different characteristic impedance of the phase shifter circuit was obtained by HFSS. Figure 4.3 shows the matching impedance of phase shifter circuit as a function of capacitance of the shunt varactor. The capacitance of the shunt varactors used in the phase shifter circuit was 0.24 pF for obtaining characteristic impedance closed to 50 ohm. For the capacitance of shunt varactor of 0.24 pF, the scattering matrixes of the simulation of distributed phase shifter were shown in Figure 4.4 under different full port impedance. When the full port impedance is 50 ohm, the return loss is smallest, which indicates that the characteristic impedance of the phase shifter circuit with the capacitance of shunt varactor of 0.24 pF is closer to 50 ohm.

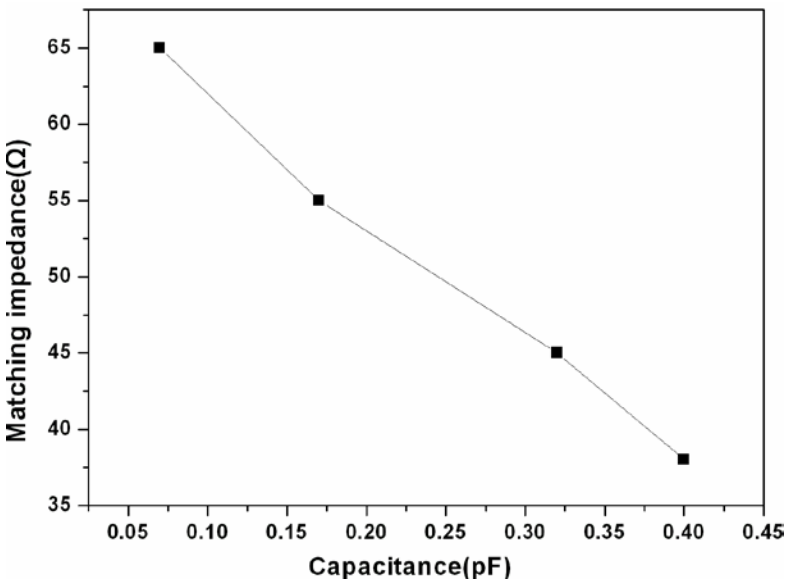

Figure 4.3 The matching impedance of phase shifter circuit as a function of capacitance of shunt varactor.

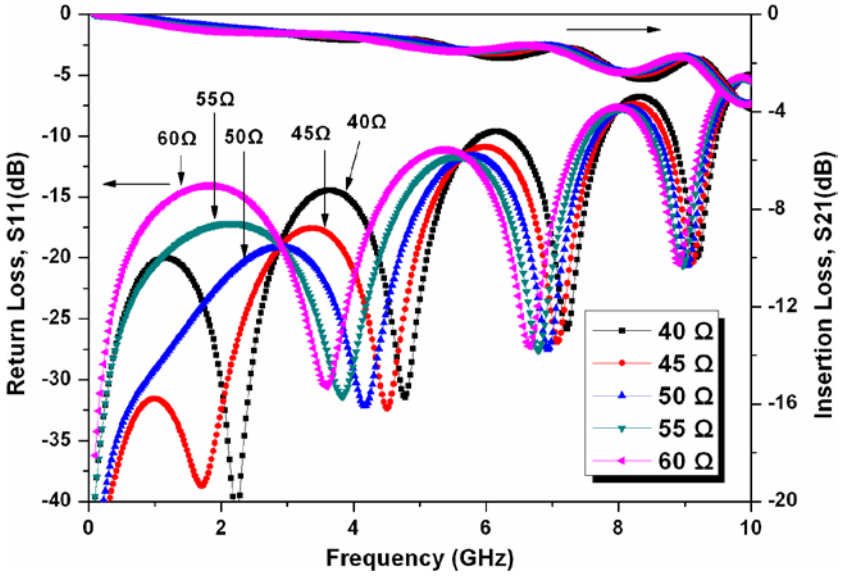

Figure 4.4 The simulation results of the phase shifter under different full port impedance.

Because of two series connection parallel plate varactors used in the circuit, the capacitance of ferroelectric thin film parallel-plate varactor designed to be about 0.48 pF. $Ba_{0.25}Sr_{0.75}TiO_3$ (BST) thin film of thickness ~300 nm was grown using PLD method on pre-patterned high-resistivity silicon substrate (5mm×10mm) that had ion beam etched Pt metal as the bottom electrode of parallel-plate varactor. In order to decrease the dielectric loss at high frequency, a layer of 2-μm-thick Au was electroplated on the prepared seed layers of Au/Cr by RF magnetron sputtering. The schematic side view of a parallel-plate varactor is shown in Figure 4.2 (b) and the photograph of top view of one varactor is also shown in Figure 4.2 (c). For the highest operating frequency of the phase shifter being well below cutoff frequency and also impedance match of the circuit, the dimensions of the conductor layer were selected appropriately. Because larger capacitance of the varactors is favorable for both the purpose of high tunability and easy fabrication, the impedance of unloaded CPW should be kept as high as possible to achieve impedance match while varactors are loaded. Based on the simulation results, the CPW transmission line with gap dimension of 400 μm and center conductor width of 100μm periodically loaded with ferroelectric thin film parallel-plate varactors (8μm × 10μm) with spacing $L_{sect} = 800\,\mu m$. The phase shifter characteristics are controlled mainly by the properties of the varactor according to the equation (4.6).

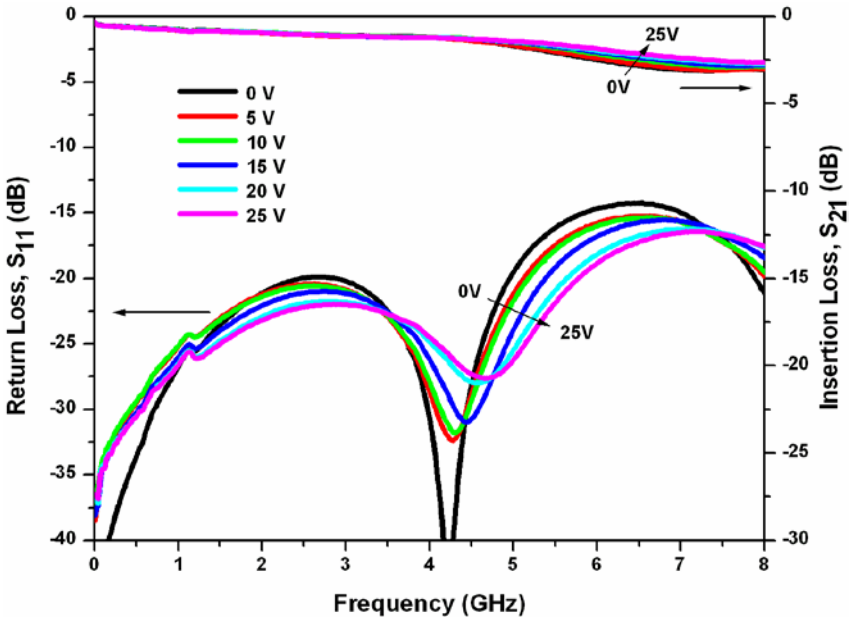

Figure 4.5 Frequency dependent insertion loss and return loss of the distributed ferroelectric phase shifter based on 6 unit cells at different bias voltages.

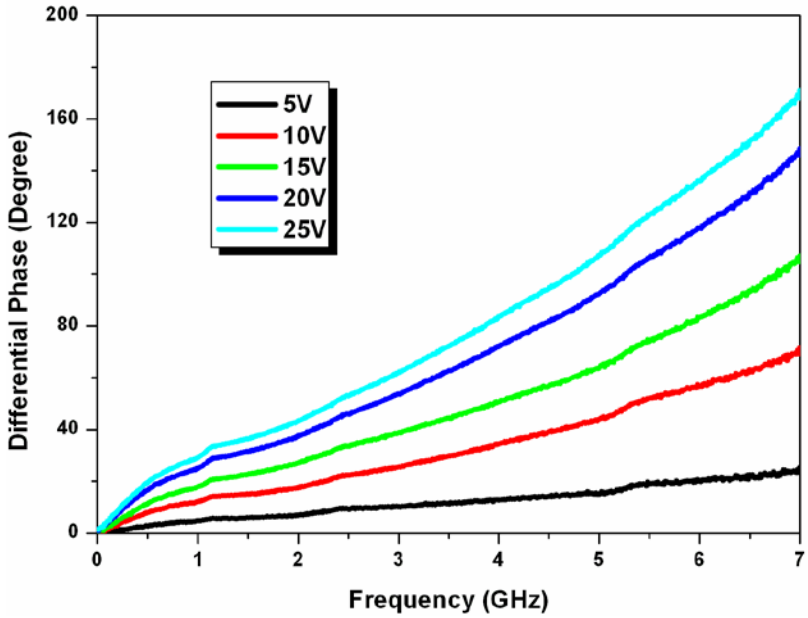

Figure 4.6 Differential phase shift of the phase shifter as a function of frequency at different bias voltages.

4.4 Experimental Results and Discussion

The scattering matrix of the CPW phase shifter shown in Figure 4.5 was measured by PNA Series Network Analyzer (Agilent N5230A) with external bias tees. Off wafer short-open-load-thru (SLOT) calibration was performed setting the reference planes at the probe tips. All measurements were taken from 10 MHz to 8 GHz at steps of 10 MHz. Pasternack PE1611 bias tee and Keithley 237 voltage source were used to supply dc bias voltage through signal probe and the copper pad. A periodic resonance could be observed in the frequency dependent return loss and is due to the coupling of the inductance from the center signal transmission line and capacitance of ferroelectric thin film varactor. When the dc bias is applied, the dielectric constant of the ferroelectric film is decreased due to the soft mode hardening, and therefore the resonance moves to a higher frequency. The insertion loss is decreased as the applied dc bias is increased because the dielectric loss in the ferroelectric thin film is reduced. The return loss was better than 16 dB over all phase states. The maximum insertion loss was 3.05 dB at 6.5 GHz with no dc bias. The differential phase shift with respect to the zero bias is plotted for 5 different bias voltages in Figure 4.6. The circuit of phase shifter was capable of a continuous 0-170^o phase shift with an insertion loss of only 2.3 dB at 7 GHz. The figure of merit F of the phase shifter, defined as the maximum differential phase shift divided by the insertion loss averaged across the full voltage range, is rather high, $F \approx 78\ °/dB$. These values are significant since large differential phase shift are achieved with such a low bias voltage of 25 V. A high performance microwave phase shifter with a 360^o phase shift at a low

bias voltage can be produced with more unit cells. The insertion loss for these circuits would be decreased by using thicker bottom electrodes.

4.5 Conclusion

In this chapter, the physical layout design, device fabrication, and microwave characterization of distributed CPW transmission line phase shifter using ferroelectric thin film varactors with parallel-plate electrodes are presented. The equivalent circuit model was simulated by the EM simulation software in an effort to optimize the design. The fabricated phase shifter exhibited differential phase shift of 170^{o} at 7 GHz with a low bias voltage of 25 V. The maximum insertion loss was 3.05 dB at 6.5 GHz with no dc bias and the return loss was better than 16 dB over all phase states. These results provide a simple method for obtaining excellent microwave properties of CPW phase shifter using ferroelectric thin film varactors. The high performance microwave phase shifters using ferroelectric films with a 360^{o} phase shift are the most critical component of modern electronically phased array antenna systems for mobile communications services.

References:

1. H. How, H. Hu, C. Vittoria, L. C. Kempel, and K. D. Trot, "Single crystal yttrium iron garnet phase shifter at X band", *J. Appl. Phys.*, **85**, 4853 (1999).

2. I. Viswanathan, S. D. Yoon, T. Sakai, A. L. Geiler, J. W. Wang, C. N. Chinnasamy, C. Vittoria, and V. G. Harris, "High Performance Compact Microstripline Phase Shifter at C-Band Using Yttrium Iron Garnet", *IEEE Transactions on Magnetics*, **45** (10), 4176 (2009).

3. J. D. Adam, L. E. Davis, G. F. Dionne, E. F. Schloemann, and S. N. Stitlzer, "Ferrite devices and materials", *IEEE Trans. Microwave Theory Tech.*, **50**(3), 721 (2002).

4. C. Tsironis and P. Harrop, "Dual gate GaAs MESFET phase shifter with gain at 12 GHz", *Electron. Lett.*, **16**, 553(1980).

5. M. Kumar, R. J. Menna, and H. Huang, "Broadband active phase shifter using dual-gate MESFET", *IEEE Trans. Microw. Theory Tech.*, **MTT-29**, 1098 (1981).

6. S. Sheng, Peng Wang, Xin Chen, Xiao-Yu Zhang, and C. K. Ong, "Two paralleled $Ba_{0.25}Sr_{0.75}TiO_3$ ferroelectric varactors series connected coplanar waveguide microwave phase shifter", *J. Appl. Phys.*, **105**, 114509 (2009).

7. L. Y. Chen, R. Forse, A. H. Cardona, T.C. Watson, and R. A. York, "Compact Analog Phase Shifters using Thin-Film $(Ba,Sr)TiO_3$ Varactors", *IEEE/MTT-S International Microwave Symposium*, v1-6, pp.666, Honolulu, HI, (2007).

8. P. Wang, C. Y. Tan, Y. G. Ma, W. N. Cheng, C. K. Ong, "Planar tunable high-temperature superconductor microwave broadband phase shifter with patterned ferroelectric thin film", *Supercond. Sci. Technol.*, **20**, 77 (2007).

9. D. Kim, Y. Choi, M. Ahn, M.G. Allen, J.S. Kenney, and P. Marry, "*2.4 GHz Continuously Variable Ferroelectric Phase Shifters Using All-Pass Networks*", IEEE Microwave Wireless Comp. Lett., **13**, 434 (2003).

10. P. M. Suherman, T. J. Jackson, Y. Y. Tse, I. P. Jones, R. I. Chakalova, M. J. Lancaster, and A. Porch, "Microwave properties of $Ba_{0.5}Sr_{0.5}TiO_3$ thin film coplanar phase shifters", *J. Appl. Phys.*, **99**, 104101 (2006).

11. G. Vélu, K. Blary, L. Burgnies, J. C. Carru, E. Delos, A. Marteau, D. Lippens, "A 310°/3.6-dB K-band phase shifter using paraelectric BST thin films", *IEEE Microwave Wireless Comp Lett.*, **16**, 87 (2006).

12. F. D. Flaviis, N. G. Alexopoulos and O. M. Stafsudd, “Planar microwave integrated phase shifter design with high purity ferroelectric material”, *IEEE Trans. on Microwave Theory and Tech.*, **45**(6), 963 (1997).

13. A. Kozyrev, V. Osadchy, A. Pavlov, and L. Sengupta, “Application of Ferroelectrics in Phase Shifter Design”, *IEEE MTT-S Int. Microwave Symp. Dig.*, **3**, 1355 (2000).

14. Y. Liu, A. S. Nagra, E. G. Erker, P. Periaswamy, T. R. Taylor, J. Speck, and R. A. York, “$BaSrTiO_3$ Interdigitated Capacitors for Distributed Phase Shifter Applications,” *IEEE Microwave and Guided Wave Lett.*, **10**(11), 448 (2000).

15. S. J. Lee, S. E. Moon, M. H. Kwak, H. C. Ryu, Y. T. Kim, and K. Y. Kang, “High Dielectric Tunability of $(Ba,Sr)TiO_3$ Thin Films and Their Coplanar Waveguide Phase Shifter Application,” *Jpn. J Appl. Phys.*, **43**, 6750 (2004).

16. D. S. Kim, Y. S. Choi, M. G. Allen, J. S. Kenny, and D. Kiesling, “A Wide Bandwith Monolithic BST Reflection-Type Phase Shifter Using a Coplanar Waveguide Lange Coupler,” *IEEE MTT-S International Microwave Symposium Digest*, **3**, 1471 (2002).

17. O. G. Vendik, M. A. Nilol’ski, and S. P. Zubho, “Optimization of Reflection Type Ferroelectric Phase Shifter with Respect to Sensitivity to Statistical Dispersion of Circuit Characteristics at Microwaves,” *Integ. Ferroelectrics*, **49**, 141 (2002).

18. A. S. Nagra and R. A. York, “Distributed analog phase shifters with low insertion loss”, *IEEE Trans. Microwave Theory Tech.*, 47, 1705 (1999).

19. V. O. Sherman, T. Yamada, A. Noeth, N. Setter, M. Mandeljc, B. Malic, M. Kosec, and M. Vukadinovic, “Microwave Phase Shifters Based on Sol-Gel Derived $Ba_{0.3}Sr_{0.7}TiO_3$ Ferroelectric Thin Films”, *37th European Microwave Conference*, Munich, p1295 (2007).

20. T. Ji, H. Yoon, J.K. Abraham, and V.K. Varadan, “Ku-band antenna array feed distribution network with ferroelectric phase shifters on silicon”, *IEEE Trans. Microwave Theory Tech.*, **54**, 1131 (2006).

21. P. M. Suherman, T. J. Jackson, Y. Y. Tse, I. P. Jones, R. I. Chakalova, M. J. Lancaster, and A. Porch, “Microwave properties of $Ba_{0.5}Sr_{0.5}TiO_3$ thin film coplanar phase shifters”, *J. Appl. Phys.*, **99**,104101 (2006).

22. A. Yu, C. Yang, H. Chen and J. Zhang, “Distributed ferroelectric phase shifter with slots periodically inserted into ground”, *Electronics Letters*, **44**(3), 207 (2008).

23. I. Paul, K. J. Vinoy, “Design optimization of micromachined ferroelectric based phase shifter using modified ground coplanar waveguide”, *Microwave and Optical Technology Letters*, **46**(2), 185 (2005).

24. W. F. Hu, D. Zhang, M. J. Lancaster, T. W. Button, and B. Su, “Investigation of Ferroelectric Thick-Film Varactors for Microwave Phase Shifters”, *IEEE Trans. Microw. Theory Tech.*, **55**, 418 (2007).

25. C. P. Wen, “Coplanar Waveguide: A Surface Strip Transmission Line Suitable for Nonreciprocal Gyromagnetic Device Applications”, *IEEE Trans. Microwave Theory Tech*., **17**, 1087 (1969).

26. R. N. Simons, “Coplanar Waveguide Circuits, Components, and Systems”, *Wiley*, New York (2001).

27. I. Wolff, “Coplanar Microwave Integrated Circuits”, *Wiley-Interscience*, New Jersey (2006).

28. M. J. W. Rodwell, S. T. Allen, R. Y. Yu, M. G. Case, U. Bhattacharya, M. Reddy, E. Carman, M. Kamegawa, Y. Konishi, J. Pusl, R. Pullela, and J. Esch, “Active and nonlinear wave propagation devices in ultrafast electronics and optoelectronics”, *Proc. IEEE*, **82**, 1035 (1994).

Chapter 5

COUPLED MICROSTRIP LINE FERROELECTRIC THIN FILM MICROWAVE PHASE SHIFTERS

Another type of phase shifter uses coupled microstrip line as dc electrodes to polarize a ferroelectric thin film. The coupled microstrip lines are often used in microwave integrated circuits, where couplers or filters have been realized within the circuitry. This chapter describes the coupled microstrip line phase shifter (CMPS) using BST thin film varactors with parallel plate electrode.

5.1 Properties of Coupled Microstrip Line

Ferroelectric thin film coupled microstrip line phase shifters are preferable for balanced circuits and will improve the flexibility of circuit design and integration, especially for scanning reflectarray antenna applications [1-5]. Some basic design equations for coupled microstrip lines useful for design of phase shifters are briefly described in this section.

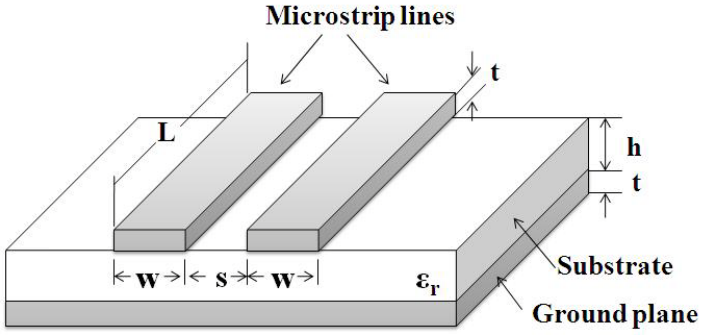

Figure 5.1 A configuration of conventional coupled microstrip lines.

A configuration of conventional coupled microstrip lines is provided in Figure 5.1. This structure is composed by setting two microstrip lines of width *w* at a distance *s*. The two lines can carry two fundamental quasi-TEM modes, the even and the odd mode, which have different effective dielectric constants (i.e., different phase velocities of their waves) and different dispersion properties because of the different field structures of the modes. The electric (E) and magnetic (H) fields associated with each mode are indicated in Figure 5.2. For an even-mode excitation, both microstrip lines have the voltage potentials or carry the same sign charges, say the positive ones, resulting in a magnetic wall at symmetry plane, as shown in Figure 5.2 (a). For the odd-mode, both microstrip lines have the opposite voltage potentials or carry the opposite sign charges, so that the symmetric plane is an electric wall, as indicated in Figure 5.2 (b). In general, these two modes will be excited at the same time. However, they propagate with different phase velocities because they are not pure TEM modes, which mean that they experience different permittivities. Therefore, the coupled microstrip lines are characterized by the characteristic impedances and the effective dielectric constants of the even- and odd- modes [6].

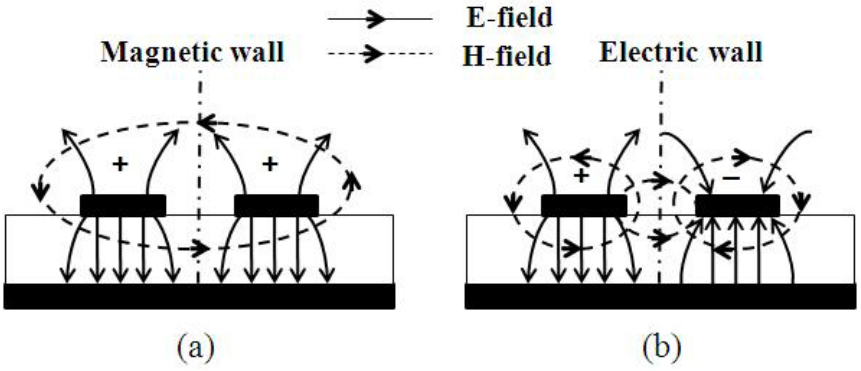

Figure 5.2 Field distributions resulting from (a) even-mode and (b) odd-mode excitation of the coupled microstrip lines.

The most simple and widely used expressions for symmetric coupled microstrip line synthesis are provided by Garg and Bahl [7]. These equations are extracted using a quasi-static analysis of the coupled microstrip line structure, which permits obtaining the coupled lines' capacitances. The even- and odd- mode characteristic impedances Z_{even} and Z_{odd} can be obtained from the capacitances.

$$Z_{even} = (c\sqrt{C_{even}^{air} \cdot C_{even}})^{-1} \tag{5.1}$$

$$Z_{odd} = (c\sqrt{C_{odd}^{air} \cdot C_{odd}})^{-1} \tag{5.2}$$

where C_{even} and C_{odd} are the even- and odd-mode capacitances, C_{even}^{air} and C_{odd}^{air} are even- and odd-mode capacitances for the coupled microstrip line configuration with air as dielectric.

Effective dielectric constant ε_{even} and ε_{odd} for even and odd modes, respectively, can be obtained from above equations.

$$\varepsilon_{even} = C_{even}/C_{even}^{air} \tag{5.3}$$

$$\varepsilon_{odd} = C_{odd}/C_{odd}^{air} \tag{5.4}$$

5.2 Design and Simulation of Coupled Microstrip Line Phase Shifter Circuit

The coupled microstrip line phase shifter is basically a high impedance transmission line periodically loaded with ferroelectric thin film varactors. The equivalent lumped element circuit of the phase shifter is similar with that of the coplanar waveguide phase shifter, as shown in Figure 4.1. And the maximum differential phase shift of each section at different states is given as

equation (4.6). The first step in designing the phase shifter is to determine the dimensions of each part of the coupled microstrip line to achieve the highest tunability while maintaining the impedance match. For a small change of dc bias *U*, the tunability $\Delta\varphi/\Delta U$ can be obtained as [8]:

$$\frac{\Delta\varphi}{\Delta U} \approx \frac{n\pi f C_{\text{var}}^{0}\sqrt{L_l}}{\sqrt{C_l + (C_{\text{var}}^{0}/L_{\text{sec}t})}} \cdot \frac{\Delta(C_{\text{var}}/C_{\text{var}}^{0})}{\Delta U} \tag{5.5}$$

where $L_l = Z_i/v_i$ and $C_l = 1/(Z_i v_i)$ are the inductance and capacitance per unit length of the coupled microstrip transmission line, C_{var} and C_{var}^{0} are the capacitances of the loaded varactor at bias *U* and zero, respectively. $L_{\text{sec}t}$ is length of a periodical cell, and n is number of sections. The term $\Delta(C_{\text{var}}/C_{\text{var}}^{0})/\Delta U$ is the ratio of the percentage change of the varactor capacitance to the change of dc bias.

A schematic structure of a segment of the coupled microstrip line loaded with three varactors is shown in Figure 5.3. It also shows the top view of a varactor periodically loaded between the two strip lines. The layer structure of the parallel-plate varactor has been shown in chapter 4 (Figure 4.2 (b)). In our study, the designed structure of the coupled microstrip line is based on eight unit cells. The coupled microstrip line loaded with eight varactors was simulated by HFSS. In the simulation, everything was considered lossless, i.e., perfect conductor, lumped capacitance, and Si substrate were used. The calculated capacitance of loaded ferroelectric varactor at zero bias voltage is about 0.12 pF. Figure 5.4 shows the simulated response of the coupled microstrip line loaded with eight varactors of capacitance of 0.12 pF, which shows low insertion loss and good impedance matching.

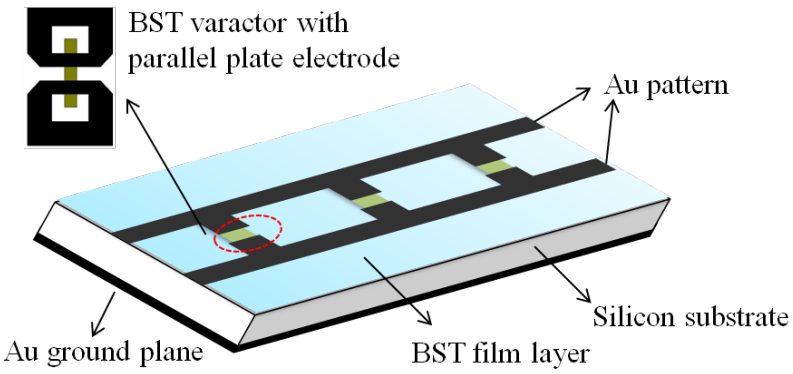

Figure 5.3 A schematic structure of a segment of the coupled microstrip line loaded with three varactors.

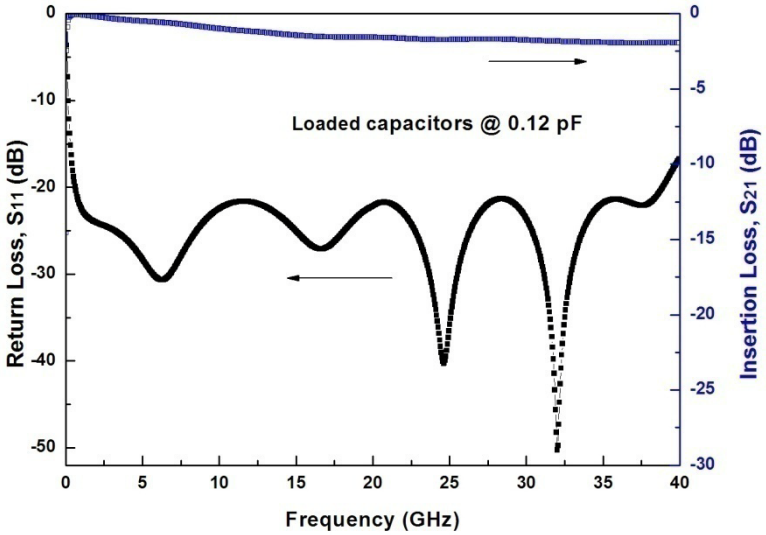

Figure 5.4 The simulated response of the coupled microstrip line loaded with eight capacitors of capacitance of 0.12 pF.

In general, minimum attenuation is obtained when the effect of the ground plane loss is minimized (i.e., in the odd or balanced mode current flows into one strip and returns through the other). Maximum attenuation occurs in the even or unbalanced mode when equal currents flow into both strips and return through ground [9]. For the phase shifter designed in this study, the phase

velocity of a signal can be more effectively tuned in the odd mode due to the fact that dc bias field is applied between the coupled lines and concentrates in the BST thin film. If the phase velocity is dominated by the even mode field, the microwave electric field is between the microstrip lines and the ground plane as shown in Figure 5.2 (a), the changing of phase velocity with applied bias voltage will be insignificant. In order to provide an odd mode excitation of the coupled microstrip lines, a microstrip Marchand balun circuit [10, 11] is adopted in the circuit design of coupled microstrip line phase shifter. A balun basically converts signal between an unbalanced and a balanced circuits. The topology of the planar Marchand balun using microstrip line to coupled microstrip lines is shown in Figure 5.5.

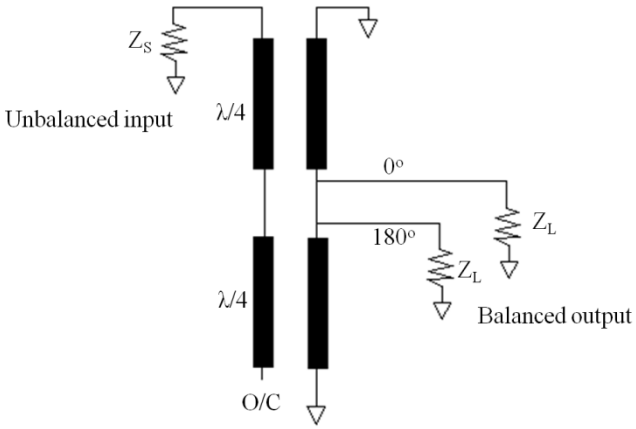

Figure 5.5 The topology of the planar balun using microstrip line to coupled microstrip lines.

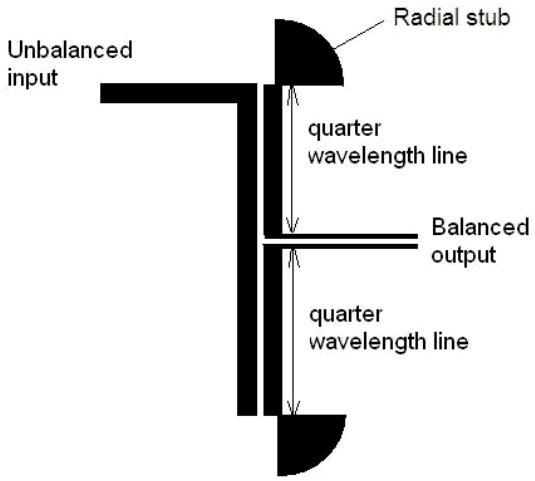

Figure 5.6 Layout of top conductor layer of the planar Marchand balun.

Figure 5.6 shows the schematic of the planar Marchand balun to be used in the phase shifter circuit. The balun consists of two pairs of parallel-coupled quarter wavelength lines connected in series. The signal referenced to ground at unbalanced input will be transformed into two signals with equal amplitude and a phase difference of 180° at balanced output. Then these differential signals at balanced port of the balun will be fed to the inputs of the coupled microstrip lines. By this means, the balun works as a transformer of odd mode excitation and a transmission stop circuit for even mode excitation. The radial stubs work as RF grounds for the baluns and electrodes for applying dc field at same time.

In the phase shifter circuit, the balun also works as an impedance matching network. The characteristic impedances of the microstrip line (Z_S), the coupled microstrip lines (Z_L), and even and odd modes of the coupled section of the balun (Z_e and Z_o) have the relationship

$$\sqrt{Z_S \cdot Z_L} = \frac{\sqrt{2}Z_e \cdot Z_o}{Z_e - Z_o} \tag{5.6}$$

where Z_S is usually 50Ω for integration with standard system. The even and odd mode characteristic impedances (Z_e and Z_o) of the coupled section can be adjusted by altering the width of strip lines and gap between two coupled lines [12]. Therefore, the port impedance on the balanced output of the balun can be chosen for the requirement of the circuit design. By this means, the balun provides tailored impedance matching between different impedances of circuits. The performances of the balun are simulated using HFSS software and Figure 5.7 shows the S-parameters results for the planar Marchand balun. It indicates that a good performance over the special frequency range from 4 to 16 GHz with the input return loss and insertion loss better than 10 dB and 2 dB, respectively. The inset shows the magnitude of the electric field in the balun. The high electric field was observed to be concentrated in the gap between coupled lines.

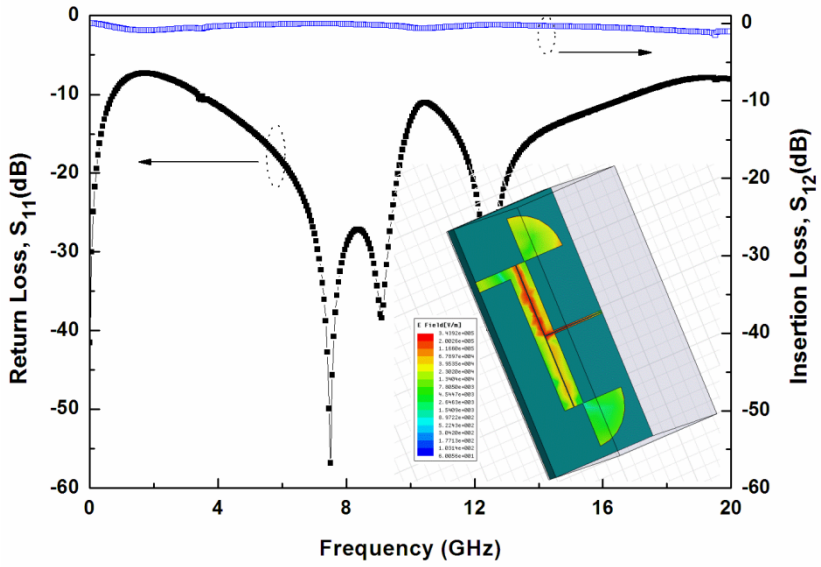

Figure 5.7 Simulated S-parameters for the planar Marchand balun. Inset shows magnitude of the electric field in the balun.

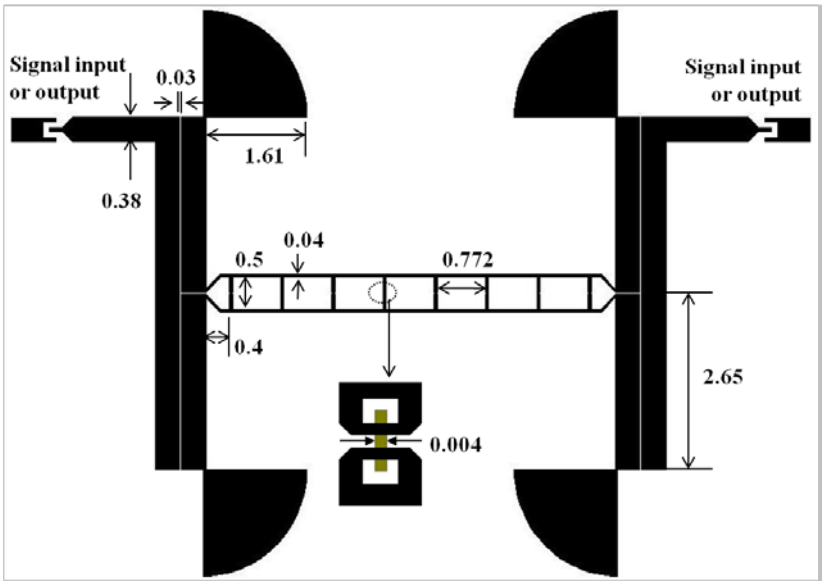

Figure 5.8 Layout of the coupled microstrip line phase shifter, with all dimensions in millimeters.

5.3 Fabrication Process and Measurement Results

For the highest tunablity with the lowest insertion loss, the parameters of the coupled microstrip line phase shifter circuit are optimized according to the simulation results. The whole layout of the coupled microstrip line phase shifter is shown in Figure 5.8. The coupled microstrip line consists of 8 unit cells. The gap between coupled lines and the width of strip lines of the balun are 30 μm and 380 μm, respectively. The coupled microstrip line with gap dimension of 500 μm and strip line conductor width of 40 μm periodically loaded with ferroelectric thin film parallel-plate varactors (4μm × 4μm) with spacing $L_{sect} = 772\,\mu m$. $Ba_{0.25}Sr_{0.75}TiO_3$ (BST) thin film of thickness ~300 nm was grown using PLD method on pre-patterned high-resistivity silicon substrate (12.3 mm × 14 mm) that had ion beam etched Pt metal as the bottom

electrode of parallel-plate varactor. A layer of 2-μm-thick Au on both sides of the phase shifter device was electroplated on the prepared seed layers of Au/Cr by RF magnetron sputtering. The BST growth procedures and metallization for the phase shifter are similar to those described in chapter 2.

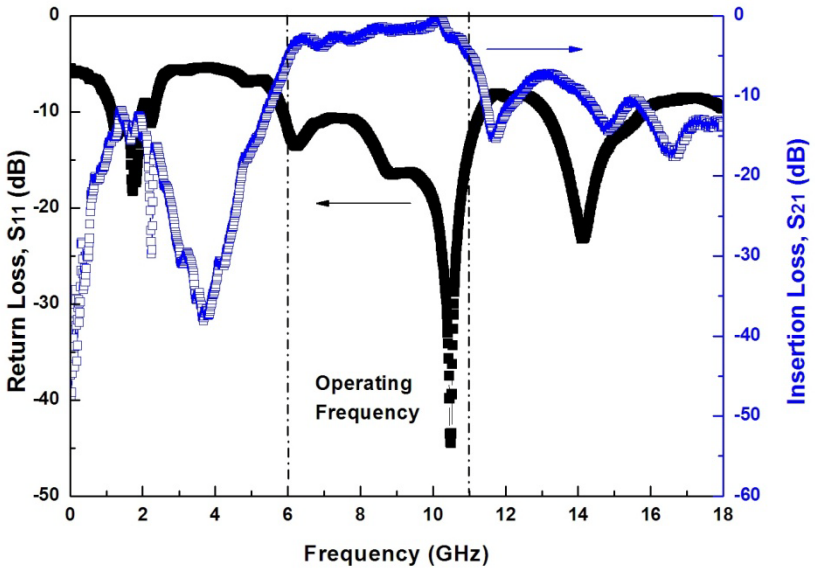

Figure 5.9 Measured frequency dependent insertion loss and return loss of the phase shifter based on 8 unit cells at zero bias voltages.

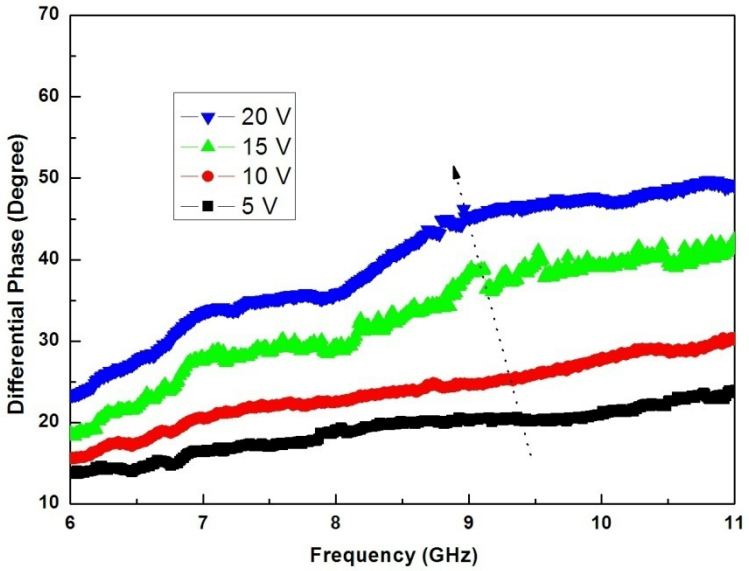

Figure 5.10 Measured differential phase shift of the phase shifter as a function of frequency at different bias voltages.

The scattering matrix of the coupled microstrip line phase shifter was measured by PNA Series Network Analyzer with a SOLT calibration as described in chapter 4. The dc electrical fields from 0 V to 20 V were applied via the radial stubs of the balun. All measurements were taken from 10 MHz to 18 GHz. Figure 5.9 shows the wide band response obtained from measured result (S_{11} and S_{21}) at zero bias voltage. The phase shifter circuit showed large insertion loss in the wide bands before 6 GHz and after 11 GHz. In the frequency range from 6 GHz to 11 GHz, the phase shifter circuit exhibited low insertion loss and good impedance matching. The measured insertion loss was less than 4 dB and return loss was better than 13 dB from 6 GHz to 11 GHz. Therefore, the operating frequency of the phase shifter device was chosen in this frequency range. Figure 5.10 shows measured differential phase shift with respect to the zero bias state as a function of frequency under different bias voltages. A differential phase shift of 45 degree was obtained with a dc bias of 20 V at frequency of 9 GHz, which corresponds to a figure of merit of ~23 deg/dB. The figure of merit can be further improved by applying higher electric field. With the low bias voltages, the performances of the proposed phase shifter using parallel plate ferroelectric varactors are better than that of the reported coupled microstrip line phase shifters [4, 5]. The decreasing of the operational bandwidth of the phase shifter should be caused by the planar Marchand balun. So, care should to be taken in the design of coupled lines of the balun to prevent forward-wave coupling from propagating in-band in the even mode configuration, which is caused by the different odd- and even-mode phase velocities. Further work should be done to optimize the design of the phase shifter structure.

5.4 Conclusion

In this chapter, an analog microwave phase shifter using BST varactors with parallel plate electrodes is presented. It consists of coupled microstrip line loaded with eight ferroelectric varactors and two planar Marchand baluns. The baluns work as the transformers of odd mode excitation and a transmission stop circuit for even mode excitation as well as the impedance matching networks. In the operational band from 6 GHz to 11 GHz, the measured insertion loss was less than 4 dB and return loss was better than 13 dB. A differential phase shift of 45 degree was obtained with a dc bias of 20 V at frequency of 9 GHz, which corresponds to a figure of merit of ~23^{o}/dB. The parallel plate approach for ferroelectric varactors has decreased the applied dc voltage compared to the coplanar approach. The phase shifter devices based on coupled microstrip line structure are less sensitive to interfacial effects and require simple processing.

References:

1. F. W. Van Keuls, R. R. Romanofsky, D. Y. Bohman, M. D. Winters, F. A. Miranda, C. H. Mueller, R. E. Treece, T. V. Rivkin, and D. Galt, "($YBa_2Cu_3O_{7-\sigma}$,Au)/$SrTiO_3$/$LaAlO_3$ thin film conductor/ferroelectric coupled microstripline phase shifter for phased array applications", *Applied Physics Letters*, **71**, 3075(1997).

2. R. Romanofsky, "Array phase shifters: Theory and technology", in Antenna Engineering Handbook, J. L. Volakis, Ed. *McGraw-Hill*, New York, (2007).

3. R. Romanofsky, "Advances in Scanning Reflectarray Antennas Based on Ferroelectric Thin-Film Phase Shifters for Deep-Space Communications", *Proceedings IEEE*, **95**, 1968 (2007).

4. H. C. Ryu, S. E. Moon, S. J. Lee, M. H. Kwak, Y. T. Kim, and K. Y. Kang, "Coupled Microstrip Line Ferroelectric Phase Shifter for Ka-Band Phased Array Antenna", *Integrated Ferroelectrics*, **66**, 243 (2004).

5. F. A. Mirandan, C. H. Mueller, F. W. Van Keuls, and R. R. Romanofsky, "$Ba_xSr_{1-x}TiO_3$ Thin Film Ferroelectric-Coupled Microstripline Phase Shifters with Reduced Device Hysteresis", *J. Am. Ceram. Soc.*, **91**(6), 1864 (2008).

6. J. S. Hong, M. J. Lancaster, "Microstrip Filters for RF/Microwave Applications", *John Wiley & Sons, Inc.*, (2001).

7. R. Garg, I. J. Bahl, "Characteristics of coupled microstriplines", *IEEE Trans. on MTT-27*, 700-705 (1979). Corrections in *IEEE Trans. on MTT-28*, 272 (1980).

8. P. Wang, C. Y. Tan, Y. G. Ma, W. N. Cheng, C. K. Ong, "Planar tunable high-temperature superconductor microwave broadband phase shifter with patterned ferroelectric thin film", *Supercond. Sci. Technol.*, **20**, 77 (2007).

9. R. Romanofsky and A. Qureshi, "A Model for Ferroelectric Phase Shifters", *IEEE Trans. Mag.*, **36**(5), 3491 (2000).

10. N. Marchand, "Transmission line conversion transformers", *Electronics*, **17**, 142-145 (1944).

11. Y. C. Leong, K. S. Ang and C. H. Lee, "A derivation of a class of 3-port baluns from symmetrical 4-port networks", *IEEE MTT-S Int. Microwave Symp. Digest*, **2**, 1165 (2002).

12. D. M. Pozar, "Microwave Engineering", 3rd Ed. *Wiley*, New York (2005).

Chapter 6

COMPOSITE RIGHT/LEFT-HANDED TRANSMISSION LINE MICROWAVE PHASE SHIFTER USING FERROELECTRIC VARACTORS

6.1 Introduction

Metamaterials, which are broadly defined as effectively homogeneous artificial structures with unusual properties, represent a new paradigm in physics and engineering. The most popular of metamaterials are the so-called left-handed metamaterials (LHMs) [1], which exhibit negative values of the main parameters determining the material response to electromagnetic waves: electrical permittivity ε, permeability μ, and as a result, the index of refraction $n = -\sqrt{\varepsilon\mu}$. LHMs based propagation media attract now much interest with the prospect to have further degrees of freedom in the design of novel microwave devices [2, 3]. LHMs were firstly implemented using copper split-ring resonators (SRRs) and thin copper wires [4, 5]. However, since resonant structures such as SRRs are lossy and narrow-banded, they are often difficult to implement for microwave applications. In the case of that, a nonresonant, low-loss and broad bandwidth transmission line (TL) approach towards LHMs was introduced by Eleftheriades [6, 7], Caloz and Itoh [8, 9], and Oliner [10], respectively. The TL is realized by periodically loading a conventional transmission line with lumped element series capacitors (C_0) and shunt

inductors (L_0), where the loading elements dominate the propagation characteristics.

The LH TLs have then been extended and generalized to the concept of composite right/left-handed (CRLH) structures where mixed contributions of both the LH and right-handed (RH) structures occur in practice [11]. The CRLH TL has been applied to various microwave applications of the guided wave type, for instance, couplers [12, 13], phase shifters [14], Filters [15], and leaky–wave antenna [16, 17]. In the chapter 4 and chapter 5, planar microwave phase shifters using ferroelectric thin film varactors have been demonstrated. These ferroelectric microwave phase shifters are delay line type phase shifters with frequency independent group delay instead of frequency independent phase shift. Phase shifters with both positive and negative slopes of phase-frequency dependence may be obtained by taking advantage of RH and LH TLs [18], respectively. The unique features of CRLH TL enable a differential phase shift with flat frequency dependence around center frequency [19].

In this chapter, a CRLH TL phase shifter using ferroelectric varactors integrated on high resistivity silicon substrate will be presented. We proposed a “cross” shape basic unit of CRLH TLs, in which each varactor has connected to the dc pad directly. Thus, the supply of the dc voltages across each varactor is the same as the power supply.

6.2 Model of Composite Right/Left-Handed Transmission Line Phase Shifters

6.2.1 Left-Handed Transmission Lines

Figure 6.1 shows equivalent circuit model of the unit cell of LH TL, loaded with series capacitors (C_L') and shunt inductance (L_L'). For simplicity, losses in the TL and loading elements are not considered here. The complex propagation constant γ, the propagation constant β, the characteristic impedance Z_c, the phase velocity v_p, and the group velocity v_g of the TL are given by

$$\gamma = j\beta = \sqrt{Z'Y'} = -j\frac{1}{\omega\sqrt{L_L'C_L'}} \rightarrow \beta = -\frac{1}{\omega\sqrt{L_L'C_L'}} < 0 \qquad (6.1)$$

$$Z_c = \sqrt{\frac{Z'}{Y'}} = +\sqrt{\frac{L_L'}{C_L'}} > 0 \qquad (6.2)$$

$$v_p = \frac{\omega}{\beta} = -\omega^2\sqrt{L_L'C_L'} < 0 \qquad v_g = \left(\frac{\partial\beta}{\partial\omega}\right)^{-1} = +\omega^2\sqrt{L_L'C_L'} > 0 \qquad (6.3)$$

The propagation constant β is negative, indication backward wave propagation, Z_c is positive, and v_p and v_g are negative and positive, respectively, that is antiparallel. These characteristics are the attributes of a LH transmission medium.

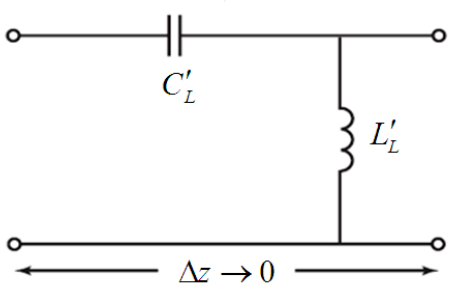

Figure 6.1 Equivalent circuit model for an infinitesimal short LH TL.

6.2.2 Composite Right/Left-Handed Transmission Lines

The concept of CRLH TL was introduced by Caloz et al. to describe practical planar LH metamaterials [11]. Figure 6.2 shows the equivalent circuit model of the unit cell and the dispersion diagram of a CRLH TL. At low frequencies, L_R and C_R tend to be short and open, respectively, so that the equivalent circuit is essentially reduced to the series C_L and shunt L_L circuit, which is LH. As the LH circuit is of high-pass nature, below a certain cut-off frequency $\omega_{cL} = 1/\left(2\sqrt{L_L C_L}\right)$, a LH stopband (LH gap) is present. At high frequencies, C_L and L_L tend to be short and open, respectively, therefore the equivalent circuit is essentially reduced to the series L_R and C_R circuit, which is RH. Due to the loss-pass nature of RH circuit, above a certain cutoff frequency $\omega_{cR} = 2/\sqrt{L_R C_R}$, a RH stopband (RH gap) is present.

If the resonance ω_{se} in the series branch and resonance ω_{sh} in the shunt branch are different (unbalanced), a gap exists between the LH and RH ranges.

$$\omega_{se} = \frac{1}{\sqrt{L_R C_L}} \tag{6.4}$$

$$\omega_{sh} = \frac{1}{\sqrt{L_L C_R}} \tag{6.5}$$

If ω_{se} and ω_{sh} are the same, i.e. $L_R C_L = L_L C_R$, the CRLH TL is said to be balanced and the gap disappears. The transition between RH and LH regions occurs at

$$\omega_0 = \sqrt{\omega_{se}\omega_{sh}} \tag{6.6}$$

For $\omega < \omega_0$, the CRLH TL is LH nature while for $\omega > \omega_0$ it is of RH nature, as illustrated in the dispersion diagram of Figure 6.2 (b). In the vicinity of ω_0, the CRLH TL acts as an effective medium.

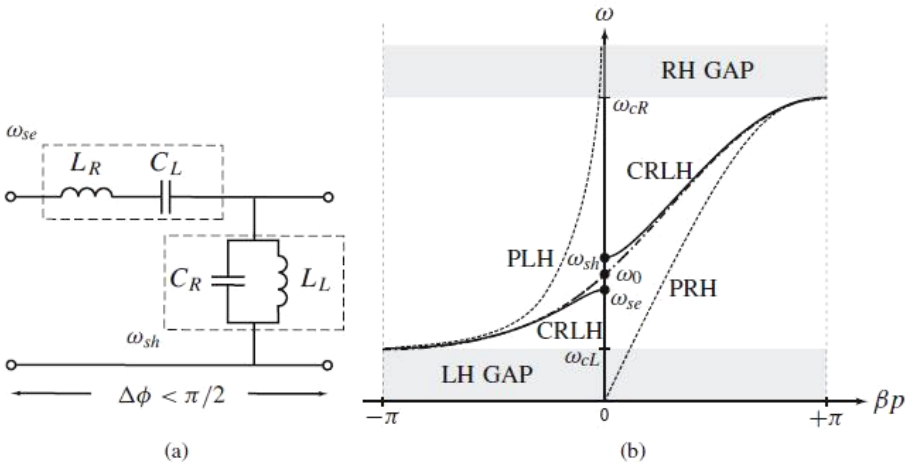

Figure 6.2 Equivalent circuit model of the CRLH unit cell (a) and Dispersion diagram of a CRLH TL [2].

In the balanced case, the propagation constant β and line impedance Z_c of the CRLH TL is given by

$$\beta = \beta_R + \beta_L = \omega\sqrt{L_R C_R} - 1/\left(\omega\sqrt{L_L C_L}\right) \tag{6.7}$$

$$Z_c = Z_R = Z_L = \sqrt{\frac{L_R}{C_R}} = \sqrt{\frac{L_L}{C_L}} \tag{6.8}$$

where the LH and RH contributions clearly decouple in the expression of β and Z_c is seen to be frequency independent, meaning that broadband matching possible.

6.2.3 Phase Shift of Varactor-Tuned CRLH TLs

For CRLH TL periodically loaded with varactors, the tunability of the varactor is defined as

$$n(V) = \frac{C(0)}{C(V)} \tag{6.9}$$

Then, the differential phase shift and characteristic impedance of CRLH TL under bias may be expressed as [19],

$$\Delta\varphi(V) = \beta(0) - \beta(V)$$
$$= \frac{2\omega}{\omega_{cR}(0)}\left(1 - \frac{1}{\sqrt{n(V)}}\right) - \frac{2\omega_{cL}(0)}{\omega}\left(1 - \sqrt{n(V)}\right) \quad (6.10)$$

$$Z_c(V) = \sqrt{n(V)}Z_c(0) \quad (6.11)$$

Under applied bias, the characteristic impedance $Z_c(V)$ is changed. To obtain an acceptable network matching, the characteristic impedance under zero bias state is chosen to be

$$\sqrt{Z_c(V)\cdot Z_c(0)} = Z_S \;\rightarrow\; Z_c(0) = \frac{Z_S}{\sqrt[4]{n(V_{max})}} \quad (6.12)$$

where Z_S is the system impedance (usually 50 Ω), and V_{max} is the maximum applied bias.

By differentiation of equation (6.10) and setting the derivative equal to zero [20], the frequency ω obtained by

$$\omega = \sqrt{\sqrt{n(V)}\omega_{cR}(0)\omega_{cL}(0)} = \sqrt[4]{n(V)}\omega_0(0) \quad (6.13)$$

If the unbiased transition frequency $\omega_0(0)$ of equation (6.6) is chosen to be

$$\omega_0(0) = \frac{\omega_C}{\sqrt[4]{n(V_{max})}} \quad (6.14)$$

The frequency ω of equation (6.13) equals the center frequency ω_C of the CRLH TL phase shifter, where the flat phase shift is obtained.

6.3 Realization of CRLH TL Phase Shifter Using Ferroelectric Varactors

6.3.1 Design and Fabrication

The CRLH TLs phase shifter presented in this chapter was designed in a high resistance silicon substrate including metal electrodes and ferroelectric $Ba_{0.25}Sr_{0.75}TiO_3$ (BST) film. The phase shifter structure consists of 3 unit cells and Figure 6.3 (a) shows the equivalent circuit. Parallel plate ferroelectric varactors were formed where the top electrode Au and bottom electrode Pt overlap each other. The fabrication process of CRLH TLs started from the commercial Pt(200 nm)/TiO_2(10 nm)/SiO_2/Si substrate and was described as following. (1) The Pt layer was patterned using ion beam etching to form the required bottom electrodes. (2) Ferroelectric BST thin film was grown on pre-patterned Pt electrode by PLD technique. The deposition conditions were described in the previous chapters. The thickness of BST film was about 410 nm determined by cross sectional SEM image. (3) A layer of 10 nm chromium (Cr) and 20 nm Au as seed layers were deposited on BST film by rf magnetron sputtering, respectively. (4) Approximate 1.5 μm thickness of Au was electroplated on the sputtered Au seed layer in order to obtain thicker top electrode and reduce the metal loss at microwave frequency. (5) The Au top electrode was formed by lift off process using photolithography and chemical etching. The photograph of the CRLH TL phase shifter with the dimension of 3330 μm × 2250 μm, including three "cross" -unit cells, was shown in Figure 6.3 (b).

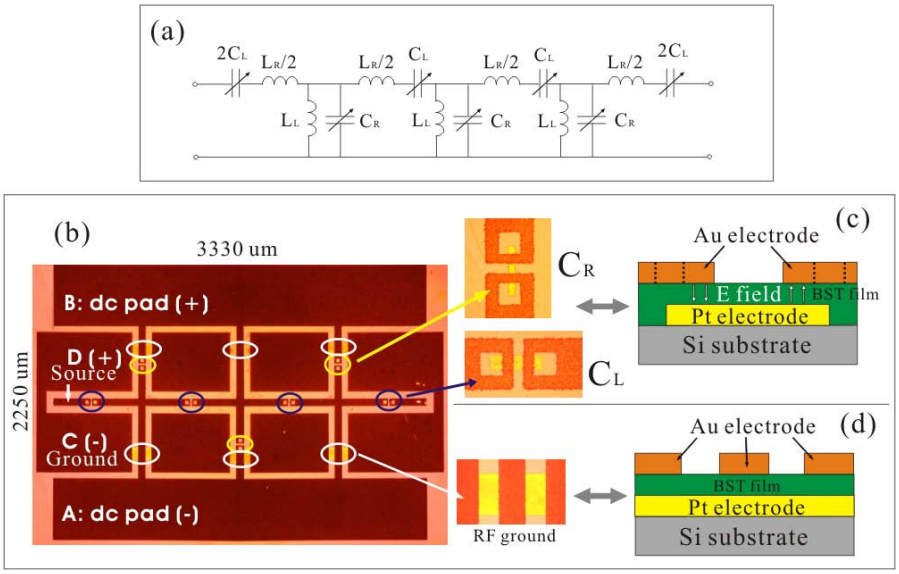

Figure 6.3 (a) Equivalent circuit of the CRLH TL phase shifter. (b) Layout of the phase shifter. (c) and (d) Magnified top-view and cross section of the varactors C_R and C_L, and RF ground.

The shunt capacitance C_R and series capacitance C_L are designed by consisting of two series capacitors. Figure 6.3 (c) and (d) showed the top-view images and schematic of cross section of varactors C_L and C_R, and radio frequency (RF) ground. The area of shunt capacitor C_R is $10\times10\ \mu m^2$ and that of the series capacitor C_L is $10\times15\ \mu m^2$. For the series capacitor $2C_L$, the area is designed to $15\times20\ \mu m^2$. The width of transmission line is 60 μm and the gap between source line and RF ground is 40 μm. The series capacitance C_L and the shunt resonance tank (C_R and L_L) are separated by high impedance CPW sections forming the series inductance L_R. It should be noted that the CPW line sections also contributes to C_R due to the line capacitance, however, the line capacitance is not tunable and will not affect the balanced condition under the applied bias voltage [11]. The stubs including shunt inductance L_L and the bias feed are RF grounded through 10×45 μm μm large varactors at microwave frequency. The ports of the phase shifter is implemented as a co-

planar waveguide (CPW) and can be measured directly by the ground-source-ground (GSG) picoprobe on pads C (ground) and D (source), as shown in Figure 6.3 (b). Bias was applied through two sets of dc power supply. One is applied on the dc bias pads A (-) and B (+), and another is applied on the pads C (-) and D (+) to provide bias to the two outer most varactors through GSG picoprobe. Such design can effectively apply the same dc voltage over each varactor.

6.3.2 Measurement Results and Discussion

The measurements were performed by a Vector Network Analyzer as described in chapter 4. Figure 6.4 shows the capacitance and loss tangent of the two series connected varactors as a function of dc bias up to 10 V. The capacitance is calculated from the measured scattering parameter data $S_{11} = (Z - Z_0)/(Z + Z_0)$ after one-port SOLT calibration. Then, one can obtain the real and imaginary parts of capacitance, and the loss tanδ=C″/C′ according to the load impedance Z=R+1/jω(C′+jC″) and characteristic impedance Z_0 is 50 Ω. The capacitance decreases with the increase of applied dc voltage, showing tunability [C(0)-C(V)]/C(0)×100% ~22%. The loss tanδ shows about 0.033 at *f*=1GHz and zero voltage. Here, the capacitance without dc bias is about 2.36 pF, which is the value of two series connected capacitors with area of 25×25 μm^2. Namely, the capacitance for one capacitor is 4.72 pF. Then, we calculate the permittivity ε~350 for BST thin film according to $\varepsilon = Cd/\varepsilon_0 A$, where d=410 nm is the thickness of the BST film and A=625 μm^2 is the area

of electrode. This value of the permittivity for BST thin film and is consistent with that in the previous chapter.

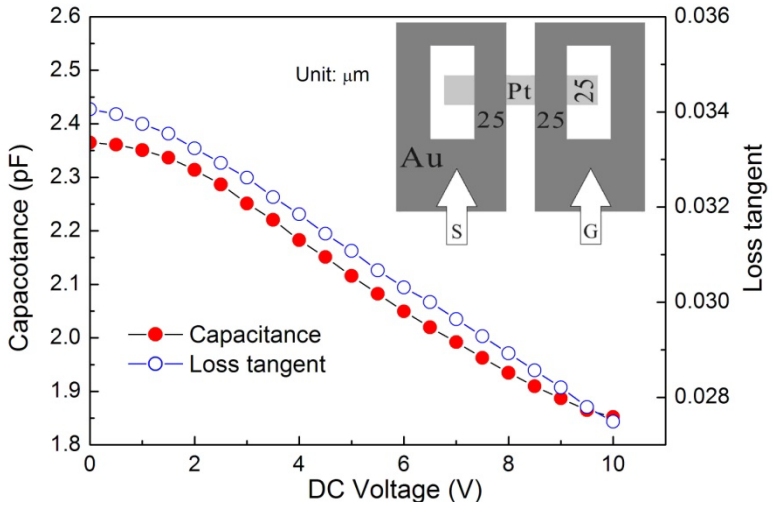

Figure 6.4 Capacitance and loss tangent of two series connected varactors at *f*=1 GHz as a function of dc bias up to 10 V.

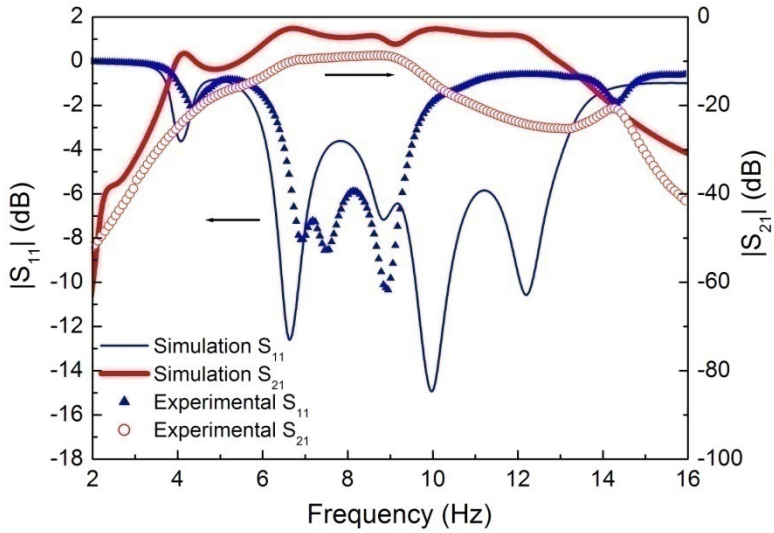

Figure 6.5 Comparison between measured and HFSS simulated forward transmission and reflection magnitude.

The varactors and CPW lines sections were simulated individually by high frequency simulator system (HFSS), and then the device with optimized circuit model was simulated after a satisfactory performance was obtained. In simulations, the capacitances, such as C_R=0.38 pF and C_L=0.57 pF, are determined according to obtained BST permittivity ε~350. Figure 6.5 shows the simulated and experimental results of reflection loss S_{11} and transmission loss S_{21} for the CRLH TL phase shifter as a function of frequency. The experimentally measured reflection loss is about -11 dB, and the measured transmission loss is around -8 dB near 7 GHz. The deviation from measured results with HFSS simulations could be associated with the metal losses of the top electrodes, which is generally poor due to the electroplating gold and form of vertical edges with the bottom electrode [19, 21].

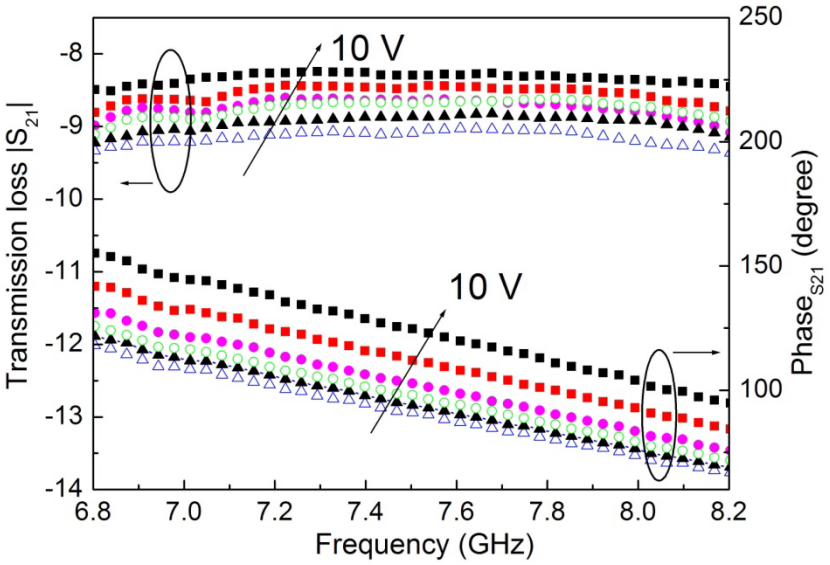

Figure 6.6 Measured magnitude and phase responses of the phase shifter under different bias voltages.

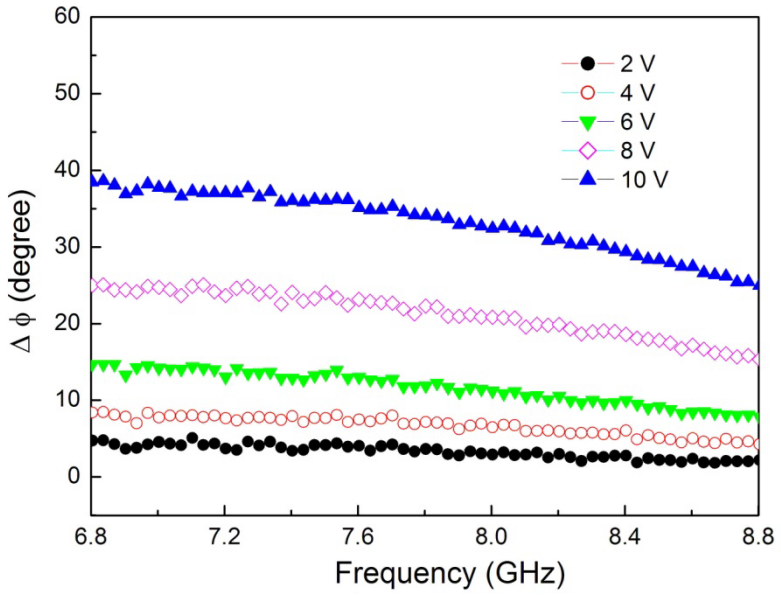

Figure 6.7 Differential phase shift under different dc biases over each varactor.

Figure 6.6 shows the magnitude of the transmission loss S_{21} and transmission phase at the different dc bias between 6.8 GHz and 8.8 GHz. The magnitude of S_{21} and transmission phase change with respect to applied dc voltage, corresponding to the decreased capacitance of tunable varactor. The relatively high insertion losses are partly associated with the poor quality of electroplated Au film. Figure 6.7 displays the differential phase shift under the different dc voltages. Here, the differential phase shift is the change of the transmission phase φ_{21} under applied voltage and is expressed as equation (6.10). The figure of merit, defined as phase shift $\Delta\varphi$ divided by the transmission loss S_{21}, changes from 4.8 deg/dB to 3.3 deg/dB extending from 6.8 GHz to 8.8 GHz. In this frequency range, the CRLH TL phase shifter shows a 35^{o} phase shift at bias voltage of 10 V. Clearly, the differential phase shift exhibits the flat frequency dependence behaviors below the dc bias of 6 V, whereas, the differential phase shift decreases gently with respect to frequency at the high dc bias. The inclined differential phase shift is due to

unbalanced state between left-hand and right-hand passbands of CRLH TL as high dc bias is applied over the varactors. This is because the tunability for each varactor in circuit is not linear with respect to dc bias, and the differential phase shift $\Delta\varphi$ is strongly dependent upon the tunability, as expressed in equation (6.10). Therefore, the differential phase shift exhibits frequency dependence behavior at high dc bias around the center frequency.

6.4 Conclusions

This chapter has presented the theory of composite right/left-handed transmission line (CRLH TL). A new type of phase shifter based on CRLH TL offers some significant advantages when compared to standard delay TLs: it is more compact in size, it can achieve a positive or a negative phase shift while occupying the same short physical length and it also can exhibits a linear, flatter phase response with frequency, leading to shorter group delays. As a result, a CRLH TL phase shifter with parallel-plate ferroelectric thin film varactors integrated on silicon substrate has been fabricated and performed. The alternative “cross” shape basic unit of CRLH TLs is designed and realized in order to apply the same dc voltages over each varactor and control voltages easily. The results indicate that the CRLH TL phase shifter provides a differential phase shift with flat frequency dependence characteristic in the measured frequency range, which demonstrates the validity of model of CRLH TL phase shifter. The phase shifter presented here exhibits good performances and compactness for high frequency applications.

References:

1. V. G. Veselago, “The electrodynamics of substances with simultaneously negative values of ε and μ”, *Sov. Phys.Uspekhi*, **10**(4), 509 (1968).

2. C. Caloz and T. Itoh, “Electromagnetic Metamaterials: Transmission Line Theory and Microwave Applications”, *Wiley*, New Jersey, (2006).

3. G. V. Eleftheriades, K. G. Balmain, “Negative Refraction Metamaterials: Fundamental Principles and Applications”, *Wiley*, New Jersey, (2005).

4. D. R. Smith, W. J. Padilla, D. C. Vier, S. C. Nemat-Nasser, S. Schultz, “Composite medium with simultaneously negative permeability and permittivity”, *Phys. Rev. Lett.*, **84**, 4184 (2000).

5. R. A. Shelby, D. R. Smith, and S. Schultz, “Experimental verification of a negative index of refraction”, *Science*, **292**, 77 (2001).

6. A. K. Iyer and G. V. Eleftheriades, “Negative refractive index metamaterials supporting 2-D waves”, in *Proc. IEEE MTT Int. Symp.*, **2** (2), 412 (2002).

7. G. V. Eleftheriades, A. K. Iyer, and P. C. Kremer, “Planar negative refractive index media using periodically L-C loaded transmission lines”, *IEEE Transactions on Microwave Theory and Techniques*, **50**, 2702 (2002).

8. C. Caloz and T. Itoh, “Application of the transmission line theory of left-handed (LH) materials to the realization of a microstrip LH transmission line”, in *Proc. IEEE-AP-S USNC/URSI National Radio Science Meeting*, San Antonio, TX, **2**, 412 (2002).

9. C. Caloz, H. Okabe, T. Iwai, and T. Itoh, “Transmission line approach of left-handed (LH) materials”, in *Proc. USNC/URSI National Radio Science Meeting*, San Antonio, TX, **1**, 39 (2002).

10. A. A. Oliner, “A periodic-structure negative-refractive-index medium without resonant elements,” in *URSI Digest, IEEE-AP-S USNC/URSI National Radio Science Meeting*, San Antonio, TX, p41 (2002).

11. A. Lai, C. Caloz, T. Itoh, “Composite right/left-handed transmission line metamaterials”, *IEEE Microwave Magazine*, **5**, 34 (2004).

12. J. He, B. Z. Wang, K. H. Zhang, “Arbitrary dual-band coupler using accurate model of composite right/left handed transmission line”, *Journal of Electromagnetic Waves and Applications*, **22**, 1267 (2010).

13. J. Park, Y. Lee, “A tunable dual-band branch line coupler based on composite right /left handed transmission lines”, *Microwave and Optical Technology Letters*, 52, 1955 (2010).

14. M. A. Antoniades, and G. V. Eleftheriades, “Compact linear lead/lag metamaterial phase shifters for broadband applications”, *IEEE Antennas and Wireless Propagation Letters*, **2**, 103 (2003).

15. B. Li, X. W. Dai, B. Wu, C. H. Liang, “Ultra wideband filter design based on composite right-/left-handed transmission line”, *Microwave and Optical Technology Letters*, **49**, 2379 (2007).

16. S. Kamada, N. Michishita, Y. Yamada, “Leaky Wave Antenna Using Composite Right/Left-Handed Transmission Line Composed of Ladder Network for UHF Band”, *IEICE Transactions on communications*, **E93B** (10), 2562 (2010).

17. A. Rahman, Y. Hao, Y. Lee, C. G. Parini, “Effect of unit-cell size on performance of composite right/left-handed transmission line based leaky-wave antenna”, *Electronics Letters*, **44**, 788 (2008).

18. S. Sheng, P. Wang, and C. K. Ong, “Compact Tunable periodically LC Loaded phase shifter using left-handed transmission line”, *Microwave and Optical Technology Letters*, **51**(9), 2127 (2009).

19. D. Kuylenstierna, A. Vorobiev, P. Linnér, and S. Gevorgian, “Composite right/left handed transmission line phase shifter using ferroelectric varactors”, *IEEE Microwave and Wireless Components Letters*, **16**, 167 (2006).

20. D. Kuylenstierna, A. Vorobiev, P. Linnér, and S. Gevorgian, “Ultrawide-band tunable true-time delay lines using ferroelectric varactors”, *IEEE Trans. Microw. Theory Tech.*, **53**, 2164 (2005).

21. D. Kuylenstierna, E. Ash, A. Vorobiev, T. Itoh, and S. Gevorgian, “X-band Left Handed Phase Shifter using Thin Film $Ba_{0.25}Sr_{0.75}TiO_3$ Ferroelectric Varactors”, *Proceedings of the 36th European Microwave Conference*, 847 (2006).

Chapter 7

DUAL-TUNABLE TRILAYERED STRUCTURE OF FERROELCTRICS AND MULTIFERROICS FOR MICROWAVE DEVICE APPLICATIONS

In this chapter, a multiferroic trilayered structure composed of a $BiFeO_3$ (BFO) layer and two $Ba_{0.25}Sr_{0.75}TiO_3$ (BST) layers is studied. Compared with the single-layered BST or the single-layered BFO, the trilayered structure provides the possibility of simultaneous broadband magnetic field and fast electrical field tuning of its microwave properties. This gives a unique opportunity for construction of cost-effective, fast and broadband devices for a wide range of microwave applications.

7.1 Introduction

Multiferroic (MF) materials have attracted major attention in recent years due to the unique possibility to tune the magnetic properties with a modest electric field and vice versa [1-4]. $BiFeO_3$ (BFO) is one of the most extensively studied multiferroic materials since it exhibits large spontaneous polarization of ~50 $\mu C/cm^2$, high ferroelectric Curie temperature (T_c =830 ˚C) [5], and high antiferromagnetic Néel temperature (T_N = 280 ˚C) [6]. Thus it offers exciting potential for room temperature device integration, if there is coupling between the order parameters [3, 7, 8], as is the case for some multiferroic manganites at low temperatures [9, 10]. The possibility of

including extra functionality with a device makes MF materials very attractive for application in microwave technology. Furthermore, the coupling of the electric and the magnetic polarizations provides an additional degree of freedom in device design. However, there are very few papers reporting the properties of MF materials in high microwave frequency range. The main reason for the lack of published high-frequency measurement data is the high leakage current in these materials and especially in samples of thin films. Until now, many attempts have been made to reduce the leakage current and improve the multiferroic behavior of BFO, for examples, by substituting ions into the either A-site (Bi^{3+}) or B-site (Fe^{3+}) or both sites of the lattice [11-15], formation of a multilayered structure, and control of film orientation and crystallinity [16-18]. The multilayered structure approach is among the most promising ongoing topics, whereby the coupling and interactions among the different functional layers can strongly influence the growth and physical properties of the thin film.

For BFO thin films, the effect of the magnetic field on the dielectric response is large [19]. Ferroelectric materials have electric field tunablility that can be achieved through the application of a modest voltage with a negligible current drain. As a promising candidate material for tunable microwave devices, $Ba_{1-x}Sr_xTiO_3$ (BST) has been extensively studied in the past years. Extra flexibility in terms of tuning, enhanced functionalities and performances of tunable devices may be achieved by combination of multiferroic materials with ferroelectric materials. Devices based on such multifunctional materials offer dual, i.e. electric, magnetic tuning possibility and extra flexibility in designing and shaping the device performances. In the

next sections, a multiferroic trilayered structure composed of a $BiFeO_3$ layer and two $Ba_{0.25}Sr_{0.75}TiO_3$ layers for tunable microwave device applications will be presented.

7.2 Experimental Procedure and Samples

The BST/BFO/BST thin films were grown in sequence on platinized silicon ($Pt/TiO_2/SiO_2/Si$) substrates using PLD with ceramic targets of $Ba_{0.25}Sr_{0.75}TiO_3$ and $BiFeO_3$, which were synthesized via a solid-state reaction of constituent oxides. The deposition parameters of BST thin films were described in chapter 2. The BFO film was deposited in situ under 0.05 mbar oxygen pressure at a substrate temperature of 520 °C. After deposition, the samples were annealed for half an hour in 1×10^3 mbar oxygen pressure. For comparison, the BFO thin film of 350 nm was prepared with the same conditions as above. To characterize their dielectric properties, the Au dots of 0.2 mm radius were sputtered on BST thin films using a shadow mask at room temperature. To characterize their microwave properties, the top electrodes were patterned as presented in section 3.2.1 of chapter 3.

The crystal structures and orientation of the BST, BST/BFO, and BST/BFO/BST thin films were characterized by XRD. The thickness and microstructure was observed by SEM. The dielectric properties of the samples at low frequencies were measured by HP4194A LF Impedance Analyzer. An electromagnet was used to provide the external dc magnetic bias fields. Their ferroelectric properties were studied by using the RT6000S (Radiant Technologies, Inc). One-port reflection measurements of the trilayered

structure at frequencies 10 MHz –16 GHz were carried out using a Network Analyzer (described in section 2.3.1 of chapter 2).

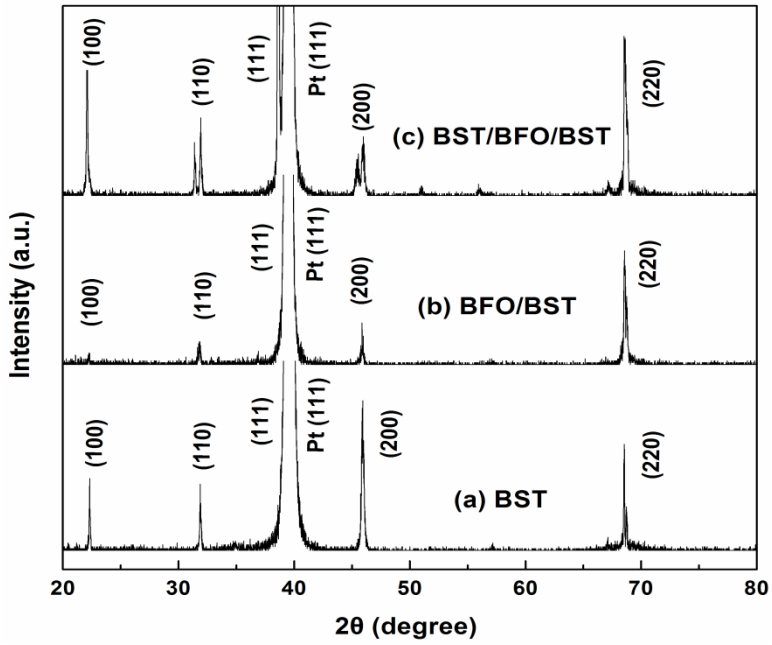

Figure 7.1 XRD patterns of the films (a) BST, (b) BFO/BST, and (c) BST/BFO/BST on (111) $Pt/TiO_2/SiO_2/Si$ substrates.

7.3 Results and Discussion

Figure 7.1 shows the XRD patterns of the BST, BFO/BST, and BST/BFO/BST thin films, together with $Pt/TiO_2/SiO_2/Si$ substrates. Apparently, all films display a polycrystalline structure. There is no shift in the corresponding 2θ reflection positions of BST and BFO/BST films and perovskite structure is shown with rhombohedral or pseudocubic symmetry without any secondary phases. However, there is shift in the corresponding 2θ reflection positions of the trilayered BST/BFO/BST film. Figure 7.2 shows the field emission SEM image of the cross section of trilayered BST/BFO/BST

thin film. The thicknesses of BST, BFO, and BST layers were calculated to be ~ 274, ~242, and ~274nm, respectively.

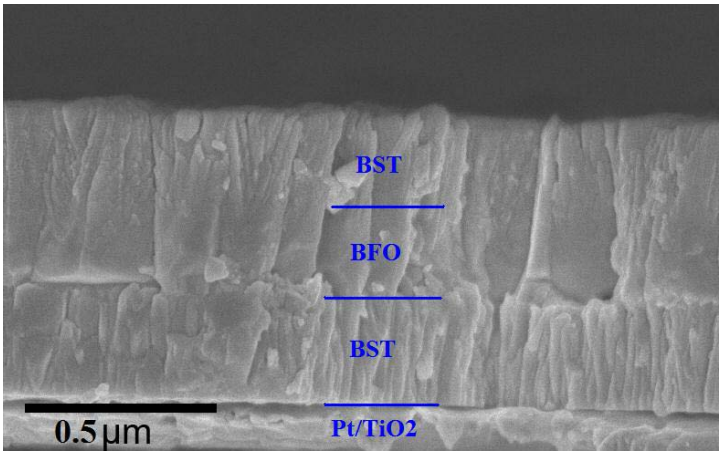

Figure 7.2 SEM picture of cross-section of the trilayered BST/BFO/BST thin films.

Figure 7.3 (a) shows electric response data, through a plot of the trilayered film relative dielectric constant ε_r versus the electric field across the gold top electrode and the platinum bottom electrode as obtained from 0.1MHz capacitance measurements. A significant tuning response for the relative dielectric constant ε_r with the electric field was obtained for the BST/BFO/BST thin film. Figure 7.3 (b) plots the *P*-*E* hysteresis loops for the trilayered BST/BFO/BST thin films and the single layer BFO thin film at room temperature and under 250 Hz. For the trilayered BST/BFO/BST thin films, all the loops show a slim shape and reach saturation at low electric fields (above 150 KV·cm^{-1}), indicating a typical soft ferroelectric behavior. It exhibited an apparently well established hysteresis loops with the remnant polarization ($2P_r$) of 29.3 µC·cm^{-2} and the coercive field ($2E_c$) of 34.3 KV·cm^{-1}, respectively at an applied electrical field of 200 KV·cm^{-1}.

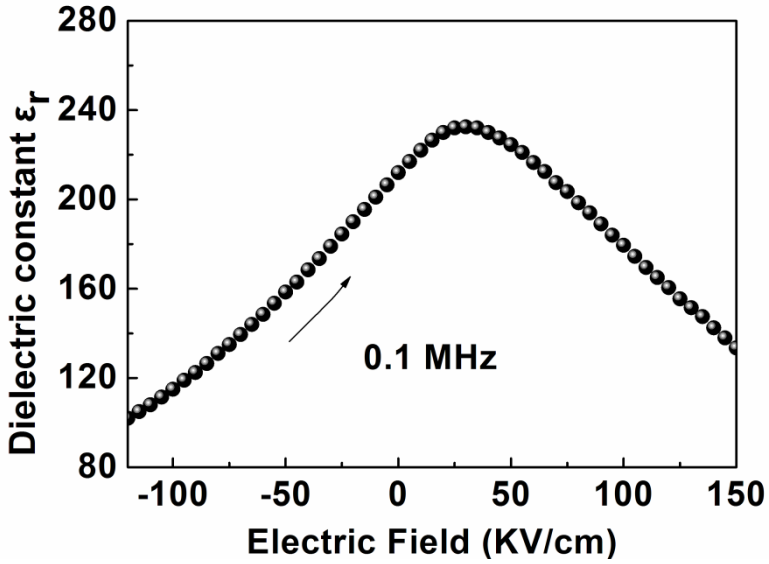

(a)

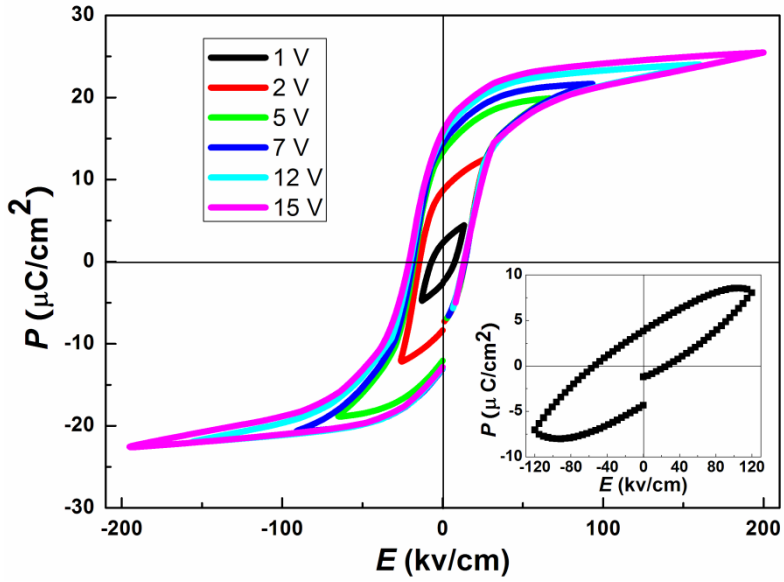

(b)

Figure 7.3 (a) The relative dielectric constant (ε_r) versus external electric fields for the trilayered BST/BFO/BST structure at 0.1 MHz. (b) The *P-E* hysteresis loops for the trilayered BST/BFO/BST structure at a series of external fields at room temperature and 250 Hz, where the inset for the *P-E* loop of the single layer BFO thin film.

For the single layer BFO thin film, the inset of Figure 7.3 (b) shows an unsaturated loose *P-E* loop, indicating a considerable degree of leakage current. This is consistent with what has been commonly observed for the

BFO thin film deposited on $Pt/TiO_2/SiO_2/Si$ substrate. The enhancement in the ferroelectric properties of the trilayered structure might be attributed to the factor that the coupling reaction between the BST and BFO thin films, which caused the enhancement in the ferroelectric properties of BFO thin film. Moreover, the BST layer might act as an important role in blocking the charge transfer between BFO and the bottom electrode and improving the resistance. Murari et al. [20] reported that the leakage current density was significantly reduced in BST/BFO thin film when compared to pure BFO thin film. For the trilayered BST/BFO/BST thin film, a further reduction in the leakage current would be obtained, which is necessary to make use of this structure for microwave devices.

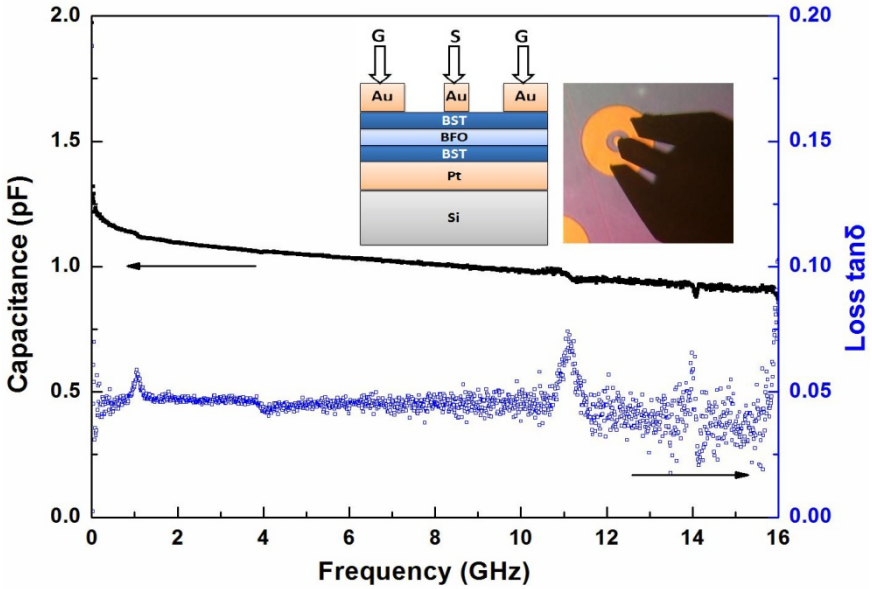

Figure 7.4 Microwave frequency dependences of the capacitance and loss tangent for the BST/BFO/BST trilayered structure. The insets show the cross-section of the trilayered structure and the photograph of the measurement setup using a GSG coplanar waveguide probe, respectively.

To characterize the microwave properties of the multiferroic trilayered structure, the top electrodes were patterned as central circular patches

surrounded by concentric electrodes, as shown in the insets of Figure 7.4 (ref. section 3.2.1). Figure 7.4 shows the capacitance and loss tangent of the multiferroic trilayered structure versus microwave frequencies at room temperature and zero external electric field. It is seen clearly that the capacitance is fairly frequency independent in the range 2-16 GHz. The peaks appearing in the microwave data of loss tangent were due to the Network Analyzer. To investigate the dielectric properties of the trilayered structure under an external magnetic field, we measured the capacitance versus frequency under different external magnetic field. As shown in Figure 7.5, the dielectric constant is controllable via the external magnetic field. With increasing the magnetic field, the capacitance increases, which demonstrated the coupling between electric and magnetic polarizations in the trilayered structure. However, the relatively large frequency dependence of the capacitance at low frequencies suggests a finite level of space charge polarizability, which may occur at the interface between the BFO and BST layers. The film microstructure should be improved to reduce the space charges. Moreover, an improvement upon frequency dependence can be done by making the tunability measurements at higher frequencies. The inset of Figure 7.5 shows the magnetic field dependences of the capacitance of the trilayered BST/BFO/BST structure at different frequency and the loss tangent at 10 kHz, which states that the magnetic field dependence of loss tangent is very small. The percentage change of the capacitance under 1 T dc magnetic field increases with the raise of frequency from 11.8% at 0.5 kHz to 18.7% at 100 kHz, which is better than the result reported in [21]. The magnetic field effect on the dielectric constant is expected to be stronger at higher frequency

[21]. Compared with the electric field, the tuning response for dielectric constant with the magnetic field is relatively small. But, the linear change in the dielectric constant with external magnetic field under different frequency was obtained.

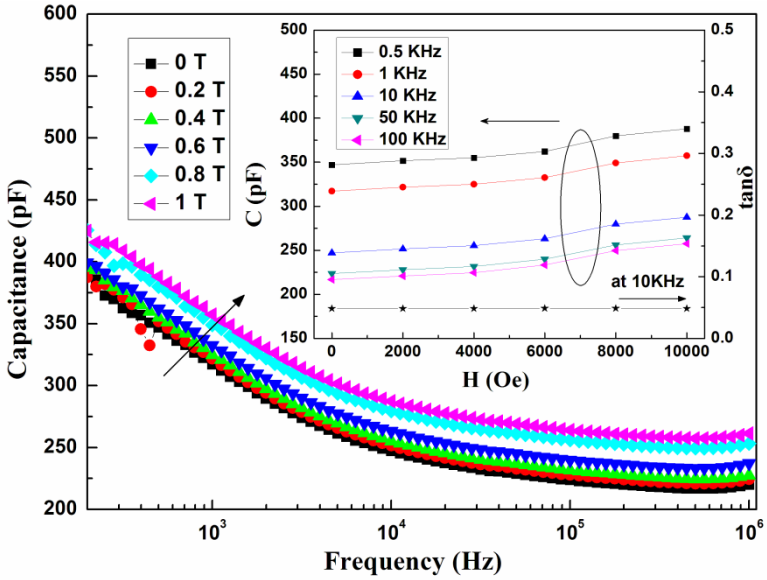

Figure 7.5 The capacitance of the multiferroic BST/BFO/BST trilayered structure versus frequency under different external magnetic field. The inset shows the magnetic field dependences of the capacitance at different frequency and loss tangent at 10 kHz.

7.4 Conclusion

A multiferroic trilayered BST/BFO/BST thin film structure on the Pt/TiO_2 /SiO_2/Si substrate has been fabricated and investigated. The significant tuning response for the dielectric constant with the electric field and the magnetic field respectively was obtained for the multiferroic trilayered structure. It should be noted that a multiferroic BST/BFO/BST trilayered structure presented here may have potential application in microwave devices, which offer dual, i.e. electric and magnetic, tuning possibility and extra flexibility in designing and shaping the device performances.

References:

1. Y. N. Venevtsev, V. V. Gagulin, “Search, design and investigation of seignettomagnetic oxides Ferroelectrics”, *Ferroelectrics*, **162**, 23 (1994).

2. J. Wang, J. B. Neaton, H. Zheng, V. Nagarajan, S. B. Ogale, B. Liu, D. Viehland, V. Vaithyanathan, D. G. Schlom, U. V. Waghmare, N. A. Spaldin, K. M. Rabe, M. Wuttig, R. Ramesh, “Epitaxial BiFeO3 Multiferroic Thin Film Heterostructures”, *Science*, **299**, 1719 (2003).

3. T. Kimura, T. Goto, H. Shintani, K. Ishizaka, T. Arima, Y. Tokura, “Magnetic control of ferroelectric polarization”, *Nature*, **426**, 55 (2003).

4. D. H. Wang, W. C. Goh, M. Ning, and C. K. Ong, “Effect of Ba doping on magnetic, ferroelectric, and magnetoelectric properties in mutiferroic $BiFeO_3$ at room temperature”, *Appl. Phys. Lett.*, **88**, 212907, (2006).

5. G. A. Smolenskii, V. A. Isupov, A. I. Agranovskaya, and N. N. Krainik, *Sov. Phys. Solid State*, **2**, 2651 (1961).

6. P. Fischer, M. Polomska, I. Sosnowska, and M. Szymanski, “Temperature dependence of the crystal and magnetic structures of $BiFeO_3$”, *J. Phys. C: Solid State Phys*, **13**, 1931 (1980).

7. C. Ederer, and N. A. Spaldin, “Influence of strain and oxygen vacancies on the magnetoelectric properties of multiferroic bismuth ferrite”, *Phys. Rev. B*, **71**, 224103 (2005).

8. P. Baettig, C. Ederer, and N. A. Spaldin, “First principles study of the multiferroics BiFeO3, Bi2FeCrO6, and BiCrO3: Structure, polarization, and magnetic ordering temperature”, *Phys. Rev. B*, **72**, 214105 (2005).

9. M. Fiebig, T. Lottermoser, D. Frohlich, A. V. Goitsev, and R. V. Pisarev, “Observation of coupled magnetic and electric domains”, *Nature*, **419**, 818 (2002).

10. T. Lottermoser, T. Lonkai, U. Amann, D. Hohlwein, J. Ihringer, and M. Fiebig, “Magnetic phase control by an electric field”, *Nature*, **430**, 541 (2004).

11. S. K. Singh, H. Ishiwara, and K. Maruyama, “Room temperature ferroelectric properties of Mn-substituted $BiFeO_3$ thin films deposited on Pt electrodes using chemical solution deposition”, *Appl. Phys. Lett.*, **88**, 262908 (2006).

12. J. K. Kim, S. S. Kim, W.-J. Kim, A. S. Bhalla, and R. Guo, "Enhanced ferroelectric properties of Cr-doped $BiFeO_3$ thin films grown by chemical solution deposition", *Appl. Phys. Lett.*, **88**, 132901 (2006).

13. X. Qi, J. Dho, R. Tomov, M. G. Blamire, and J. L. MacManus-Driscoll, "Greatly reduced leakage current and conduction mechanism in aliovalent-ion-doped $BiFeO_3$", *Appl. Phys. Lett.*, **86**, 062903 (2005).

14. S. R. Das, P. Bhattacharya, R. N. P. Choudhary, and R. S. Katiyar, "Effect of La substitution on structural and electrical properties of $BiFeO_3$ thin film", *J. Appl. Phys.*, **99**, 066107 (2006).

15. C. F. Chung, J. P. Lin, and J. M. Wu, "Influence of Mn and Nb dopants on electric properties of chemical-solution-deposited $BiFeO_3$ films", *Appl. Phys. Lett.*, **88**, 242909 (2006).

16. Y. W. Li, J. L. Sun, J. Chen, X. J. Meng, and J. H. Chu, "Structural, ferroelectric, dielectric, and magnetic properties of $BiFeO_3$/Pb($Zr_{0.5}$,$Ti_{0.5}$)-O_3 multilayer films derived by chemical solution deposition", *Appl. Phys. Lett.*, **87**, 182902 (2005).

17. Z. Cheng, X. Wang, C. V. Kannan, K. Ozawa, H. Kimura, T. Nishida, S. Zhang, and T. R. Shrout, "Enhanced electrical polarization and ferromagnetic moment in a multiferroic $BiFeO_3$/$Bi_{3.25}Sm_{0.75}Ti_{2.98}V_{0.02}O_{12}$ double-layered thin film", *Appl. Phys. Lett.*, **88**, 132909 (2006).

18. Y. J. Qi, C. J. Lu, Q. F. Zhang, L. H. Wang, F. Chen, C. S. Cheng, and B. T. Liu, "Improved ferroelectric and leakage properties in sol–gel derived $BiFeO_3$/$Bi_{3.15}Nd_{0.85}Ti_3O_{12}$ bi-layers deposited on Pt/Ti/SiO_2/Si", *J. Phys. D: Appl. Phys.*, **41**, 065407 (2008).

19. Peter Kr. Petrov, Vaijayanti R. Palkar, Alexander K Tagantsev, Hsin-I Chien, K. Prashanthi, Anna-Karin Axelsson, S. Bhattacharya, Neil McN Alford, "Dielectric properties characterization of La- and Dy-doped $BiFeO_3$ thin films", *J. Mater. Res.*, **22**, 2179 (2007).

20. N. M. Murari, A. Kumar, R. Thomas, and R. S. Katiyar, "Reduced leakage current in chemical solution deposited multiferroic $BiFeO_3$/$Ba_{0.25}Sr_{0.75}TiO_3$ heterostructured thin films on platinized silicon substrates", *Appl. Phys. Lett.*, **92**, 132904 (2008).

21. J. X. Zhang, J. Y. Dai, C. K. Chow, C. L. Sun, V. C. Lo, H. L. W. Chan, "Magnetoelectric coupling in $CoFe_2O_4$/$SrRuO_3$/Pb($Zr_{0.52}Ti_{0.48}$)O_3 hetero-epitaxial thin film structure", *Appl. Phys. Lett.*, **92**, 022901(2008).

Chapter 8

CONCLUSIONS AND FUTURE WORK

8.1 Conclusions

Ferroelectric materials have been considered as promising candidates for electrically tunable microwave device applications. In this work, miniature and tunable microwave devices based on ferroelectric $Ba_xSr_{1-x}TiO_3$ (BST) thin films were investigated. Our work mainly includes fabrication of ferroelectric thin films, characterization of microwave dielectric properties, development of tunable microwave devices based on ferroelectric thin films, such as varactors and phase shifters.

A reliable measurement method for the microwave dielectric properties of parallel plate ferroelectric varactor with the aid of electromagnetic simulation software was presented. Parallel plate varactors based on BST thin film deposited by PLD on the platinized silicon substrate were fabricated. The test structures for microwave measurement of BST parallel plate varactor need to be designed for the measurement of reflection coefficient S_{11}. In this measurement method, the parasitic effects were effectively removed in evaluating the thin film dielectric properties based on a good agreement between the experimental results measured with parasitic model and the computer simulation data.

Effects of bottom electrodes including $La_{0.7}Sr_{0.3}MnO_3$ (LSMO), Pt and Au, on microwave dielectric properties of BST parallel plate varactors were

investigated. The results show that the bottom electrodes appear to have a strong influence on the dielectric properties of the BST thin films in high frequency range. The (*00l*) BST thin film was grown epitaxially on LSMO bottom electrode. The structures of BST thin films grown on LSMO and Pt bottom electrodes show columnar grains respectively. The experimental measurement reveals that the BST film grown on LSMO bottom electrode has a maximum dielectric constant and a little higher loss tangent due to the higher resistive loss.

A systematic comparison of the microwave properties of BST thin film varactors with parallel plate and interdigital electrodes was investigated. Compared with the interdigital structure, significant dielectric dispersion and lower permittivity are observed in the parallel plate varactors since the interfacial polarization between the electrode and the film plays an important role in dielectric measurements.

A new hybrid varactor, which integrates the features of both basic structures of coplanar and parallel plate varactors, was proposed by our group. In our experiments, the configuration of the hybrid varactor was modified. At the same time, a ZnO ultra-thin film layer was used for the high resistivity dc bias bottom electrode, which is nearly “transparent” to microwave signal. The BST hybrid varactor with low capacitance has improved the tunability of the conventional coplanar varactor by integrating a vertical dc bias electrode with low conductivity.

A distributed coplanar waveguide (CPW) microwave phase shifter using BST thin film varactors with parallel plate electrodes was designed, simulated, and fabricated. The CPW phase shifter exhibited a continuous 0-170^{o}

differential phase shift from 10 MHz to 7 GHz at a low bias voltage of 25 V. The maximum insertion loss was 3.05 dB at 6.5 GHz with no dc bias and the return loss was better than 16 dB over all phase states. The prototype of the phase shifter showed a high figure of merit of 78^{o}/dB.

A coupled microstrip line microwave phase shifter using parallel plate BST varactors was demonstrated. Two planar Marchand baluns were used in the phase shifter as the transformers of odd mode excitation and a transmission stop circuit for even mode excitation as well as the impedance matching networks. In the operational band from 6 GHz to 10 GHz, the measured insertion loss was less than 4 dB and return loss was better than 13 dB. A differential phase shift of 45 degree was obtained with a dc bias of 20 V at frequency of 9 GHz.

A composite right/left-handed transmission line (CRLH TL) phase shifter with parallel plate ferroelectric thin film varactors integrated on silicon substrate was presented. This new type of phase shifter offers some significant advantages when compared with standard delay TLs: it is more compact in size, it can achieve a positive or a negative phase shift while occupying the same short physical length and it also can exhibit a linear, flatter phase response with frequency, leading to shorter group delays. At the frequency of 7.6 GHz, a 35^{o} differential phase shift under bias voltage of 10 V was obtained. The experimental results demonstrated the unique features of the CRLH TL structure, providing a differential phase shift with flat frequency dependence characteristic in the operating frequency range.

The above mentioned three kinds of phase shifters were integrated on high resistance silicon substrates using BST thin film varactors with parallel plate

electrodes, respectively. At present, the CPW microwave phase shifter exhibited the best microwave properties. However, the CRLH TL phase shifter provided the unique features, which enable a differential phase shift with flat frequency dependence around center frequency. The phase shifter devices based on coupled microstrip line structure are less sensitive to interfacial effects and preferable for balanced circuits, especially for scanning reflectarray antenna applications.

A multiferroic trilayered BST/BFO/BST thin film structure on the Pt/TiO_2 /SiO_2/Si substrate was studied. The significant tuning response for the dielectric constant with the electric field and the magnetic field respectively was obtained for the multiferroic trilayered structure. This trilayered structure may have potential application in microwave devices, which offer dual, i.e. electric and magnetic, tuning possibility and extra flexibility in designing and shaping the device performances.

8.2 Future Work

In this work, the modified hybrid varactor structure has been shown to be an effective method to improve the tunability of the conventional coplanar varactor by integrating a vertical dc bias high resistance bottom electrode. However, the tunability of the hybrid varactor is relatively low for now. The tunability is expected to be improved by design optimization of hybrid varactor structure or alternative materials for low conductive electrode. $SrRuO_3$ (SRO) could be a good candidate material used for high resistance

bottom electrode. SRO is an ideal electrode in devices incorporating oriented ferroelectric films, due to its relatively high thermal conductivity, and good compatibility in structure and chemistry with perovskite type ferroelectric materials. The further work should be done to investigate in detail on how the presence of the high resistivity dc bias electrode affects the tunability and quality factor. It may be interesting to extend the applications of this new hybrid varactor structure into other passive circuits, such as phase shifters, filters, impedance matching networks, etc.

The composite right/left-handed transmission lines (CRLH TL) loaded by ferroelectric varactors presented in chapter 6 have great promise for MMIC applications. Conventionally, bandpass filters have been used as a core component for an RF/microwave communication system and designed based upon the half-wavelength resonator. However, the half-wavelength resonators are pointed out with shortcomings such as giving rise to the spurious resonance known as harmonics and limitation in practical size reduction. Balanced CRLH TLs exhibit typically broad bandwidths that are useful for the synthesis of ultrawide bandpass filters. Electrically tunable bandpass filters could be implemented by using resonant-type CRLH TLs loaded with ferroelectric BST thin film varactors. In the future, the studies of combination of these elements with split rings resonators (SRRs) should be carried out using microstrip MMIC planar technology for achieving a tunable bandpass filter with good performance.